AFRL-AFOSR-VA-TR-2020-0147

Active Metasurfaces for Advanced Wavefront Engineering and Waveguiding

Federico Capasso
HARVARD COLLEGE PRESIDENT & FELLOWS OF

12/19/2019
Final Report

DISTRIBUTION A: Distribution approved for public release.

Air Force Research Laboratory
AF Office Of Scientific Research (AFOSR)/ RTB1
Arlington, Virginia 22203
Air Force Materiel Command

REPORT DOCUMENTATION PAGE

Form Approved
OMB No. 0704-0188

1. REPORT DATE *(DD-MM-YYYY)*
22-08-2020

2. REPORT TYPE
Final Performance

3. DATES COVERED *(From - To)*
30 Sep 2014 to 29 Sep 2019

4. TITLE AND SUBTITLE
Active Metasurfaces for Advanced Wavefront Engineering and Waveguiding

5a. CONTRACT NUMBER

5b. GRANT NUMBER
FA9550-14-1-0389

5c. PROGRAM ELEMENT NUMBER
61102F

6. AUTHOR(S)
Federico Capasso, Alexandra Boltasseva, Mark Brongersma, Marko Loncar, Nader Engheta, Nanfang Yu, Vladimir Shalaev

5d. PROJECT NUMBER

5e. TASK NUMBER

5f. WORK UNIT NUMBER

7. PERFORMING ORGANIZATION NAME(S) AND ADDRESS(ES)
HARVARD COLLEGE PRESIDENT & FELLOWS OF
1350 MASS AVE STE 600
CAMBRIDGE, MA 02138-3846 US

8. PERFORMING ORGANIZATION REPORT NUMBER

9. SPONSORING/MONITORING AGENCY NAME(S) AND ADDRESS(ES)
AF Office of Scientific Research
875 N. Randolph St. Room 3112
Arlington, VA 22203

10. SPONSOR/MONITOR'S ACRONYM(S)
AFRL/AFOSR RTB1

11. SPONSOR/MONITOR'S REPORT NUMBER(S)
AFRL-AFOSR-VA-TR-2020-0147

12. DISTRIBUTION/AVAILABILITY STATEMENT
A DISTRIBUTION UNLIMITED: PB Public Release

13. SUPPLEMENTARY NOTES

14. ABSTRACT
Focus is on the new physics and materials afforded by metasurfaces and in particular on designer/ active metasurfaces that are reconfigurable/tunable with external control of their optical characteristics, including distinctively quantum properties. Nonconductive oxide and nitride plasmonic metasurfaces and 2D transition metal nitrides/carbides, namely MXenes, were developed and a new broadly tunable phase change material SmNiO3 was discovered. Highlights in the Physics are: synchrotron radiation from self-acceleration of nonlinear polarization, giant Kerr nonlinearities in ENZ metamaterials, phasematching-free harmonic generation in metasurfaces, Dirac cone and zero index metasurfaces and metasurfaces with exceptional points by topological optimization. NV centers in diamond metasurfaces have shown large enhancement of the Purcell factor. Arbitrary spin to orbital angular momentum conversion has been implemented. High performance monochromatic and broadband achromatic metalenses in the near IR and entire visible have been demonstrated along applications to new depth cameras, spectrometers and endoscopes.

15. SUBJECT TERMS
metasurfaces, wavefront engineering, waveguiding, light modulators, active meta-surfaces, phase change materials, transparent conductive oxides, planar photonics, flat photonics

16. SECURITY CLASSIFICATION OF:			17. LIMITATION OF ABSTRACT	18. NUMBER OF PAGES	19a. NAME OF RESPONSIBLE PERSON
a. REPORT	b. ABSTRACT	c. THIS PAGE			POMRENKE, GERNOT
Unclassified	Unclassified	Unclassified	UU		19b. TELEPHONE NUMBER

					19b. TELEPHONE NUMBER *(Include area code)* 703-696-8426

Standard Form 298 (Rev. 8/98)
Prescribed by ANSI Std. Z39.18

DISTRIBUTION A: Distribution approved for public release.

Final Performance Report
AFOSR Grant Number: FA9550-14-1-0389
Active Metasurfaces for Advanced Wavefront Engineering and Waveguiding

Reporting Period: 9/30/2014-9/30/2019

Program Manager: Gernot Pomrenke

PI: Prof. Federico Capasso
John A. Paulson, School of Engineering and Applied Sciences
Harvard University
205A Pierce Hall
29 Oxford St.
Cambridge MA 02138
Tel. 617-3847611
Fax 617-495-2875
Email: capasso@seas.harvard.edu

MURI team:
Harvard University (Co PI: Marko Loncar)
Columbia University (Co-PI: Nanfang Yu)
North Eastern University (Co PI: Hossein Mosallei)
Purdue University (Co PIs: Alexandra Boltasseva, Vladimir Shalaev)
Stanford University (Co PI: Mark Brongersma)
University of Pennsylvania (Co PI: Nader Engheta)

1. Executive summary

This MURI program was focused on exploring the new physics and materials science afforded by metasurfaces that can lead to breakthrough applications in photonics with specific focus on designer and active metasurfaces that are reconfigurable and/or tunable with external control of their optical characteristics, including distinctively quantum properties. The MURI team efforts were organized along the following thrusts:

Thrust 1: Materials Building Blocks,
Thrust 2: Physics of Metasurface Devices
Thrust 3: Metasurface Platforms
Thrust 4: Active Metasurfaces
Thrust 5: Quantum Metasurfaces

In *Thrust 1* achievements include the development of non-conductive oxide and nitride based plasmonic metasurfaces and of 2D transition metal nitrides/carbides, namely MXenes, for applications in flat optics, e.g. for control of light polarization and nanocavities. ITO-based tunable metasurfaces have been demonstrated. Conformal metasurface building blocks have been developed; they consist of inclusions made of silicon disk nanoantennae embedded in a flexible supporting layer of polydimethylsiloxane (PDMS). Porous polymer coatings for highly efficient passive daytime radiative cooling metasurfaces have been developed, mimicking the mechanism used by certain ants to cool in the desert. Correlated oxide $SmNiO_3$ as a new materials platform for broadband tunable photonics and network metamaterials for robust structured color, based on de-alloying the non-noble metal, have been developed.

Thrust 2 achievements include the exploration of novel nonlinear optical phenomena such synchrotron radiation from self-acceleration of nonlinear polarization in metasurfaces, giant Kerr nonlinearities in epsilon near zero (ENZ) metamaterials, phase-matching-free harmonic generation in gradient metasurfaces, nonlinear photonic doping and nonlinear Salisbury metasurfaces. Dirac cone and zero index metasurfaces have been experimentally demonstrated and exploited in band-engineering of new optical materials and photonic crystals; metamaterials with exceptional points have been discovered using topological optimization. In the area of structured light arbitrary spin angular momentum to optical angular momentum conversion, Cherenkov surface plasmons in one-dimensional metamaterials and chiroptical activity with giant circular dichroism and holograms for complex wavefront control have been demonstrated. One-way photonic surface states with magnetized materials, all-passive nonreciprocal metasurfaces and metasurfaces with plasmonic features without negative dielectrics have been designed.

Thrust 3 has focused on flat optics based on metasurface to replace conventional optical components with the advantage of smaller footprint, greater control of aberrations, ease of optical alignment and multifunctionality. The vision is that flat optics will lead to the convergence of lens making with semiconductor fabrication technology so that foundries will manufacture both the CMOS sensor and the camera module, leading to wafer level cameras for a wide range of applications. Using structural dispersion engineering of meta-atoms for broadband optical control, high NA monochromatic and broadband achromatic metalenses across the near IR and the entire visible have been demonstrated along with systems based on these advances such as miniature high-resolution spectrometers, new endoscopes for in vivo imaging of lung cancer and depth sensing cameras. Large area cm scale metalenses by stepper lithography have

been fabricated and tested along with hybrid metasurface-refractive lenses. Other components include metasurface doublets for Seidel aberration correction and triplets for controlling optical wavefronts over a large angular range; integrated photonic devices based on metasurfaces such as waveguide mode converters. Metasurfaces with spatially varying polarization response have been designed and demonstrated, which have enabled new ultracompact in-line and terminating polarimeters and single-shot polarization sensitive cameras without moving parts.
A diamond metasurface platform has been demonstrated that has yield ultrahigh reflectivity in the near IR with no sign of laser damage at high power. Other innovative devices include ultrathin multicolor cavities with embedded metasurfaces, enhanced graphene photodetectors with fractal metasurface and oolarization tunable color encoding in metasurfaces for encryption; inverse-designed metasurfaces as anti-reflection (AR) coatings for rough surfaces and metalenses with broken optical axes.

Thrust 4 has advanced the state-of-the-art of active metasurfaces. Tuning of the light scattering properties of plasmonic and semiconductor antennas above a metallic mirror has been demonstrated. From this work, it has become clear that Si nanowires are ideal building blocks for mechanically-tunable metasurfaces. The creation of dynamically tunable metasurfaces based on Mie resonators followed. Other seminal work includes the experimental demonstration spatiotemporal light control with frequency-gradient metasurfaces, MEMS based dynamic metalenses; adaptive metalenses with voltage-controlled focus and aberrations, metasurface tunability via nonlinearity and via mechanical actuation. Dual-band multilayer metasurface shared aperture antennas which can achieve two-dimensional beam steering simultaneously at two distinct operating wavelengths in near-infrared and visible have been designed. In a complementary effort bifunctional reflectarray antenna that can operate at two distinct frequencies in the near-IR with two different functionalities bending and focusing have been invented.

Thrust 5 Zero-index metamaterials based on diamond, leveraging on the group's expertise with diamond quantum photonics were explored, leading to the demonstration of devices that feature Dirac cone and exhibit zero-effective refractive index. NV centers in metasurfaces have shown large enhancement of the Purcell factor. Current activities are focused on introducing color silicon-vacancy (SiV) color centers inside the structures, with the goal of observation of super-radiant emission rom an array of SiVs. The main challenge is overcoming inhomogeneous distribution of SiV color centers, due to variations in local strain environments of different SiVs.

This work has resulted in 120 publications and 36 patents
Four startups have been created based on the research carried out under this MURI

2. Accomplishments

Nanfang Yu Group

The Columbia team led by Prof. Yu has focused on investigating new physical phenomena and device functionalities that are uniquely enabled by the low dimensionality of metasurfaces. The Columbia team has developed unconventional fabrication techniques to create flat optical devices and materials, with the ultimate goals to revolutionize the way one designs and manufactures optical devices and systems, to replace conventional optical devices and systems with their advanced "flat" counterparts, and to realize flat optical devices and systems with completely new functionalities. The most important research accomplishments are described below

Structural dispersion engineering of meta-atoms for broadband optical control

A metasurface consists of a 2D array of meta-atoms; their collective action imparts a spatial distribution of phase delays to an incident wavefront and molds the outgoing wavefront into a desired shape. To realize focusing, for example, the wavefront must be molded into a concave sphere. This is easily achieved at a single wavelength, but molding wavefronts at multiple wavelengths, or over a continuum of wavelengths, into the same spherical shape (for broadband focusing) is quite challenging, because each meta-atom must simultaneously satisfy the phase requirements at all design wavelengths. The Columbia team has addressed this challenge by structural dispersion engineering, i.e., exploring novel meta-atom geometries to provide a diverse range of phase dispersion (i.e., phase as a function of wavelength) well beyond what is achievable by meta-atoms with simple geometries. Figure 1 illustrates a few Silicon meta-atoms with widely-ranging phase dispersion in the near-infrared. These wavelength-dependent optical responses are summarized as the effective modal index in Fig. 1b, showing a continuum of responses from highly dispersive (large slope) to dispersion less (zero slope).

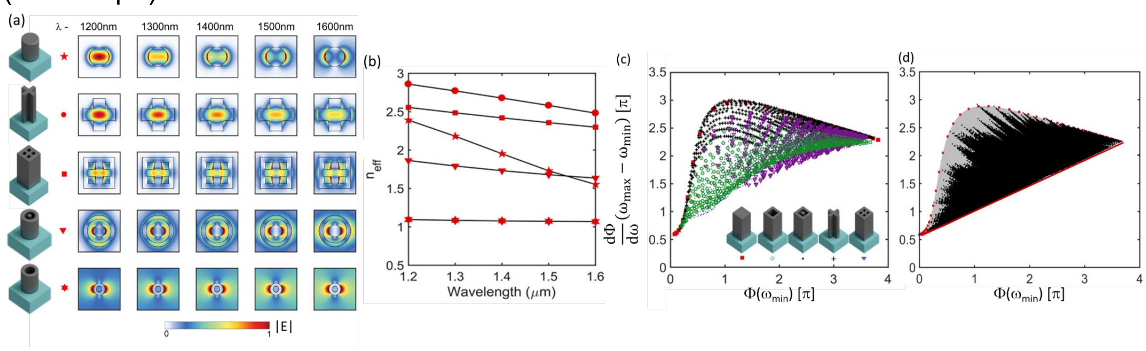

Fig. 1 (a) Example meta-atoms made of amorphous Silicon on a SiO_2 substrate. The meta-atoms support a variety of field profiles (pictured for selected wavelengths) with wavelength dependence controlled by the cross-sectional shapes. (b) Effective modal indices of the modes in (a), showing a variety of optical dispersion. (c) Coverage of the phase-dispersion space by an example meta-atom library. Phase of the lowest frequency (or largest wavelength, λ = 1.6 μm) and phase dispersion, $\Delta\phi = d\Phi/d\omega(\omega_{max}-\omega_{min})$ for the chosen bandwidth (i.e., λ = 1.2–1.6 μm) are calculated for each meta-atom, which is 1.4 μm in height and made of Silicon. Inset: Schematics showing meta-atom archetypes. The meta-atoms have four-fold symmetry and are thus polarization insensitive. (d) A set of 2^{21} = 2,097,152 simulations exploring all possibilities of creating binary meta-atoms and their coverage of the phase-dispersion space.

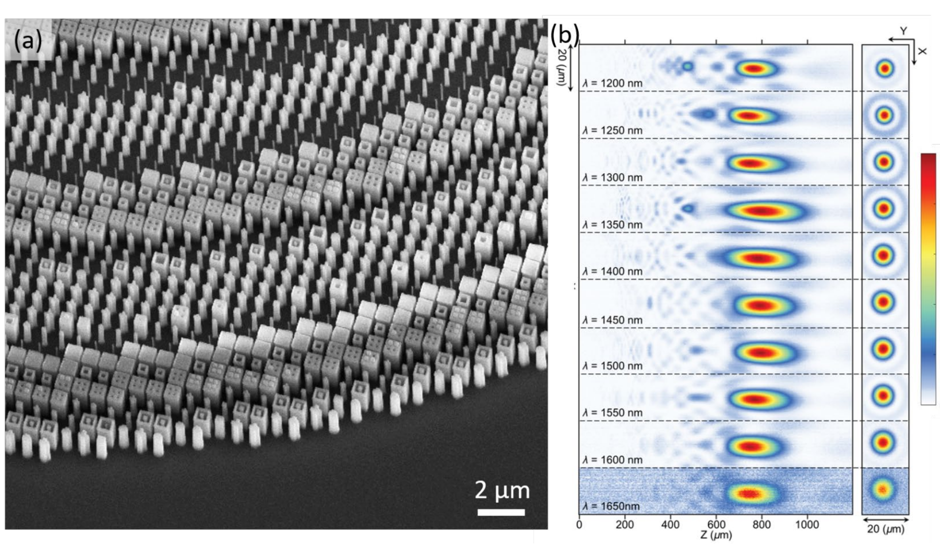

Fig. 2 (a) Scanning electron microscope (SEM) image of a Silicon achromatic meta-lens constructed using meta-atoms 1.4 μm in height. (b) Experimental confirmation of achromatic focusing at or near the diffraction limit over a broad wavelength range of λ=1.20-1.65 μm.

The Columbia team constructed meta-atom libraries by choosing a few different archetypal cross-sections, each representing a subclass of meta-atoms composed of the archetype's basic shape but with varying in-plane geometrical parameters (e.g., size of square pillars). They found that each archetype characteristically fills a different area of the phase-dispersion space (Fig. 1c), providing a continuous coverage of the 2D optical parameter space. They performed an exhaustive set of simulations based on binary search and show that the meta-atom library chosen based on physical intuition and constrained to fabricable structures (Fig. 1c) performs as well as the brute-force approach based on binary search and no constraint on fabricability (Fig. 1d) in terms of fully spanning the phase-dispersion space for a given meta-atom height.

The Columbia team has experimentally realized broadband achromatic meta-lenses, operating in the near-infrared (Fig. 2) using meta-atoms shown in Fig. 1c. As the meta-atoms provide the largest possible coverage of the phase-dispersion space given the meta-atom height, their meta-lenses based on a single nanostructured thin film reach performance near the theoretic limit: the tightest focal spot over the largest wavelength range.

Metasurface triplets for controlling optical wavefronts over a large angular range

Singlet metasurfaces such as the ones described in the previous section control the wavefront of light incident to the metasurface in the normal direction but are not able to perfectly focus light propagating along off-axis directions. The Columbia team has designed and demonstrated meta-lens triplets that can focus a broad spectrum of light incident over an extended angular range. The phase profiles of the metasurface triplet are determined by using an optimization scheme. Fabricated elements of the metasurface triplet (M_1, M_2, and M_3) and assembled the triplet are shown in Fig. 3a. Results of broadband, wide-angle focusing are shown in Fig. 3b. It is observed that the focal spots are without large distortion up to an incident angle of ±20^o over λ=1.3-1.6 μm (distortion to focal spots starts to appear at an incident angle of 25^o at short wavelengths). They have conducted imaging in the near-infrared using the metasurface triplet. Figures 3c, d show that the image quality is largely maintained when switching from a λ=1.55 μm diode laser to a Halogen lamp that provides broadband infrared illumination, which demonstrates satisfactory chromatic aberration correction. Figures 3e, f show that clear images can be formed within a field of view of ±20^o with broadband illumination, demonstrating the ability of the triplet to suppress monochromatic aberrations within that angular range.

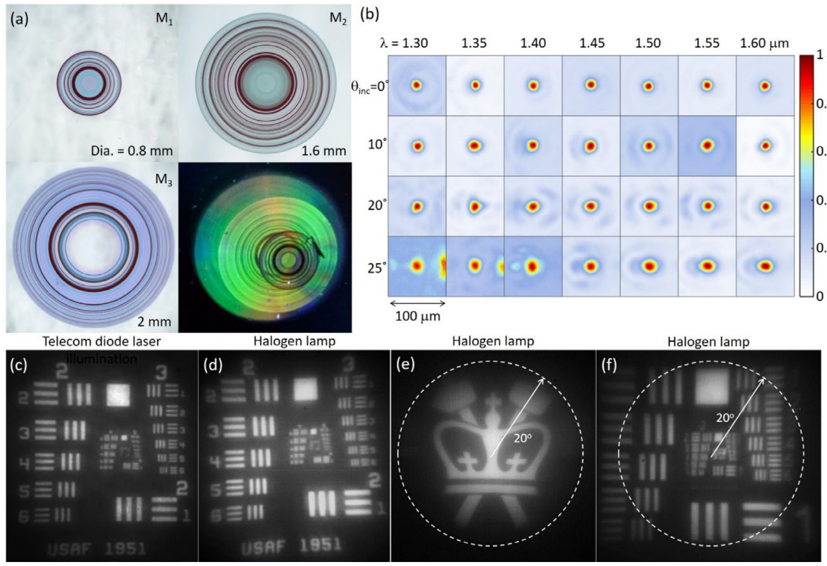

Fig. 3 (a) Optical images of fabricated elements of a metasurface triplet and the assembled triplet. The library of meta-atoms used is illustrated in **Fig. 1c**. (b) Measured focal spots at various incident angles and wavelengths. (c, d) Images of a USAF target taken by the triplet with a telecom diode laser and with an unpolarized broadband near-infrared source (a Halogen lamp with visible portion of the spectrum attenuated), respectively. (e, f) Images taken with the Halogen lamp up to a field of view of ±20^{o}.

Holographic manipulation of complex optical fields

Creating a complex optical field where each point of the space has an arbitrarily controllable combination of optical phase and amplitude is a “holy grail” of free-space optics. The Columbia team has been pursuing this “holy grail” of controlling complex optical fields at more than one color of light by investigating the interactions between light waves and metasurfaces composed of complex meta-atoms. Complete and independent control of optical amplitude and phase at one wavelength has been demonstrated by utilizing rectangular dielectric meta-atoms with two degrees of freedom in their geometry (Fig. 4a). Here, structural birefringence of the meta-atoms controls the amplitude of converted light from circular polarization of one handedness to the opposite handedness; the in-plane orientation of the birefringence axis controls the phase of the converted light via the “geometric phase” or Pancharatnam-Berry phase. The Columbia team has demonstrated “artifact-free” 2D metasurface holography, with markedly higher image fidelity compared to phase-only approaches (Fig. 4b). They have shown that the phase and amplitude of a holographic object can be encoded separately, allowing, for instance, identical intensity distributions but distinct phase distributions (Fig. 4c). They have shown that the ability to encode phase and amplitude separately enables creating 3D holographic objects with high fidelity (Fig. 4d) and controlling the surface texture of the objects (Fig. 4e). In another work, the Columbia team has used an additional degree of freedom, the freedom of choosing the complex cross-sectional shapes of dielectric meta-atoms (Figs. 5a, b), to control phase dispersion and demonstrate complete and independent control of four optical parameters: phase and amplitude for two colors of light at each point in the free-space (Fig. 5c).

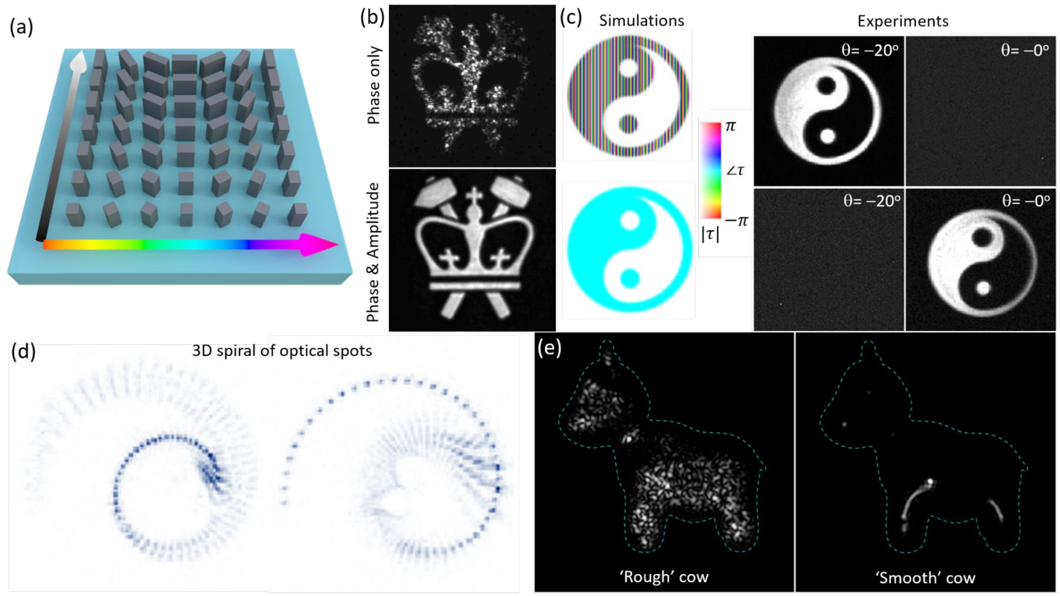

Fig. 4 (a) Two degrees of freedom in the geometry of meta-atoms (aspect ratio and orientation angle) allow for realizing full control of two optical parameters: amplitude and phase at one wavelength. (b) Experimental comparison of 2D images generated by a conventional phase-only metasurface (top) and by a phase-amplitude metasurface (bottom). (c) Simultaneous encoding of amplitude and phase in a holographic image. While the holographic image intensity distributions are indistinguishable between the two examples on the top and bottom rows, the optical phase profiles are distinct (i.e., one has a phase gradient and the other has a constant phase). (d) Visualization of a 3D spiral of optical spots created by a phase-amplitude metasurface at two focal planes of the camera. (e) Phase-amplitude metasurfaces enable creating 'rough' and 'smooth' 3D holographic cows (i.e., mimicking diffuse and specular reflection from the cow).

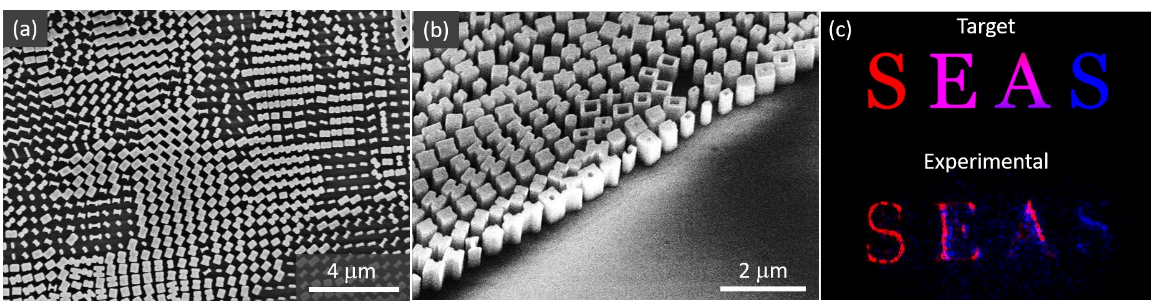

Fig. 5 (a) and (b) SEM images of a metasurface consisting of Silicon meta-atoms and capable of completely and independently controlling the phase and amplitude at two colors of light (four optical parameters). (c) Target and experimental two-color holographic images.

Integrated photonic devices based on metasurfaces *(in collaboration with the Loncar Group, Harvard)*

The Columbia team has achieved pure-phase modulation of light in the visible spectrum within a device footprint of ~10 μm ×10 μm. Pure-phase modulation refers to the scheme where optical phase is changed continuously over 2π while the amplitude of the optical signal has minimal variations. This function is essential for applications such as holographic display, light detection and ranging (LIDAR), and augmented reality/virtual reality (AR/VR) glasses. Because of the small refractive index change (induced by either thermo-optic or electro-optic effect) of available materials in the visible spectrum, conventional phase modulators based on waveguides demand a long propagation length, typically in the range of 1–10 mm. The Columbia team demonstrated that by using integrated, miniature optical resonators (e.g., adiabatic micro-rings) operating in the strongly over-coupling regime, a 2π pure-phase modulation can be achieved across an optical resonance (Fig. 6). The experimentally demonstrated devices offered more than one-order-of-magnitude reduction in both device footprint and power consumption compared to conventional waveguide-based phase modulators. This scheme promises compact, energy-efficient, fast pure-phase modulation, and enables large-scale integration of 1D or 2D optical phased arrays on compact nanophotonic chips for dynamic arbitrary wavefront generation.

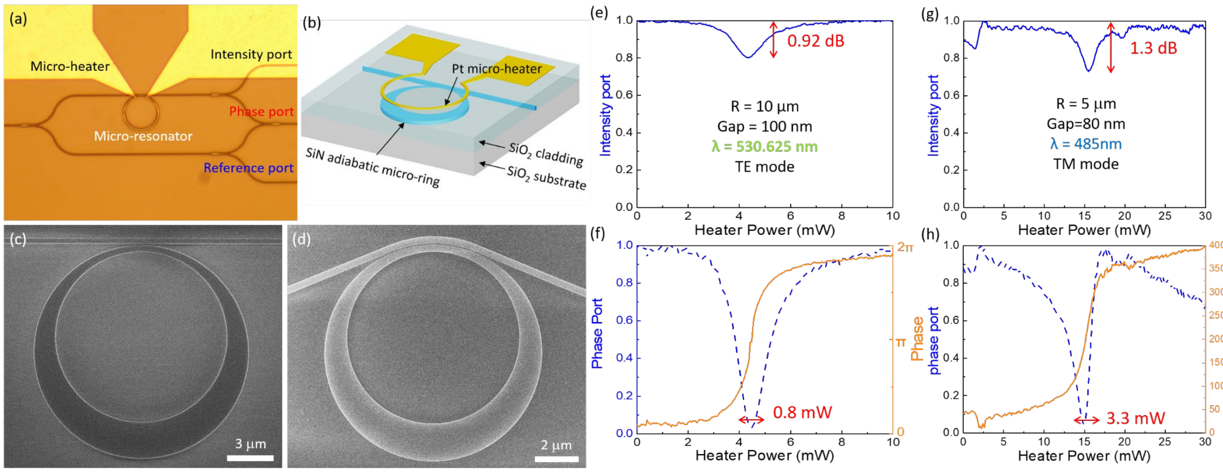

Fig. 6 Micro-resonators operating in the strong over-coupling regime for pure phase modulation. (a) Photo of a device based on adiabatic micro-ring loaded on one arm of a Mach-Zehnder interferometer. (b) Schematic of one device. (c) and (d) Scanning electron micrographs of two devices working at the green and blue wavelengths. (e, f) and (g, h) Measured signals from the intensity and phase ports of a device based on adiabatic micro-ring resonators at the green and blue wavelengths. Orange curves are extracted optical phase responses as a function of heater power.

In another work, the Columbia team experimentally demonstrated the smallest and most broadband photonic integrated devices (including waveguide mode converters, on-chip polarization rotators, on-chip perfect absorbers), where metasurfaces are used, for the first time, to control light propagating in waveguides. The metasurfaces control waveguide modes via strong optical scattering at subwavelength intervals; the unidirectional phase gradient, or effective wavevector, provided by the metasurfaces enables one-way transfer of optical power from one waveguide mode to another. These two effects make it possible to substantially shrink device footprints and broaden their operation bandwidth. Some of the demonstrated waveguide mode converters, for example, are just 1.7 times of the free space wavelength (Fig. 7a) and can tolerate wavelength variations as large as ±20%. Furthermore, devices based on dielectric metasurfaces have negligible insertion losses (Figs. 7e,f). Such small-footprint, broadband, and low-loss photonic integrated devices are highly desirable for photonic integrated circuits.

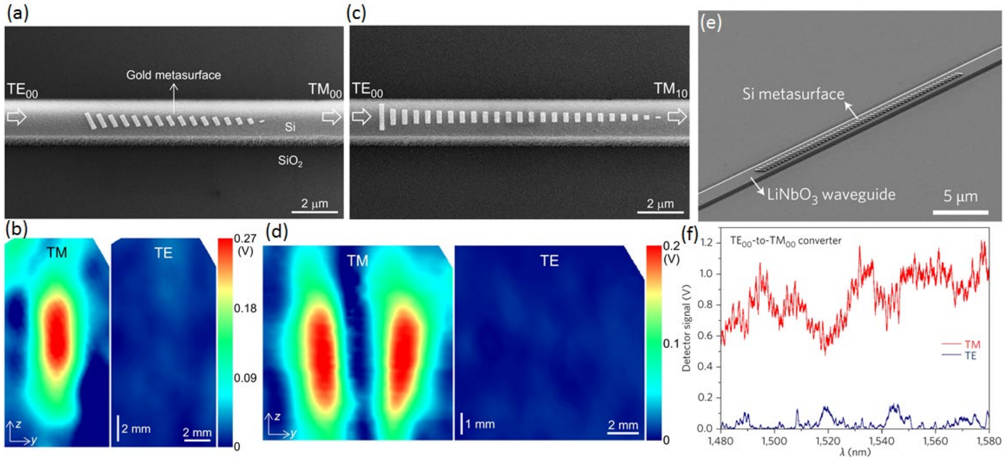

Fig. 7 Small-footprint, broadband waveguide mode converters based on phase-gradient metasurfaces. (a) and (c) SEM images of a TE_{00}-to-TM_{00} mode converter (on-chip polarization rotator) and a TE_{00}-to-TM_{10} mode converter, respective, based on plasmonic metasurfaces. (b) and (d) Measured far-field emission patterns of the two devices, respectively, showing complete conversion from the incident TE fundamental waveguide mode to the TM-polarized output modes. (e) SEM image of a polarization rotator based on dielectric metasurfaces. (f) Measured transmission spectra of the device, showing that polarization rotation is realized over a broad wavelength range.

Porous polymer coatings for highly efficient passive daytime radiative cooling

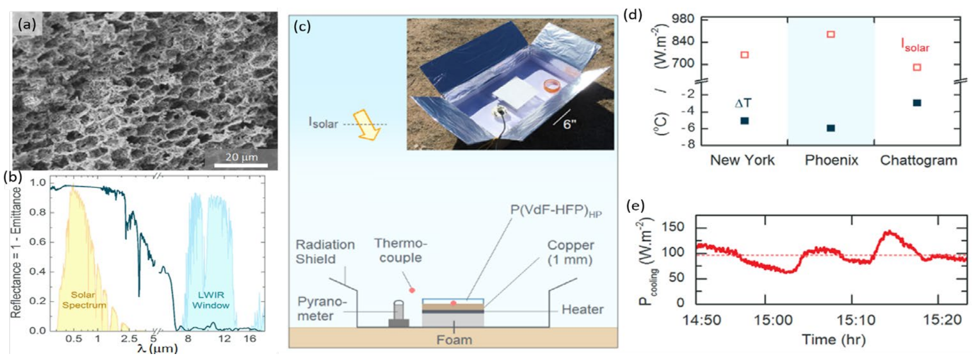

Fig. 8 Porous PVDF coating with optimal radiative cooling properties. (a) SEM image of the porous polymer coating containing a high density of air voids. (b) Spectral reflectance of a 300-μm thick radiative-cooling coating. (c) Schematic of the experimental setup used for testing the thermodynamic properties of PVDF coatings in the field. Inset: Photo of the setup. (d) Average solar intensity and sub-ambient temperature drops (ΔT) of PVDF coatings in New York, Phoenix, and Chattogram. (e) Measurements showing a cooling power of about 100 W/m^2 in the Phoenix field study.

Passive daytime radiative cooling (PDRC) involves spontaneously cooling a surface by reflecting sunlight and radiating heat to the cold outer space. The Columbia team has invented a simple, inexpensive and scalable phase-inversion-based method for fabricating hierarchically porous polyvinylidene fluoride-co-hexafluoropropene) or PVDF coatings with excellent PDRC capability. High, substrate-independent hemispherical solar reflectance (0.96 ± 0.03) and long-wave infrared (LWIR) emittances (0.97 ± 0.02) (Fig. 8b) allow for sub-ambient temperature drops of ~6°C and cooling powers of ~96 W/m^2 under solar intensities of 890 and 750 W/m^2, respectively (Figs. 8dd, e. The performance equals or surpasses those of state-of-the-art PDRC designs, while the technique offers a paint-like simplicity.

6. Correlated oxide $SmNiO_3$ as a new materials platform for broadband tunable photonics
(in collaboration with Ramanathan's group, Purdue)

The Columbia team has discovered a new optical phase-transition material samarium nickelate ($SmNiO_3$), which exhibits electron-doping induced phase transition between an opaque and a transparent state over the entire visible, near-infrared, and mid-infrared spectral bands (Fig. 9b). The phase transition is due to strong electron correlation, a quantum mechanical phenomenon in which electron doping profoundly modifies the band structure of $SmNiO_3$ by increasing its bandgap by an order of magnitude from ~100 meV to 3 eV.

The Columbia team has experimentally demonstrated free-space narrowband optical modulators based on thin-film $SmNiO_3$ integrated with metasurface structures (Figs. 9c-f). In this device the cross-aperture antennas interact strongly with incident light waves resonant to the antenna structure, leading to strong enhancement between the phase-change material and light of the resonant wavelength and thus strong optical modulation at this wavelength. This is the first investigation of correlated perovskites in active photonic device applications.

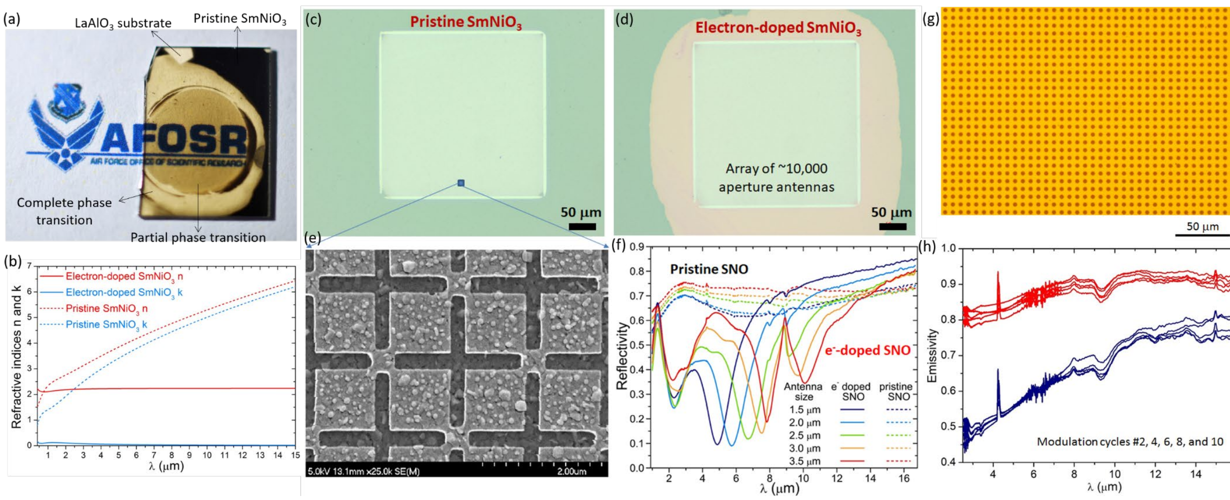

Fig. 9 Active photonic devices based on $SmNiO_3$ metasurfaces. (a) Optical image of a wafer placed on top of an AFOSR Logo. The wafer consists of an 80 nm $SmNiO_3$ thin film deposited on a 500 μm $LaAlO_3$ substrate. (b) Complex refractive indices (n and k) extracted from experiments. Pristine $SmNiO_3$ has high electric conductivity and is an optically opaque dielectric. Electron-doped $SmNiO_3$ is electrically insulating and optically transparent. (c, d) Photos of a narrowband optical modulator at two states of $SmNiO_3$. (e) SEM image of part of a device consisting of Pt cross apertures 2 μm × 2 μm in size patterned on $SmNiO_3$. (f) Measured reflection spectra of the device where $SmNiO_3$ phase transition was induced by hydrogenation and de-hydrogenation. (g) Photo of a variable emissivity metasurface, showing a gold plasmonic hole array patterned on a $SmNiO_3$ film. (h) Reflection spectra measured from the devices when $SmNiO_3$ is switched between its opaque and transparent states. Blue curves correspond to transparent $SmNiO_3$ (electron-doped state) and red curves correspond to opaque $SmNiO_3$ (pristine state).

The Columbia team has experimentally realized large dynamic tuning of emissivity over a broad infrared wavelength range in a metasurface integrated with phase-transition complex oxide $SmNiO_3$ (Figs. 9 g, h). The phase transition of $SmNiO_3$ is triggered by electrochemical reactions, where water dissolved with KOH is used as the electrolyte. A forward bias voltage generates protons through the electrolysis of water molecules; the protons together with an equal number of electrons are doped into the $SmNiO_3$thin films and switch pristine $SmNiO_3$ into its electron-doped, or optically transparent state. A reverse bias voltage draws protons along with electrons away from the $SmNiO_3$ thin-films, and thus $SmNiO_3$ is switched back to the pristine, or opaque, state. Modulation of emissivity of ~0.3 in the short-wavelength mid-infrared range (λ=3-5 μm), and 0.15-0.2 in the long-wavelength mid-infrared range (λ=8-13 μm) have been demonstrated experimentally (**Fig. 9h**). The thickness of $SmNiO_3$ thin-films used is ~80 nm and the switching time is roughly two minutes.

Purdue Team
co-PIs: V. M. Shalaev and A. Boltasseva, non-PI member: A. V. Kildishev

The Purdue team has pursued a broad range of research with breakthroughs in metasurfaces utilizing non-conventional plasmonic material (such as nitrides), tunable control of metasurface nanocavities using deep subwavelength spacings, epsilon near zero (ENZ) metasurface design and giant Kerr nonlinearities in ENZ metasurfaces, spatiotemporal light control with frequency-gradient metasurfaces; synchrotron radiation from nonlinear polarizations in metasurfaces and a number of novel devices such as fractal metasurface photodetectors.

***Boltasseva** (with V. Shalaev): Plasmonic Ceramic Materials for Metasurfaces*

Robust and high-temperature stable (refractory) transition metal nitrides are emerging nanophotonic materials for durable, CMOS-compatible applications. We experimentally demonstrated phase manipulating optical metasurfaces that exhibit a photonic spin Hall effect utilizing titanium- and zirconium nitrides (Fig. 10). In the developed all-nitride system, metal nitrides are combined with dielectric nitrides such as aluminum nitride and silicon nitride to design a highly anisotropic, multilayer resonator geometry that supports gap plasmons and enables high power efficiency (~40%) and broad bandwidth of operation in the near-infrared (NIR) wavelength region. A one-dimensional phase gradient created by geometric rotations of the resonators leads to simultaneous, spatial separation of right and left circular polarization as well as different frequency components of the incident light.

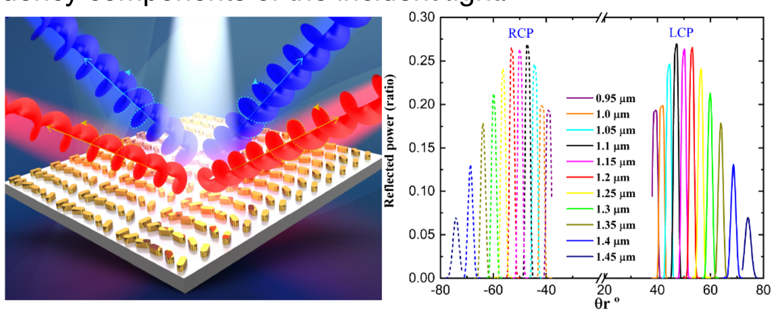

Fig. 10: Left: schematic of the metasurface exhibiting photonic spin Hall Effect (SHE) by separating the two circular polarizations (or photonic spins) in opposite angular directions. Right: experimentally measured reflected power collected as a function of reflection angle, from the fabricated TiN based metasurfaces for different frequency incident beams with left or right circular polarization.

***Boltasseva** (with Y. Gogotsi, Drexel University): Plasmonic MXene for Metasurfaces*

An emerging class of 2D transition metal nitrides/carbides, namely MXenes, has been studied for applications in flat optics.

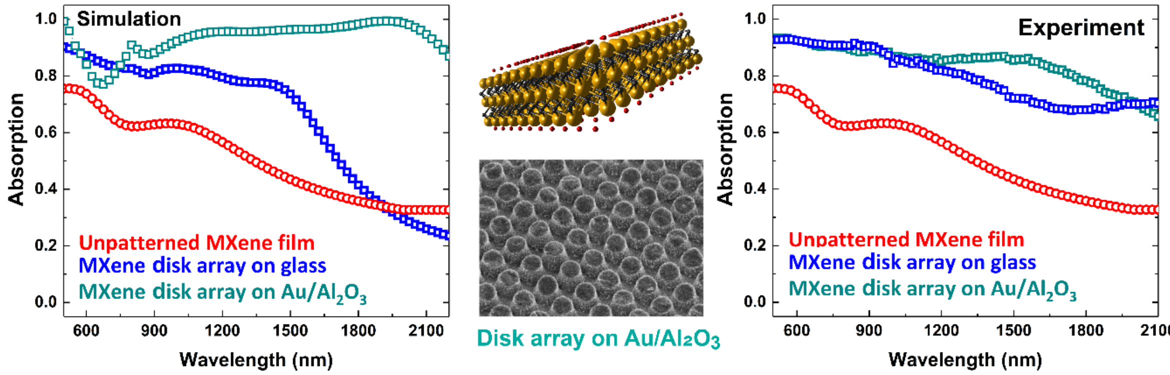

Fig. 11: Highly Broadband absorber using plasmonic MXene $Ti_3C_2T_X$. Left: simulation comparison of absorption spectra. Middle-top: Schematic of monolayer flake of two-dimensional $Ti_3C_2T_X$ MXene. Middle-bottom: Scanning electron microscope image of fabricated MXene disk array on Au/Al_2O_3 stack. Right: comparison of the experimentally measured absorption spectra.

Localized surface plasmon resonances were experimentally demonstrated in nanostructured films of 2D MXene Ti_3C_2 (Fig. 11). A planar design of highly broadband plasmonic absorber was implemented as a practical application of this new plasmonic material. As the material class and its synthesis techniques continue to mature, applicability in nanophotonics along with device performances are expected to improve further.

***Boltasseva** (with A. Alu, UT Austin): Controlling Light Polarization with TCO Metasurface*

Transparent conducting oxides (TCOs) are promising materials for nanophotonic applications due to their tunable optical properties. We designed and experimentally demonstrated a quarter-waveplate (QWP, converting linear polarized light to circular polarized light) using gallium doped zinc oxide (Ga: ZnO) over a wide wavelength range of 1.75 to 2.5 µm (Fig. 12). The optical property of the Ga: ZnO is tuned by post-growth annealing, as a result, the QWP operation bandwidth is experimentally shown to vary.

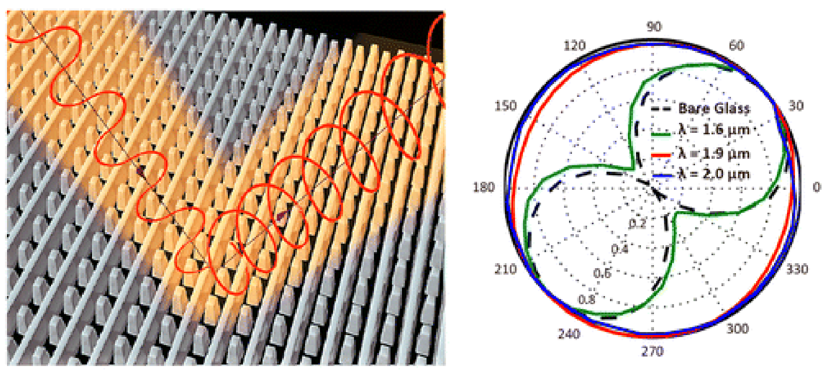

Fig. 12: Left: schematic of the TCO quarter-waveplate metasurface. Right: polarization state analysis for the reflected beam at λ = 1.6, 1.9, and 2.0 µm.

***Boltasseva, Shalaev** (with V M. Ferrera, Heriot-Watt University):*
Dynamic Control of Nanocavities with Tunable Metal Oxides

The operational wavelength of conventional Fabry-Perot nanocavities is not tunable because the phase accumulation is directly related to the wavelength and the cavity size. To realize tunable nanocavities, we implemented a static method with a passive plasmonic metasurface and a dynamic method using a TCO (Ga:ZnO) embedded in the nanocavities (Fig. 13). Static tuning was achieved by changing the design of the metasurface, and dynamic tuning is achieved by pumping the Ga:ZnO with pulsed laser near its epsilon-near-zero (ENZ) point.

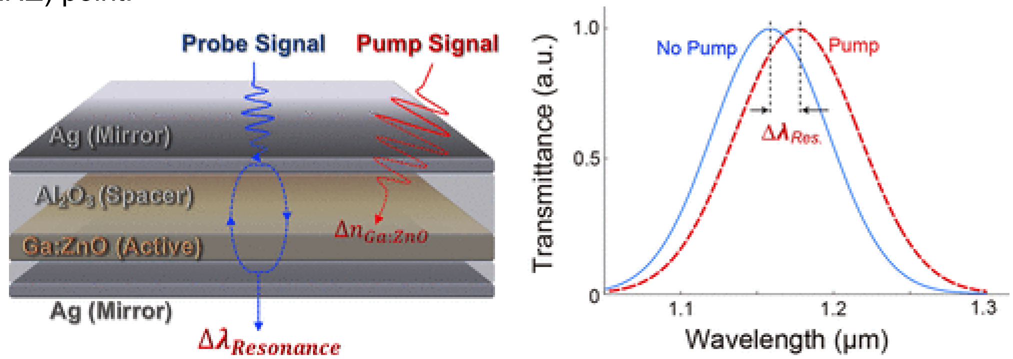

Fig. 13: Left: schematic of the Ga:ZnO embedded nanocavity. Right: measured transmittance spectrum with and without pumping, showing 15 nm shift in resonant wavelength.

Kildishev, Boltasseva, Shalaev:
Ultrathin, Multicolour Cavities with Embedded Metasurfaces

The size of conventional Fabry-Perot nanocavities is limited by the operating wavelength because light needs to accumulate a certain phase while propagating inside the cavity. We introduced a gap plasmon metasurface inside the cavity, which imparts an optical phase discontinuity to light thus greatly reducing the thickness required to accumulate the desired phase. We achieved functional nanocavities well below the conventional λ/2n thickness (Fig. 5). The operating wavelength can simply be tuned by changing the metasurface design, and we demonstrate wide palette of colors using such metasurface-embedded nanocavities.

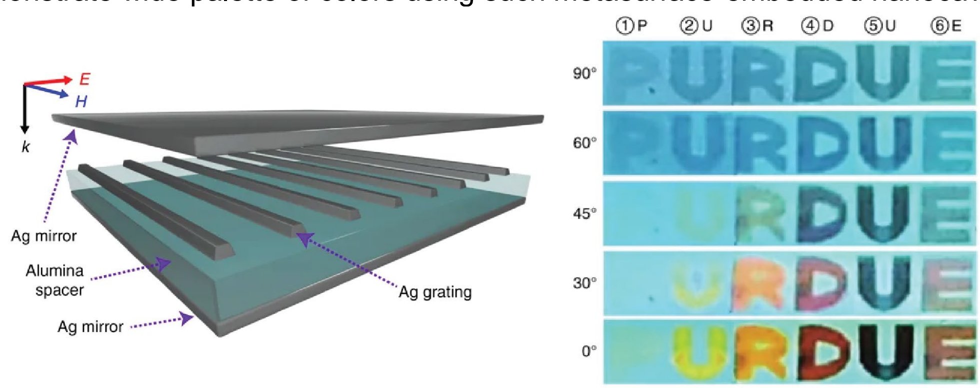

Fig. 14 Left: schematic of the metasurface embedded cavity. Right: transmission imaged with incident white light of different polarization angles.

Boltasseva, Shalaev *(with M. Ferrera, Heriot-Watt University)*
Controlling Hybrid Nonlinearities in TCOs via Two-Colour Excitation

We investigated the carrier dynamics of aluminum-doped zinc oxide (AL: ZnO or AZO) using pump-probe technique. Specifically, we studied the inter-band dynamics by using a pump at 262 nm, and the intra-band dynamics using a pump at 787 nm. In both cases, the probe wavelength is set at 1300 nm, near AZO's ENZ point. We showed that both inter- and intra-band excitations induce sub-ps recombination dynamics, and a strong modulation in amplitude (above 30%) with opposite signs (Fig. 15).

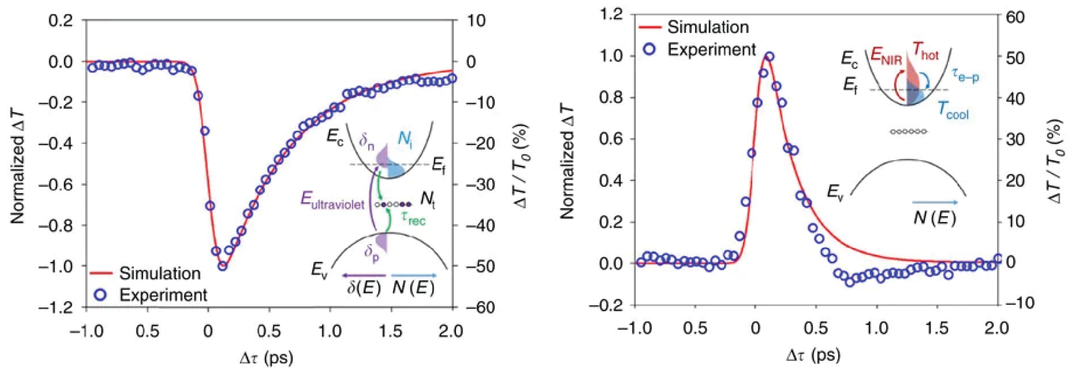

Fig. 15: measured recombination dynamics (transmission change at λ_{probe} = 1300 nm) of inter-band (left, λ_{pmup} = 262 nm) and intra-band (right, λ_{pump} = 787 nm) excitation.

Shalaev, Boltasseva *(with S. Bozhevolnyi, Denmark):*
Epsilon-Near-Zero Materials for Metasurfaces

We explored the effects of ENZ films of AZO on single and dimer plasmonic antennas. For thick AZO films, we developed an accurate and efficient semi-analytical model for calculating resonances and near-fields of single antennas on dispersive substrates which strongly agrees with our observations of resonance pinning effects. Ultrathin TCO support unique ENZ modes which correspond to the excitation of long range plasmons. Here, we investigated the coupling of single plasmonic antennas with ENZ modes in 23-nm-thick AZO films (Fig. 16).

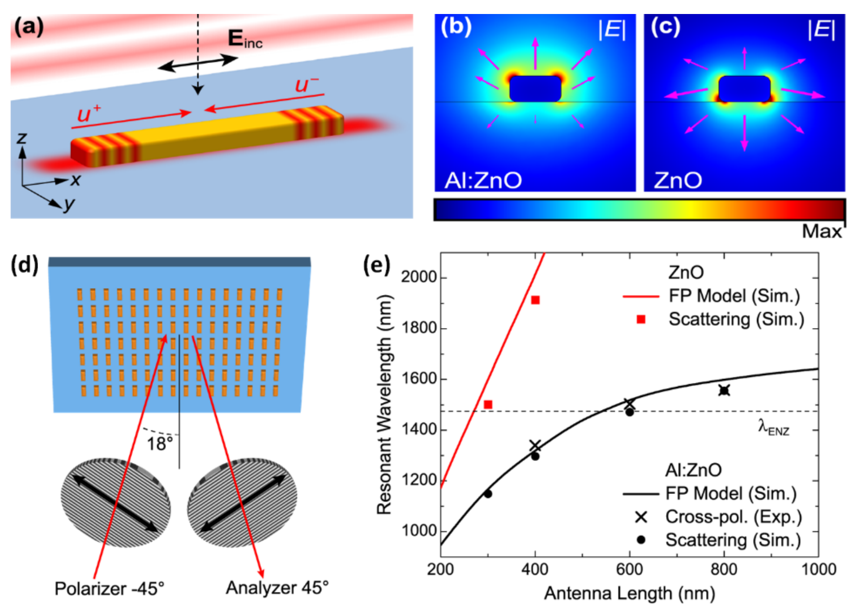

Fig. 16: Semi-analytical FP model for a single nanorod. (a) Sketch of a nanorod upon normal illumination, exciting two counter-propagating nanorod modes. (b, c) Electric field distribution of nanorod waveguiding mode at 1475 nm, deposited on (b) an Al: ZnO and (c) a ZnO substrate. Far-field characterization of nanorod arrays. (d) Cross-polarized configuration used for measuring the far-field scattering of the single antenna arrays. (b) Resonant wavelength as a function of antenna length for the Al: ZnO (black) and ZnO (red). The dashed line indicates the ENZ wavelength of 1475 nm.

Shalaev, Boltasseva, Kildishev
Enhanced Graphene Photodetector with Fractal Metasurface

We used a snow-flake shaped fractal metasurface to enhance the sensitivity of graphene photodetectors. Due to its complex structure, the metasurface achieves a broadband optical absorption in the visible range, and the optical response is insensitive to the polarization of the incident light (Fig. 17). Therefore, the measured photodetection sensitivity enhancement ranges from 7-14X, and in a polarization-independent manner over the visible range.

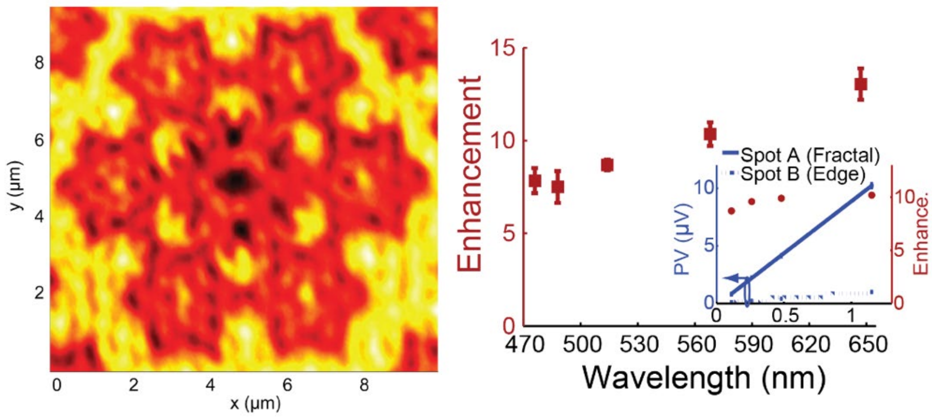

Fig.17: Left: measured near-field E-field distribution when the fractal metasurface is excited by 532 nm light. Right: measured enhancement in photovoltage (PV) from the metasurface in the visible range.

Shalaev, Boltasseva

Enhancing Graphene Photocurrent Using Surface Plasmons and p-n Junction

Graphene photodetection is severely limited by its low sensitivity. In graphene, the photo-carriers are generated by first converting light to heat and then heat to electricity. We designed a structure that simultaneously enhances the light-to-heat (via gap plasmon structure) and heat-to-electricity (via gate-induced p-n junction) conversion efficiencies in graphene photodetector, and experimentally achieved 25X enhancement in photo-sensitivity (Fig. 18).

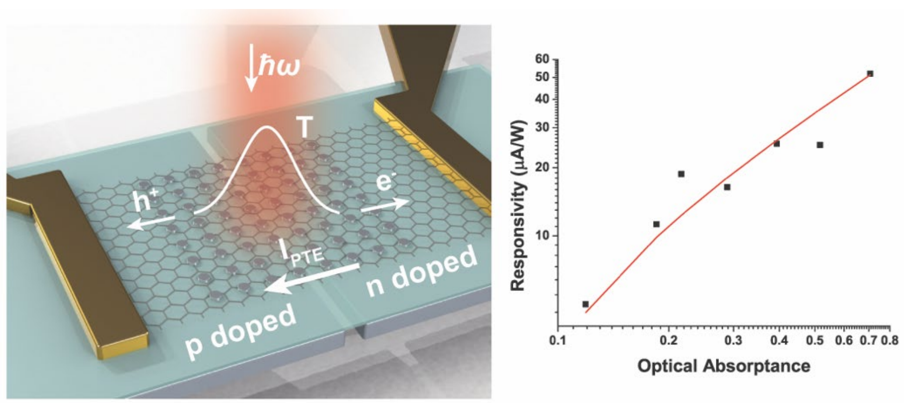

Fig. 18: Left: schematic of the proposed graphene photodetector design, consisting of a gap plasmon structure and a p-n junction. Right: measured responsivity versus optical absorption.

Shalaev *(with A. Boltasseva): Quantifying Nanoscale Plasmonic Heating*

We used optical thermoreflectance imaging – a thermal imaging method based on the temperature-dependent surface reflectivity of materials – to study the plasmonic heating behavior of plasmonic structures. This method achieves a higher spatial resolution than conventional thermal camera imaging and does not require special sample preparation. We used time-domain thermoreflectance to study the transient heat dissipation in the ns scale and revealed the effect of nanostructure's size on its temperature decay speed (Fig. 19).

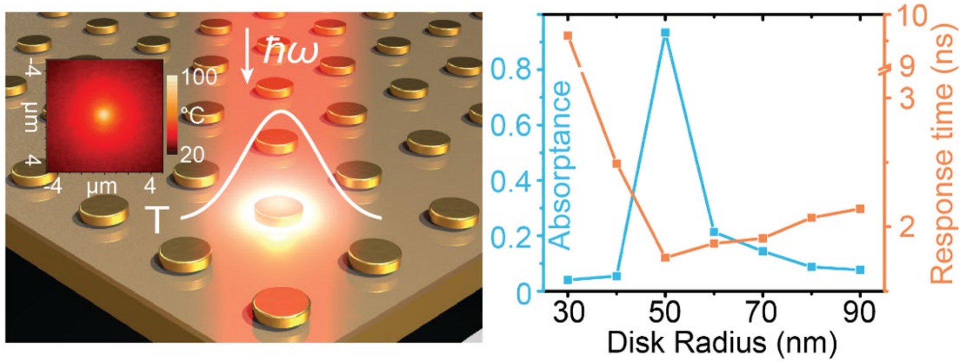

Fig. 19: Left: schematic of the gap plasmon structure and (inset) an experimental thermal image obtained via optical thermoreflectance imaging. Right: numerically fitted optical absorptance (blue) and temperature decay speed (yellow) versus nanostructure size.

Shalaev *(with M. Brongersma, Stanford)*
Spatiotemporal Light Control with Frequency-Gradient Metasurfaces

We realized continuous steer of light using a passive frequency-gradient metasurface and a frequency-comb light source. The metasurface redistributes different frequency components of the incident light, and they constructively interfere to achieve rapid beam steering. The steering speed is controlled by the frequency gradient, and we realized 25° steering in just 8 picoseconds (Fig. 20).

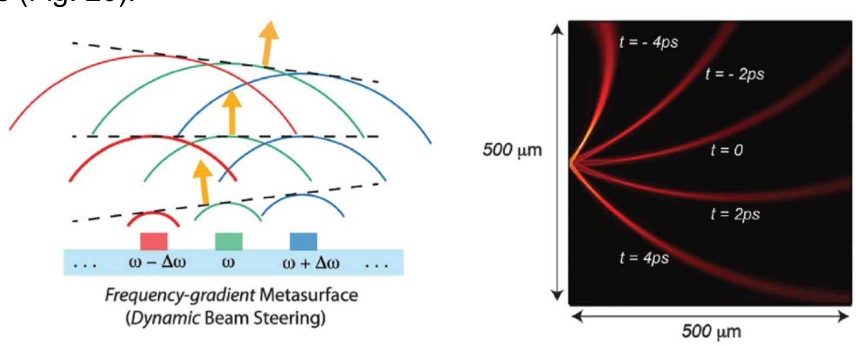

Fig. 20: Left: principle of beam steering using frequency-gradient metasurface. Right: light generated at different time instants by our designed frequency-gradient metasurface.

Shalaev, Boltasseva *(with R. Merlin, U. Michigan)*
Synchrotron Radiation from an Accelerating Light Pulse

We studied the synchrotron radiation emitted by charge particles traveling in a circular arc at relativistic speeds, using nonlinear optics (Fig. 21). A v-antenna metasurface is used to guide 800 nm laser pulses to propagate along a 100 μm radius arc inside a nonlinear crystal, and the pulses emit THz frequency radiation via difference frequency generation (DFG) nonlinear polarization. Due to the dispersion of the crystal, the 800 nm light pulse propagates 3 times faster than the THz nonlinear polarization, therefore the radiation pattern from the light pulse resembles that of a *superluminal* synchrotron radiation generated from a millimeter-scale chip.

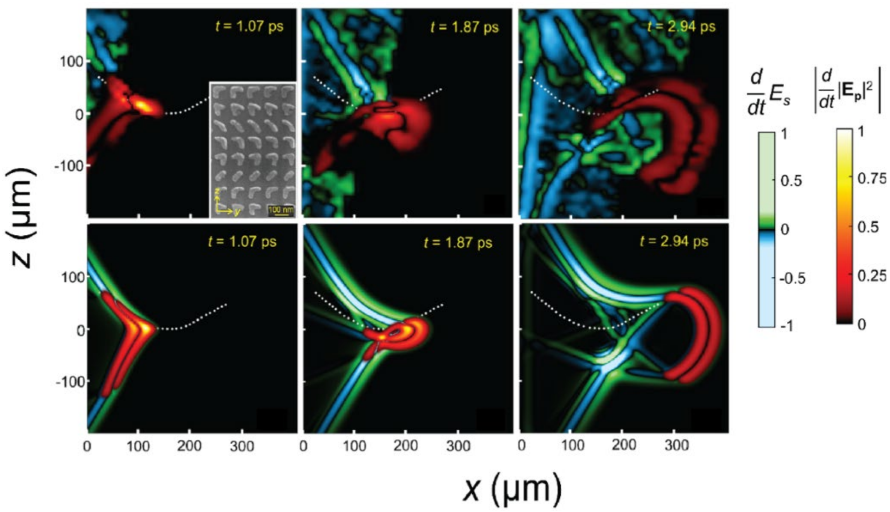

Fig. 21: Measured (top row) and calculated (bottom row) light pulse (yellow-red color scale) traveling in an arc of 100 μm radius, and its THz radiation field (green-blue color scale), at different instants. Inset shows part of the metasurface that guides the light pulse to propagate in the circular arc.

Kildishev, Boltasseva, Shalaev

Polarization Tunable Color Encoding in Metasurfaces for Encryption

We proposed an all-aluminum metasurface for dynamic optical displays and high-density data storage. (Fig. 22) This metasurface is composed of aluminum nanoantennae attached on aluminum back reflector. When illuminated with broadband light, such metasurface reflects a broad palette of colors with different combinations of polarizer and analyzer angles. Based on this feature, numerous information states can be stored in the orientation of the nanoantennae, and customized color codes can be created to enable high-density data storage with speedy read-out manner. The system theoretically achieves a 5% increment in storage capacity and 143X enhancement in readout speed compared to current Blu-ray technology.

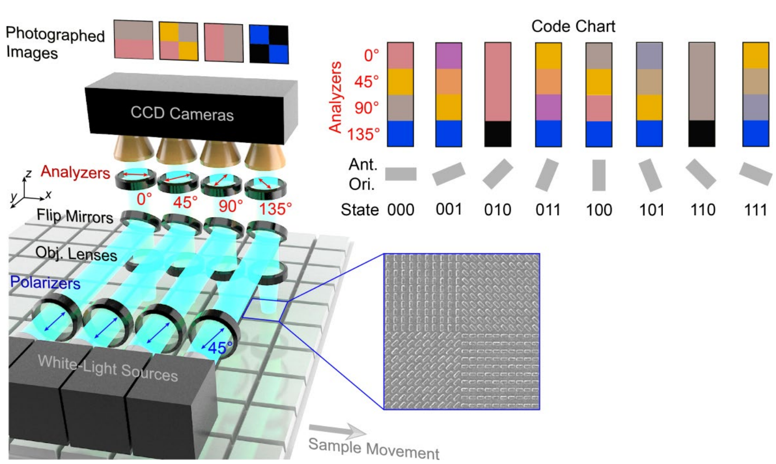

Fig. 22: Different information is stored by the orientation of the aluminum nanoantennae. By pre-programming the polarizer and analyzer angle, various color codes are created by scanning the sample.

Brongersma Group

The Brongersma group has led effort within this MURI team to create a variety of multifunctional and dynamic metasurfaces. A major effort at the beginning of the program was devoted to understanding the opportunities mechanical tuning of plasmonic and Mie resonant antennas. This was then used to create actively tunable lenses and beam steering devices later in the program. A collaboration with the Shalaev group also led to the development of an entirely new concept for optical beam steering that capitalizes on passive metasurfaces and frequency comb sources. Collaborations with the Fan and Yu groups also led to new ways of optical angle-sensing with Si antenna structures. The research led to many publications, including 4 high impact papers in *Science* and *1 in Nature Nanotechnology.*

Tuning of the light scattering properties of plasmonic antennas above a metallic mirror

Within this MURI, the group pursued the opportunity of using mechanical motion of optical antennas to tune their light scattering properties. They started by quantifying the sensitivity of the plasmonic and Mie resonances supported by metallic and semiconductor nanostructures to their spacing from a metallic mirror. The experimental configuration shown in Fig. 23 was used to explore this first for metal nanowires (NWs). Here, a metallic nanowire (NW) is essentially floated over a metallic substrate with a gap. It has been well established that a metallic nanostrip above a metal substrate can form a resonant metal-insulator-metal (MIM) nanocavity. Such cavities support strong, resonant modes for gap surface plasmons. Because these structures have at least one dimension comparable to the gap plasmon wavelength, their resonant properties are dominated by retardation effects rather than quasi-electrostatics. Therefore, intuitive design rules based on radiofrequency antenna design can be applied to such cavities. In this MURI, we develop this resonator concept by forming a floating NW geometry. As shown in Fig. 23 a, the structure can locally be viewed as a metallic nanostrip separated with a small gap from a metallic substrate; it can be termed a metal-air-metal (MAM) nanocavity analogous to a MIM nanocavity. This tapered experimental geometry offers a simple way to explore MAM resonances with gap sizes in the 50 nm – sub-10-nm range within one fabricated structure.

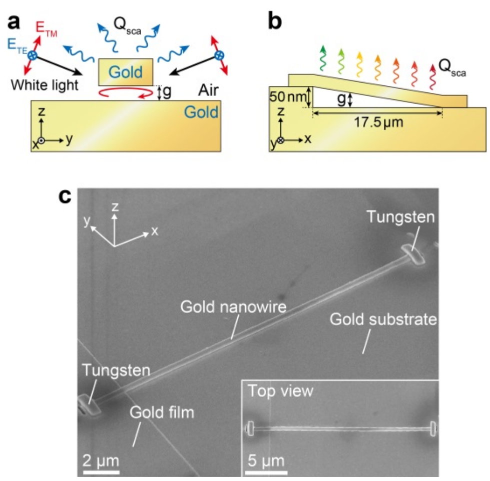

Fig. 23 Exploring optical antenna resonances of an individual 'floating' metal NW. (a, b) Schematic of the cross section (a) and side view (b) of a floating gold NW above a gold substrate. The dark field illumination configuration is shown. At various gap sizes between the NW and the metal substrate, surface plasmons resonantly oscillate in the gap. This produces strong light scattering at a set of resonant wavelengths that are tunable with the gap size. (c) Oblique scanning electron microscopy (SEM) image of a floating gold NW above a gold substrate. The NW width and thickness are 440 nm and 80 nm, respectively. Inset shows the top view.

The proposed structure (shown in Figure 23 a, b) is fabricated by a pick-and-place method in nanoscale dimensions within a focused ion beam tool. The pick-and-place method is based on template striping with a precisely controlled nanoprobe and has been used to obtain ultra-smooth pure metal films with three-dimensional shapes (i.e. bumps, grooves, and apertures). However, we now used this method for constructing a floating

NW geometry with metallic nanogaps. In fact, with this method, it is possible to form a smooth metallic nanogap by placing a stripped NW on a smooth metallic substrate with a gap because of an ultra-smooth surface of the NW bottom via a template effect in the stripping process.
To analyze plasmon resonance properties of the fabricated NW, we measured scattered light under the dark-field illumination. The illumination was polarized by a linear polarizer to be in either the transverse magnetic (TM) or transverse electric (TE) polarization defined in Figure 23 a. Figure 24 a, b shows dark-field images of the NW with w = 440 nm for TM and TE polarized illuminations. We observed that the NW shows different scattering colors from red to green along the wire-length-axis under TM illumination, while the NW shows only a green color scattering under TE illumination.

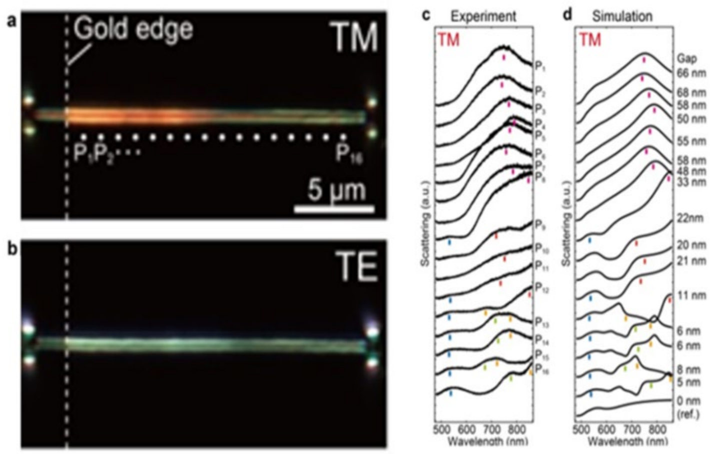

Fig. 24. Optical scattering observed from a gold NW above a gold substrate under dark-field illumination. (a,b) Dark-field light scattering images of a NW illuminated with TM (a) and TE (b) polarized light. The vertical dashed white lines represent the gold step edge. Experimental (c) and simulated (d) scattering spectra for TM polarized illumination. The spectra in experiment were measured at the sixteen positions of the NW indicated by the white dots in (a). The gap sizes that were used in the simulation are presented for each simulated spectrum. The colored dots in both (c) and (d) show the peak wavelengths.

A spectral analysis was performed by focusing on the scattered light from sixteen positions (P1-P16) on the NW indicated by white dots in Fig. 24a. Figure 24c shows the experimentally observed scattering spectra at each position for TM illumination. From these spectra, we clearly observed resonance peaks and the trend of their red-shift in the spectra as the position number increases from P1 to P16, highlighted by color dots in Figure 24c. When the MAM nanocavity is driven by TM polarized light, these obtained spectral shifts indicate the gap dependence of plasmon resonances along the NW. We also see weak peaks (blue dots) near the 550 nm wavelength and they never show the spectral shift, indicating the excitation of gap-independent resonance modes. Spectral analysis for TE illumination was also performed and these spectra show only one peak around 570 nm for all positions and the scattering intensities are roughly three-times smaller than those of TM illumination (not shown). In general, TE illumination cannot excite plasmon resonance modes, so these weak peaks can be attributed to the absorption band of gold. To understand the observed resonant behavior, we performed electromagnetic simulations and successfully developed intuitive models. Next, we demonstrate even greater tunability for semiconductor nanostructures.

Tuning of the light scattering properties of semiconductor antennas above a mirror

Recently there has been much interest in utilizing high-index dielectric and semiconducting nanostructures to efficiently confine and manipulate light at the nanoscale. Much work has focused on tailoring the size and geometry of these structures to achieve various optical phenomena such as spectrally-controlled and polarization absorption, light scattering, emission, Fano-type and Kerker resonances. Also metamaterials concepts such as negative refraction, and wavefront manipulation have been investigated. At the origin of the observed behavior are the optical resonances supported by high-index nanostructures and these have been analyzed by analytical Lorentz-Mie theory and numerical approaches such as finite difference methods and the discrete dipole approximation. Such treatments illustrate how electric and magnetic dipolar-like modes are supported through the excitation of displacement currents as opposed to free-electron currents in metal structures. In optimizing the modal properties for a specific application, one has primarily focused on tailoring the deep subwavelength structure to maximize modal excitation and to fashion the near-fields inside the structure.

As part of this MURI effort, the group analyzed how the scattering via the excitation of the optical modes of semiconductor nanowires can be enhanced or suppressed at different heights above a metal surface. We also demonstrated near-complete suppression of light scattering of specific modes due to the occurrence of surface selection rules for high-index nanoscatterers. This affords selective control over the excitation of specific multipolar modes.
For our light scattering measurements, silicon nanowires (SiNWs) grown via a gold colloid-catalyzed chemical vapor deposition process were deposited at a low density on a quartz substrate. This substrate was suspended above an aluminum-coated plano-convex fused silica lens (Fig. 25a). This configuration affords very precise, nanometer-scale control over the height of the NW above the mirror by sliding a quartz substrate perpendicular to the collection direction. Figure 25b shows representative dark field images of a 50-nm-diameter nanowire illuminated with a white light source using a dark field objective. The images show vibrant color-selective scattering when the height of the resonator is changed by only 140 nm.

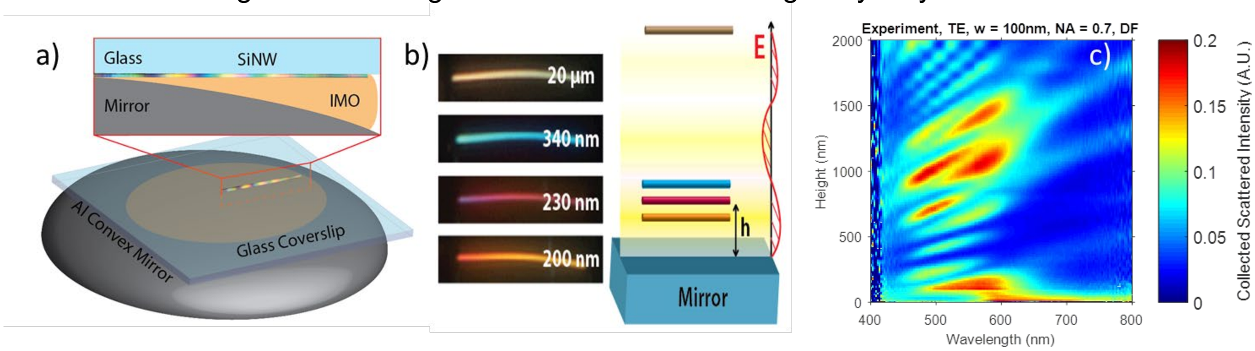

Fig. 25. Experimental layout for light scattering experiments above a mirror. (a) The schematic layout of the sample geometry. (b) Dark field optical microscopy images of a SiNW at various heights above the mirror. (c) Map of the scattered light intensity from a 100 nm diameter Si nanowire versus the illumination wavelength and height above a metallic mirror surface. Substantial changes in the light scattering spectrum can be observed with changing NW height.

There have been several studies aimed at examining the optical light scattering properties in the near-field regime where a semiconductor nanostructure is placed in very close proximity (d < 50 nm) to a surface. Here, significant frequency-shifts in the spectral scattering response are observed when the distance between the particle and substrate are changed. This behavior has accurately been captured by a Green's function method in which the nanostructure is treated in the point dipole approximation. Physically, these changes can be understood by viewing the scattering system to be a composite composed of the particle's dipole and its image dipole in the substrate. In the 'mid-field' and far-field regime, where the near-fields of the particle and substrate no longer overlap significantly, no such frequency shifts are expected. However, we found that for high-index nanostructures that support magnetic and electric dipolar resonances at different frequencies the changes in the scattering efficiencies for these distinct type of modes with height offer a very effective way to tune the light scattering spectra. Figure 25c shows a very significant modulation in the light scattering intensity with NW height. This modulation in the scattered light intensity can be attributed to the interference of the fields from the scattering dipole and those originating from the image dipole (i.e. reflected fields from the substrate). Under this MURI program the Brongersma group developed full-field simulation techniques and intuitive analytical models that accurately predict the observed changes in scattering seen in the experiments. From this work, it is clear that Si nanowires are ideal building blocks for mechanically-tunable metasurfaces and these will be discussed in the following section.

IV: The creation of dynamically tunable metasurfaces based on Mie resonators

One of the most notable accomplishments of the Brongersma group in this MURI program was the realization of a Si-based metasurface capable of dynamically tuning structural color and active beam steering. This work led to Science publication on both the fundamental tuning mechanism and the ability of dynamically steer and focus light. The operation of these metasurfaces was based on the highly tunable light scattering phase of Si antennas with their height above a reflecting surface. Si metasurfaces as shown in Fig. 26 a and b were suspended above a Si substrate and fabricated using standard silicon-on-insulator technology. These metasurfaces were incorporated in a frame so that they could be moved up and down using micromechanical movement at low actuation voltages (Fig. 26c). The interaction of the optical resonances supported in the suspended array with the Fabry-Pérot modes supported between the substrate and the array gave rise to vibrant changes of color in bright field reflection (Fig. 26c). The size of individual nanowires was judiciously chosen to afford highly tunable structural colors (Fig. 26d). For a similar device illuminated under dark-field illumination conditions, Brongersma showed that the scattered light can be temporally mixed between a linear combination of the colors at 0 and 1V by applying different duty cycles of the actuation voltage (Fig. 26e-f). Due to the capacitive actuation of these devices, they could be integrated into low-power reflective color displays.

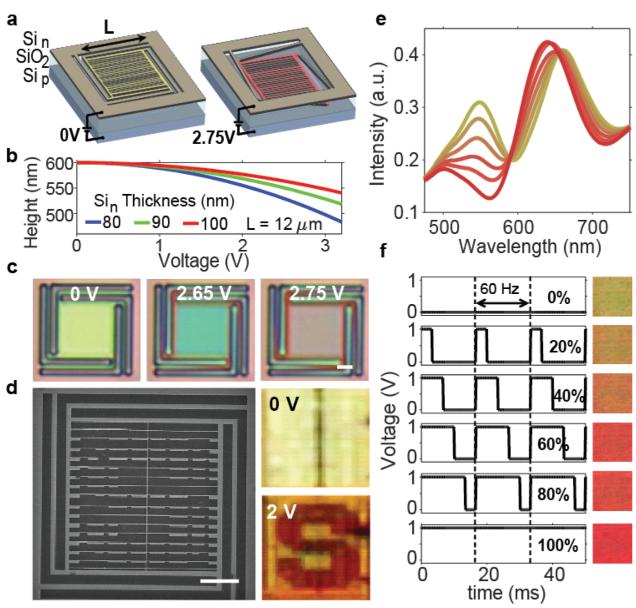

Fig. 26 (a) Schematic of the active metasurface device under a 0V (*left*) and 2V (*right*) bias. (b) Finite element simulation result of the active metasurface height as a function of applied bias for an arm length of 12 μm with various active layer thicknesses (c) bright field light scattering from a nanowire 100 x 100 nm nanowire array with a period of 300 nm (d) An active metasurface patterned with nanowires of various widths for tunable structural color (*left*) with bright field scattering images taken at biases of 0V (*top*) and 2V (*bottom*). (e-f) Temporally averaged time-multiplexed color mixing spectra from an active metasurface. The scale bars are 2 μm.

Leveraging their understanding of the tunable light scattering properties of Si antennas above a back reflector, the Brongersma group also constructed a metasurface capable of steering light beams. Here, a mechanically movable metasurface was created from Si nanowires with a spatial gradient in the beam diameter (Fig. 27a, b, and c). Again, the metasurface was suspended above a Si substrate and fabricated using standard silicon-on-insulator (SOI) technology. By applying a modest electrical bias (few volt) between the frame and surface the Si metasurface was moved. In this device, they leveraged the interplay of the optical, Mie resonances in the nanowires and the Fabry-Perot resonance between the metasurface and the Si substrate to control the scattering phase from each nanowire. With the graded nanowire width, a tunable phase gradient was achieved, and this enabled active beam steering. The types of elements can be used as active optical components for tunable lenses and LIDAR systems that can operate at low voltage and power.

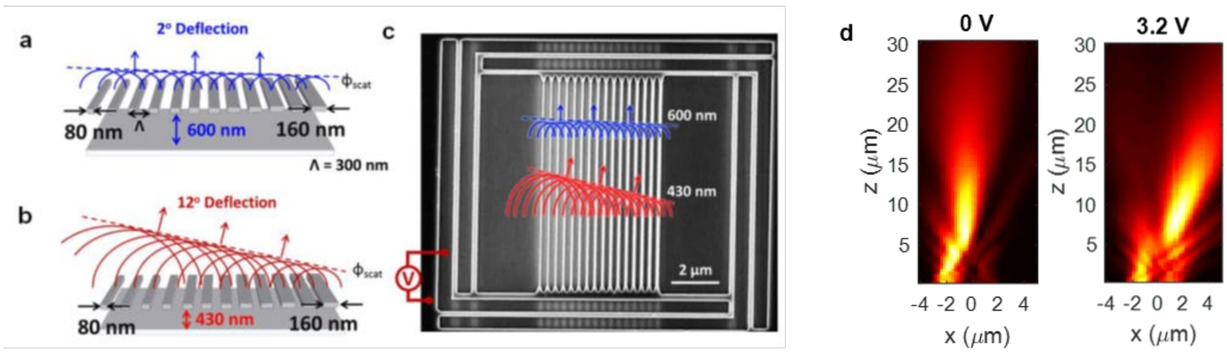

Fig. 27 Design of a beam steering device using a nanowire array with varying nanowire widths (a-b) Schematic representation of the beam steering device comprised of a nanowire array linearly increasing in width from 80 nm to 160 nm with a 100 nm thickness. The beam deflection spans from 2° to 12°. (c) Scanning electron micrograph of a fabricated device with 16 nanowires showing the linearly increasing nanowire width. The schematic overlay represents the scattered phase front shown in panels a and b. (d) Experimentally measured beam profiles of steered light from the Si metasurface at 0V and 3.2 V applied bias. The measurements were performed in a standard confocal microscope.

Dynamically tunable metasurfaces based on frequency metasurfaces *(with Shalaev, and Vuckovic groups)*

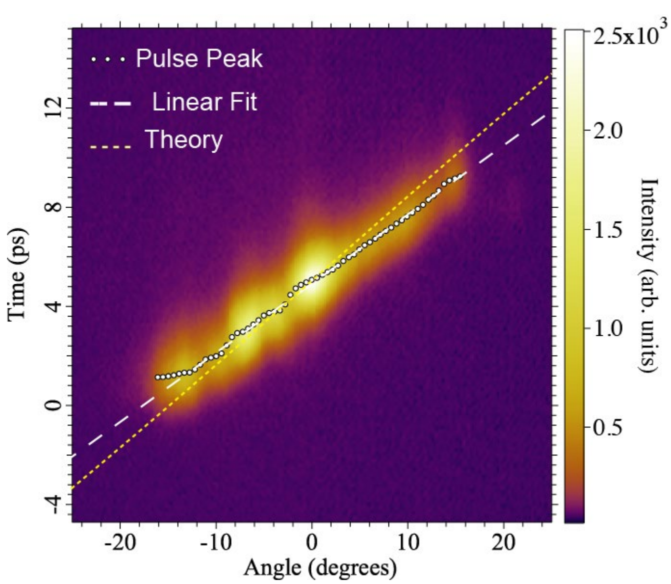

An entirely new approach to realize power-efficient metasurfaces was developed that offers full-phase modulation (0-2π) and operation at very high speeds. It is based on a virtual frequency-gradient metasurface. We generate it by illuminating a passive dielectric metasurface with a mode locked laser that features a frequency-comb spectrum. Spatiotemporal redirection of light naturally occurs as optical phase-fronts reorient at a speed controlled by the frequency-gradient across the virtual metasurface. An experimental realization of laser beam steering with a continuously changing steering-angle was demonstrated for the first time with a single metasurface over a 25 deg angle in just 8 ps (Fig. 28)

Fig. 28: Streak camera measurements of beam steering action obtained from a frequency-gradient metasurface. Here, each moment in time is mapped to its corresponding beam steering angle. It shows the angular redirection over 25° in 8 picoseconds. The white dots denote the peak locations for the pulse at each steering angle. The white dashed line shows the linear fit used to calculate the angular speed of beam steering. The yellow dashed line shows the theoretical prediction that was developed.

This work shows the path towards integrated solutions for ultrafast spatiotemporal light control by fusing the best of non-power-consuming, passive metasurfaces and advanced frequency-comb sources.

Angle-dependent photodetectors *(collaboration with Fan (Stanford) and Yu (Columbia) groups)*

A subwavelength photodetection pixel was realized that can measure both the intensity and the incident angle of light. It consists of two nanoscale Si nanowire resonators, which serve the equivalent role of the two eardrums. They can internally circulate light to produce standing electromagnetic waves in an analogous way as an eardrum hosts standing mechanical vibrations. Because of the high refractive index of semiconductors, the sizes of resonators and their separation can be much smaller than the free-space optical wavelength. By electrically contacting each nanowire to form photodetectors, they afford measurement of the internally stored optical energy through simple photocurrent measurements. The team showed that the two electrically-isolated and optically-coupled photodetectors allow angle-sensing by monitoring the difference in stored energy between the resonators. The angular resolution for this device was less than 1 degree for subwavelength pixel. This work led to a publication in Nature Nanotechnology.

Capasso Group

The Capasso group has made important advances in several of the MURI thrusts.

Metasurface Platforms: Flat optics including high NA diffraction limited metalenses in the visible; large area metalenses by stepper lithography; achromatic metasurface optical components by dispersive phase compensation; first broadband achromatic lens across the entire visible; hybrid metasurface refractive lenses; dynamic metalenses based on MEMS; adaptive metalenses with voltage controlled focus and aberrations; miniature high-resolution spectrometers and optical endoscopes; novel polarization optics with applications to polarimeters and single shot full-Stokes polarization sensitive cameras.

Physics of Metasurface Devices: Metasurfaces for arbitrary mapping from spin angular momentum to optical angular momentum; Cherenkov surface plasmons with a one-dimensional metamaterial; chiroptical metasurfaces with giant circular dichroism; metasurfaces with wavelength-controlled functionalities.

Materials Building Blocks: network metamaterials for scalable, ultra-resistant structural colors; optical metasurfaces based on defect-engineered phase transition materials.

This work has resulted in four *Science* papers, *two Science Advances,* two *Nature Nanotechnology*, one *Nature Photonics*, one *Nature Communications*; one *Nature Light: Science and Applications,* one *PNAS* and many other leading journals: *Nano Letters, Advanced*

Materials, Physical Review Letters, Optica, Applied Physics Letters, APL Photonics, Optics Express.

Metasurface Platforms

Meta-Lenses at Visible Wavelengths: Diffraction-limited Focusing and Sub-wavelength Resolution Imaging

Major advances were made in metasurface lenses with the first report of high performance visible high numerical aperture metalenses. The enabling factor is a novel atomic layer deposition process of Titanium Oxide which creates low loss, negligible roughness, and high-aspect-ratio metasurfaces (Fig. 29).

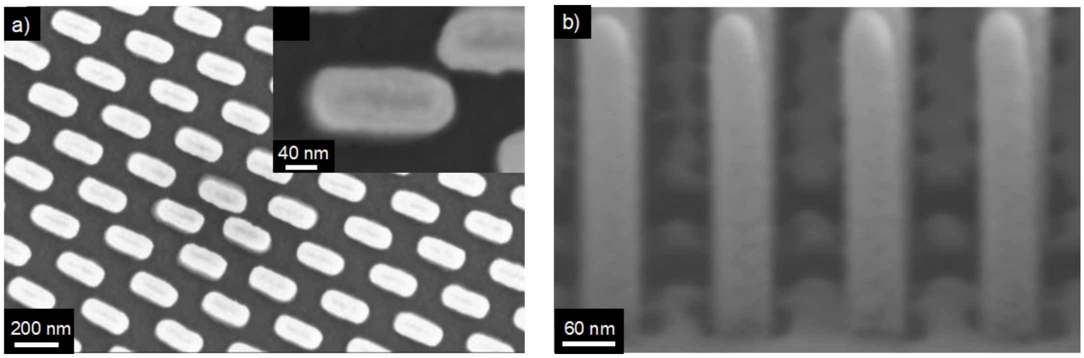

Fig. 29 Metasurfaces realized by Atomic Layer Deposition of TiO2 nanostructures a) SEM image showing arrayed pillars of 60 x 170 nm dimensions. Inset shows spacing of 10nm between individual pillars. b) Cross section SEM showing anisotropy of the fabricated nanopillars

Sub-wavelength resolution imaging requires high numerical aperture (NA) lenses, which are bulky and expensive. Metasurfaces allow the miniaturization of conventional refractive optics into planar structures. We showed that high-aspect-ratio TiO_2 metasurfaces can be fabricated and designed as meta-lenses with NA = 0.8 (Fig. 30) Diffraction-limited focusing was demonstrated at wavelengths of 405 nm, 532 nm, and 660 nm with corresponding efficiencies of 86%, 73%, and 66% (Fig. 31). The meta-lenses can resolve nanoscale features separated by sub-wavelength distances and provide magnification as high as 170× with image qualities comparable to a state-of-the-art commercial objective. Our results firmly establish that meta-lenses can have widespread applications in microscopy, imaging and spectroscopy.

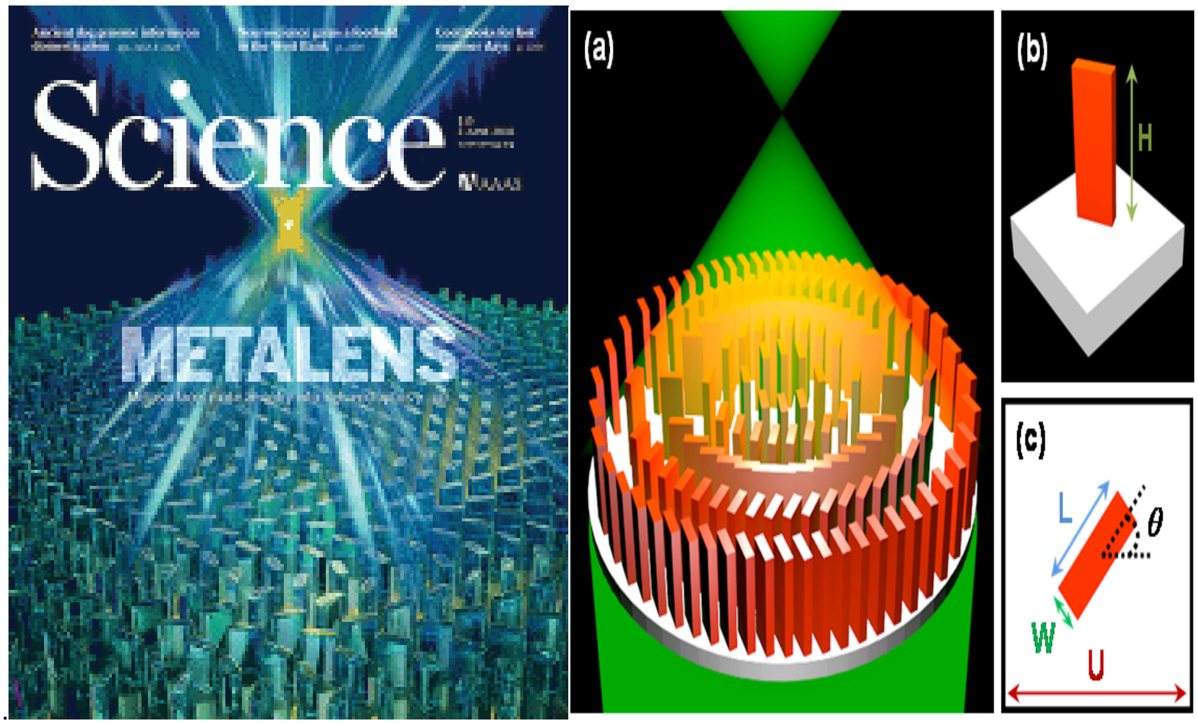

Fig. 30. (a) Transmissive metalens consisting of an array of TiO_2 nanofins on a glass substrate. (b) Side-view of the building block of the metalens: a single nanofin, showing its height. (c) Top-view of the nanofin with width W, length L, angle θ and the unit cell lattice constant U. Optimized parameters for the design wavelength of 405 nm (532 nm; 660 nm) are H=600 nm, W=40 nm, L=150 nm and U=200 nm (H=600 nm, W=95 nm, L=250 nm and U=325 nm; H=600 nm, W=85 nm, L=410 nm and U=430 nm)

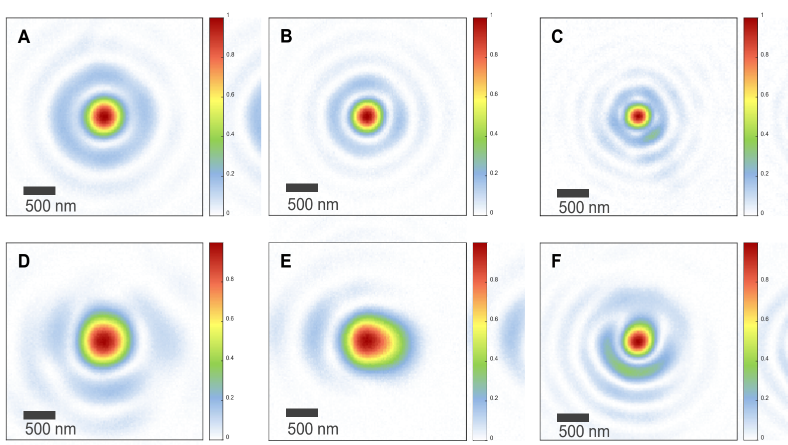

Fig. 31. Diffraction-limited focal spots of three meta-lenses and comparison with a commercial state-of-the-art objective**.** (**A** to **C**) Measured focal spot intensity profile of the meta-lens with NA=0.8 designed at (**A**) *λ_d=660 nm,* (**B**) *λ_d=532 nm,* and (**C**) *λ_d=405 nm*. (**D** to **F**) Measured focal spot intensity profiles of the objective (100× Nikon CFI 60, NA = 0.8) at wavelengths of (**D**) 660 nm, (**E**) 532 nm, and (**F**) 405 nm.

Broadband achromatic metalenses covering the visible spectrum

To achieve achromatic focusing across a significant bandwidth, objectives so far have required multiple lenses made of different glasses. The Capasso group has reported the first single achromatic lens. Made of suitably designed metasurfaces it focuses light of all wavelengths from the blue to the red with the same focal length in a diffraction limited spot. The metalens is designed to provide spatially dependent group delays and group delay dispersions such that outgoing wave packets at all wavelengths (white lines) from different locations are identical and arrive simultaneously at the focus (Fig. 32). The metalenses focus circularly polarized light.

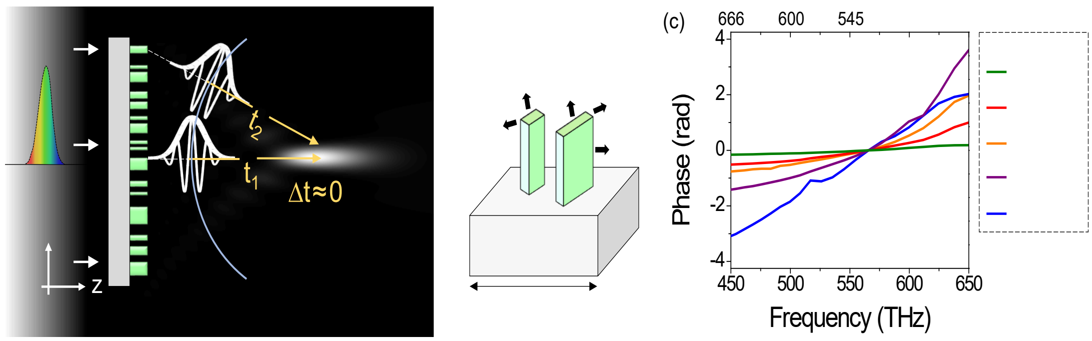

Fig. 32. (a) Schematic of an achromatic metalens. The metalens is designed to provide spatially dependent group delays and group delay dispersions such that outgoing wavepackets (white lines) from different locations are identical and arrive simultaneously at the focus. (b) Schematic diagram of a constituent element comprised of a pair of coupled TiO2 nano-pillars (c) Phase spectra for different elements. These spectra were obtained by the electric field of right-handed polarization in left circularly polarized incidence. Group delays and group delay dispersion are labelled in fs and fs squared units.

They also demonstrated diffraction limited metalenses with focal length displaying different typed of chromatic aberration. The focal length can be parameterized as $F(\omega) = k\omega^n$, where k and n are constant. By substituting different n values, the target phase and dispersion can be obtained and subsequently imparted by different TiO2 elements. Figure 33 a shows measured point spread functions of metalenses with n = 0, 1 and 2. The n = 1 case shows a chromatic metalens with focal length shift similar to Fresnel lenses. We can further increase the focal length shift as shown in the case of n = 2.

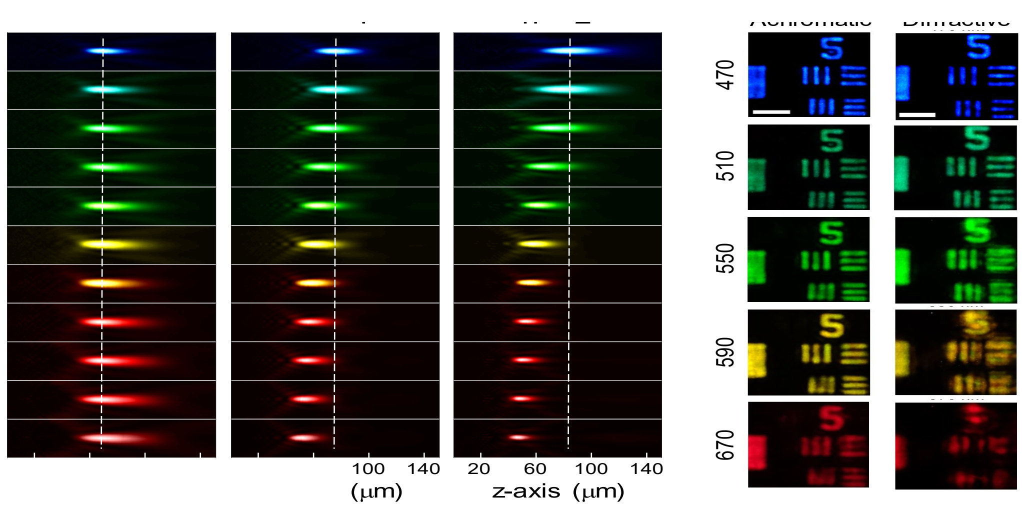

Fig. 33. Applications of dispersion-engineered metalenses. (a) Measured intensity distributions in linear scale (shown in false colors corresponding to their respective wavelengths) in the x–z plane. The wavelengths are labeled on the left. These metalenses have a numerical aperture of 0.2 at λ = 530 nm, and a diameter of 25μm. (b) Images of 1951 United States Air Force resolution target formed by the achromatic (first column) and diffractive (second column) metalenses. Scale bar: 100 μm. The numerical aperture and diameter are 0.02 and 220 μm, respectively.

More recently the Capasso group has demonstrated polarization insensitive metalenses across the visible, including white light focusing with efficiencies ~ 35% significantly larger than the above metalenses, by using anisotropic nanofins. Compared to isotropic nano-pillars, the nanofin structures provides more geometric parameters to tailor dispersion.

The Capasso group achromatic metalens work was discussed in the December Issue of Scientific American, which listed metalenses and flat optics in general as one of the top ten emerging technologies of 2019 https://www.scientificamerican.com/article/top-10-emerging-technologies-of-2019/ .

Broadband achromatic metasurface corrected refractive lens

Metasurfaces consist of sub-wavelength spaced nanostructures. By tuning the geometric parameters of each constituent nanostructure, the dispersion of the metasurface can be tailored pixel by pixel with sub-wavelength resolution to control the group delay and group delay dispersion of each 600-nm-tall TiO2 nanofins and thus compensate chromatic aberrations. (Fig.34 a, b). The hybrid lens was subsequently used to image a standard resolution target under incoherent broadband illumination from a lamp. The standard USAF resolution target was brought to focus at a wavelength λ = 460 nm and the distance between the target and the hybrid lens was kept constant for all other wavelengths. Thus, metasurface aberration correctors can work in tandem with traditional refractive optical components leading to major improvement in performance with reduced design complexity and footprint.

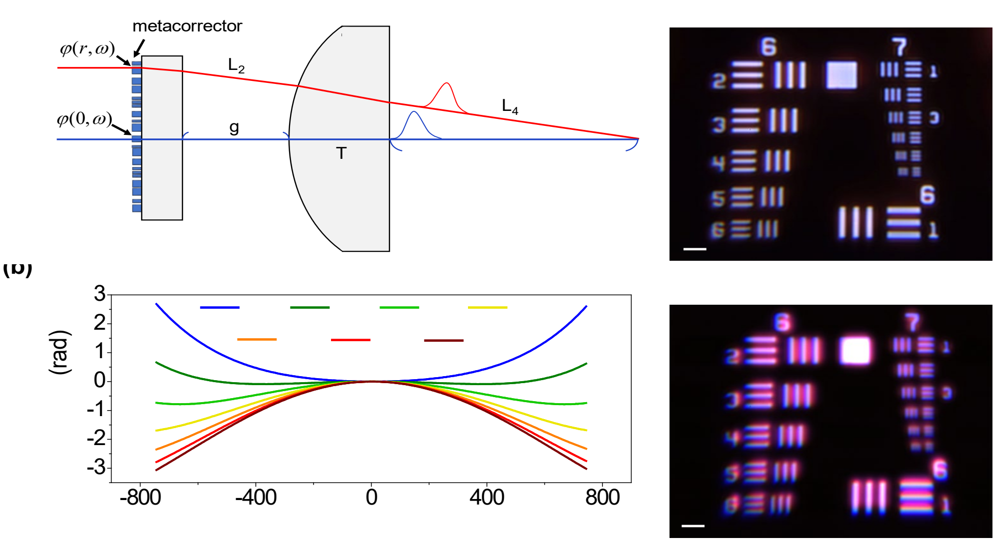

Fig. 34: Achromatic hybrid metasurface-refractive lens. The metacorrector has a diameter of 1.5 mm and the hybrid lens has a numerical aperture of 0.075. (a) Schematic of a hybrid lens consisting of a metacorrector and a spherical lens to illustrate wavepacket tracing. The refractive lens is a plano-convex spherical lens (LA4249, Thorlabs Inc.). (b) Phase profiles of the metacorrector for different incident wavelengths. The metacorrector has a wavelength-dependent phase profile to correct both spherical and chromatic aberrations. At blue wavelengths, because the focal length of the refractive lens becomes shorter, the metacorrector 's phase profile behaves like a diverging lens to increase the focal length so that they can be focused at the same position as green wavelengths, and vice versa at red wavelengths. (c) The image obtained without the metacorrector shows significant chromatic aberration, resulting in a blurred image.

Large area metalenses (in collaboration with the group of David Clarke, Harvard University)
Using a scalable metasurface layout compression algorithm that exponentially reduces design file sizes (by 3 orders of magnitude for a centimeter diameter lens) and stepper photolithography, we show the design and fabrication of metasurface lenses (metalenses) with extremely large areas, up to centimeters in diameter and beyond. Using a single two-centimeter diameter near-infrared metalens less than a micron thick fabricated in this way, high-quality imaging and diffraction-limited focusing was demonstrated. This result points to the possibility of unifying two industries: semiconductor manufacturing and lens-making.

Adaptive metalenses (in collaboration with the group of David Clarke, Harvard University)

The Capasso group demonstrated electrically tunable large-area metalenses, made of a-Si (focusing diffraction limited light at telecom wavelengths) controlled by artificial muscles (i.e. dielectric elastomer technology) capable of simultaneously performing focal length tuning (>100%) as well as on-the-fly astigmatism and image shift corrections, which until now were only possible in electron optics. These results demonstrate the possibility of future optical microscopes that fully operate electronically, as well as compact optical systems that use the principles of adaptive optics to correct many orders of aberrations simultaneously.

MEMS based dynamic metalenses (in collaboration with the group of Daniel Lopez, Argonne National Laboratory)

A monolithic Micro-Electro-Mechanical System (MEMS) integrated with a metasurface-based flat lens, consisting of Au dots on SiO_2 with an Au back plane, which focuses light in the mid-infrared spectrum was demonstrated. A two-dimensional scanning MEMS platform controls the angle of the lens along two orthogonal axes by $\pm 9^{\circ}$, thus enabling dynamic beam steering. This advance should enable a new class of flat optical devices with active control provided by the combination of metasurfaces and MEMS for a wide range of applications, such as miniaturized MEMS-based microscope systems, LIDAR scanners, and projection systems.

Miniature high-resolution spectrometers

The spectral resolution and range of conventional spectrometers are typically limited by optical aberrations of their focusing elements, mainly due to chromatically induced astigmatism and an intrinsically curved focal plane. Traditional approaches to overcome this challenge require additional optical components which introduce significant bulk and design complexity to the system and prevent easy integration with portable devices. Here a single planar off-axis focusing metalens consisting of subwavelength TiO_2 nanofins whose focal spots lie along a plane and undergo minimal focal spot broadening for almost 200 nm across the visible spectrum was demonstrated. This enabled a miniature aberration-corrected spectrometer with nanometer spectral resolution, while having a beam propagation distance of only 4 cm to the camera plane. This is achieved by dispersion engineering: tailoring the phase, group delay (GD) and GD dispersion of the metalens.

Nano-optic endoscope for high resolution medical imaging
(Collaboration with Prof. Melissa J. Suter group at Massachusetts General Hospital, Boston)

Endoscopic optical imaging techniques and endoscopic optical coherence tomography (OCT) using fiber optic catheters are emerging as promising tools for detection, diagnosis, and monitoring of disease in luminal organs. OCT endoscopes traditionally use either a graded-index (GRIN) lens or a ball lens to focus the light into the tissue. Constraints in the refractive index profile of GRIN lenses and shape of ball lenses result in spherical aberrations that impede high resolution tissue imaging. A metalens was integrated into the design of an endoscopic OCT catheter (termed nano-optic endoscope) to address these difficulties (Figure 35).

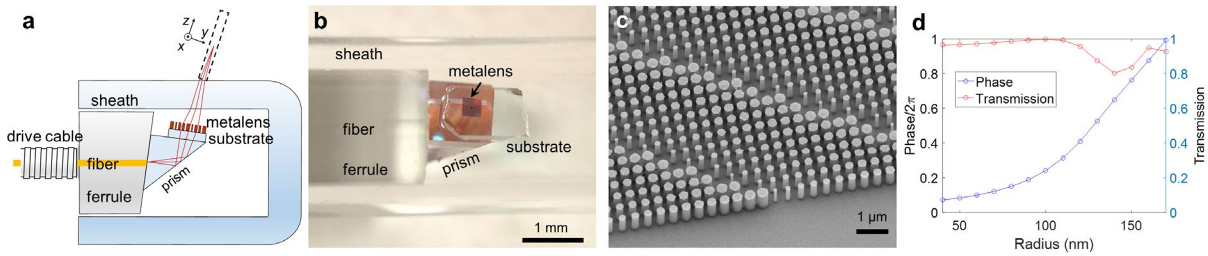

Fig. 35 a, Nano-optic endoscope schematic. b, Fabricated nano-optic endoscope. c, Metalens SEM images. d, Nanopillars phase/transmission.

The metalens ability to modify the phase at sub-wavelength level allows the nano-optic endoscope to achieve diffraction-limited imaging free of spherical aberrations and astigmatism (Figure 35). Remarkably, the tailored chromatic dispersion of the metalens allows maintaining high-resolution OCT imaging of in vivo and ex-vivo human and animal lung tissue significantly beyond the Rayleigh range of the incident light, thus enabling high-resolution imaging at an extended depth-of-focus with no requirements for additional acquisition/processing time or complex arrangements of optical elements. Glandular features, the hallmark of adenocarcinoma, were detected for the first time using this technique

Metasurface polarimeter (with Kristjan Leosson, University of Iceland, Reykjavík)
The need for complex optical systems and special materials have so far prevented polarization measurements from realizing their full scientific potential and achieving widespread use in technology. The Capasso group demonstrated a nanotechnology-based method for non-destructive polarization measurements using a single ultra-compact optical element and simultaneous co-planar intensity measurements. The method is based on a highly polarization-dependent scattered field, which is here implemented using a metasurface consisting of a nano-antenna array. The device (Figure 36) provides a polarization state measurement accurately matching that of a state-of-the art commercial rotating waveplate polarimeter across the full Poincaré sphere, while offering far superior speed, stability and compactness.

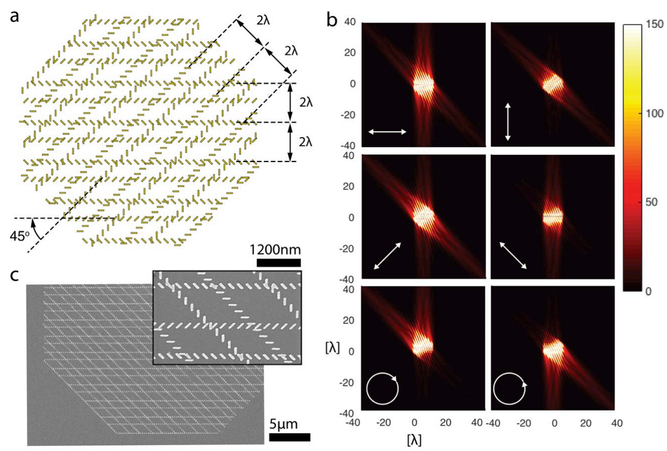

Fig. 36 Polarimetric antenna array. (a) The cross-section of the polarimeter is increased by patterning several pairs of antenna rows resulting in a patch as shown. (b) The calculated in-plane scattered field intensity of a polarimetric antenna array with 5 pairs of rows under illumination with different polarizations in the independent-dipole approximation (arbitrary units, color scale saturated in the central region). The spatial scale is in units of wavelength. The incident polarization states are shown as white arrows and correspond to the cardinal directions on the Poincaré sphere. Each polarization state results in a unique distribution of intensities over the four beams, implying that their measurement enables the deduction of a signal's state of polarization. (c) SEM micrographs of the fabricated structure designed for operation at telecommunication wavelengths. Inset: Close-up showing individual antennas of the array.

Compact full-Stokes polarization camera

Recently the Capasso group presented an extension of Fourier optics—matrix Fourier optics—for understanding of metasurfaces with space varying shape birefringence and attendant Jones matrix and applied it to the design and realization of metasurface gratings implementing arbitrary, parallel polarization analysis. Such gratings are designed to possess four diffraction orders that act as analyzers (i.e. follow Malus law) for four different polarization states corresponding to the vertices of tetrahedron on the Poincare' sphere (Fig. 37, first panel from right). As a result, when illuminated by a weakly focusing lens, they project four images on the sensor plane, each analyzed by one of the designed diffraction orders (Fig. 38, bottom). The four images are then overlapped and co-registered yielding for each image pixel the corresponding Stokes vector i.e. the polarization state of the light incident from the scene. In this way important quantities such as the azimuth of the polarization and the degree of polarization (Fig. 38), and the S_3 Stokes parameter, which provides information on the birefringence of the object can be imaged, providing depth information and details normally lost in conventional images based on brightness and color alone. This single-shot polarization camera requires no moving parts, specially patterned pixels, or conventional polarization optics and may enable the widespread adoption of polarization imaging in machine vision, remote sensing, and other areas.

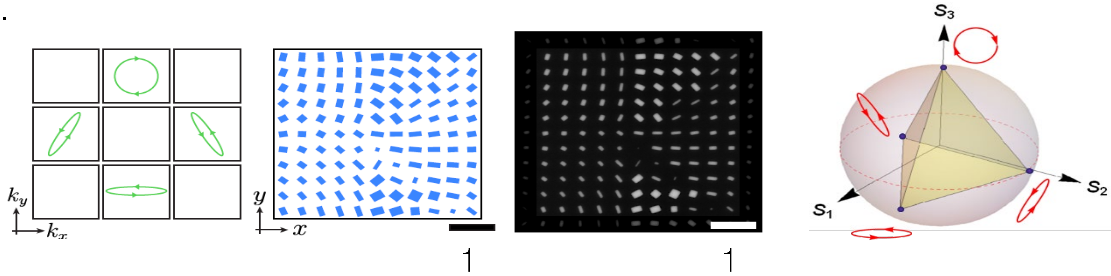

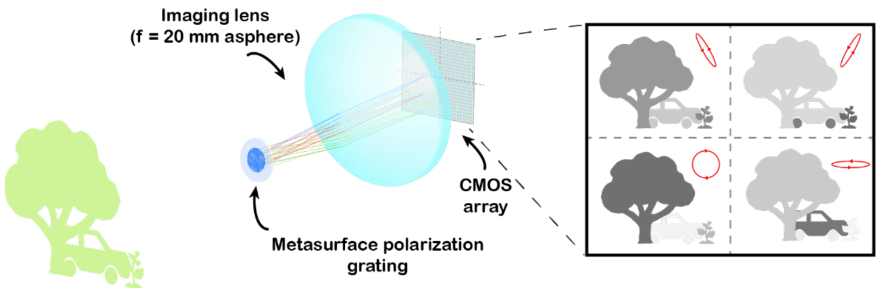

Fig. 37 A 2D grating unit cell is designed to analyze four polarization states corresponding to a tetrahedron inscribed in the Poincare´ sphere. On the left is a map of the diffraction orders and the polarization ellipses they analyze in *k*-space. The designed 11 × 11 element grating unit cell containing TiO_2 rectangular pillars implementing this at λ = 532 nm is shown in design (middle) and as-fabricated (SEM, right). The matrix meta-grating is integrated with an aspheric lens to image the scene's four diffraction orders onto four quadrants of a CMOS imaging sensor.

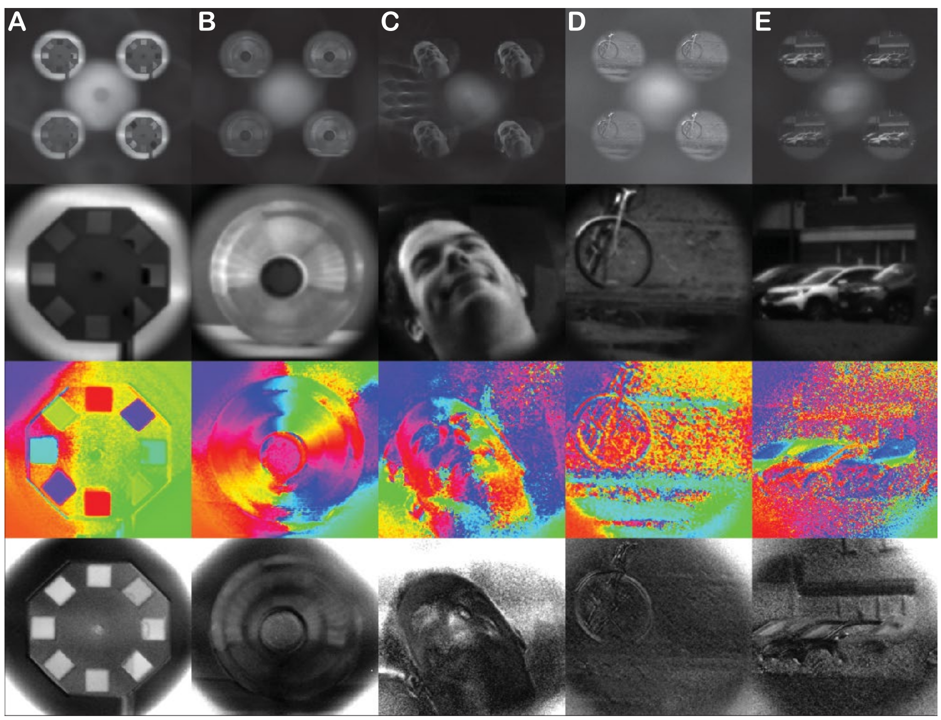

Fig. 38 Full-Stokes polarization imagery. Indoor (A-C) and outdoor (D, E) photography with the camera depicted in Fig. 3. In each case, the raw unprocessed exposure, S_0 (the traditional monochrome intensity image), the azimuth of the polarization ellipse (in degrees) and the degree-of-polarization (DOP) are shown. Indoor images were acquired at frame rates on the order of 100 ms, outdoor 10 ms. In both cases polarization imagery can be acquired at video framerate. The bright disk in the center of each raw exposure is zero-order light that does not interact with the grating and thus forms a defocused image of the scene. All images are at a single color (green, λ ~ 532 nm).

Metalens based depth sensing camera (in collaboration with Todd Zickler group, Harvard)

Jumping spiders (Salticidae) rely on accurate depth perception for predation and navigation. They accomplish depth perception, despite their tiny brains, by using specialized optics. Each principal eye includes a multi-tiered retina that simultaneously receives multiple images with different amounts of defocus, and from these images, distance is decoded with relatively little computation. We introduced a compact depth sensor that is inspired by the jumping spider. It combines novel metalens optics, which modifies the phase of incident light at a subwavelength scale, with efficient computations to measure depth from image defocus. Instead of using a multi-tiered retina to transduce multiple simultaneous images, the sensor uses a metalens to split the light that passes through an aperture, and to simultaneously form two differently-defocused images at distinct regions of a single planar photosensor. We demonstrate a system that uses a 3mm-diameter metalens to measure depth over a 10 cm distance range using fewer than 700 floating point operations per output pixel. This combination of nano-photonics and efficient computation brings artificial depth sensing closer to being feasible on millimeter-scale, micro-Watts platforms such as micro-robots and mobile sensor networks.

Physics of Metasurfaces

Metasurfaces for arbitrary spin-orbital angular momentum converters

Recently, Capasso and his group demonstrated the design of an optical element that provides an arbitrary mapping from spin angular momentum (SAM) to optical angular momentum (OAM); going well beyond the limitations of conventional SAM-to-OAM converters also known as q-plates. They implemented this design using a metasurface because of their ability to control both polarization and phase. To experimentally verify the design, they fabricated devices that map from SAM to OAM for two cases. First, they showed that one can transfer two input circularly polarized states to two unique values of OAM, a freedom not afforded by any previous device. They examined the full set of output states of the device and showed that this technique provides a way to produce a phased and weighted superposition of Total Angular Momentum (TAM) states of light. They also demonstrated the ability to transfer arbitrary and orthogonal elliptical polarizations to two unique values of OAM, which is the most general form of spin-to-orbit conversion (Fig. 39). Because of its ability to map SAM to two arbitrary output TAM, this device is referred to as a J-plate. These devices allow one to create superpositions of total angular momentum states of light with independently controlled phases and amplitudes. These results suggest a deep connection between optical spin and orbital angular momentum and may find applications in quantum and classical information.

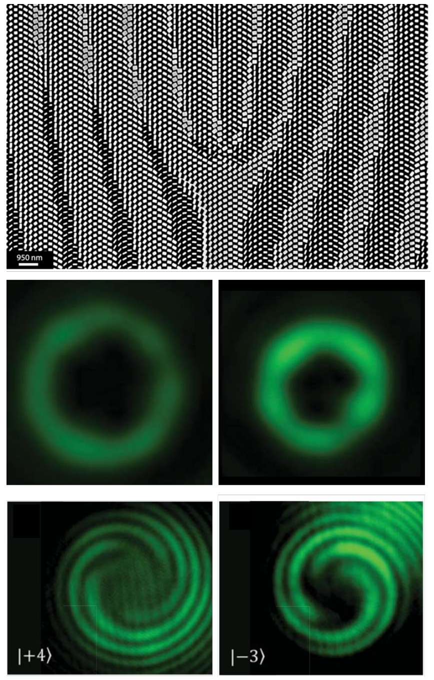

Fig. 39 (top) SEM micrograph of a TiO2 metasurface that allows transforming any two orthogonal polarization states into two independent values of orbital angular momentum. (bottom) Vortex beams of orbital angular momentum *l* = 4 and *l* = - 3 produced by means of a J-plate. The spiral patterns result from the interference between the vortex beam and the Gaussian beam incident on the metasurface

Metamaterials building blocks

Scalable, ultra-resistant structural colors based on network metamaterials (in Collaboration with Prof. Ralph Spolenak Group, ETH, Zurich)
An efficient approach to realize robust colors with a scalable fabrication technique is still lacking, hampering the realization of practical applications with this platform. They developed a new approach based on large-scale network metamaterials that combine subwavelength structures at the nanoscale with lossless, ultra-thin dielectric coatings to generate saturated structural colors that cover a wide portion of the spectrum. Ellipsometry measurements support the efficient observation of these colors, even at angles of 70 degrees. The network-like architecture of these nanomaterials allows for high mechanical resistance, which is quantified in a series of nano-scratch tests. With such remarkable properties, these metastructures represent a robust design technology for real-world, large-scale commercial applications.

(a) **(b)** **(c)**

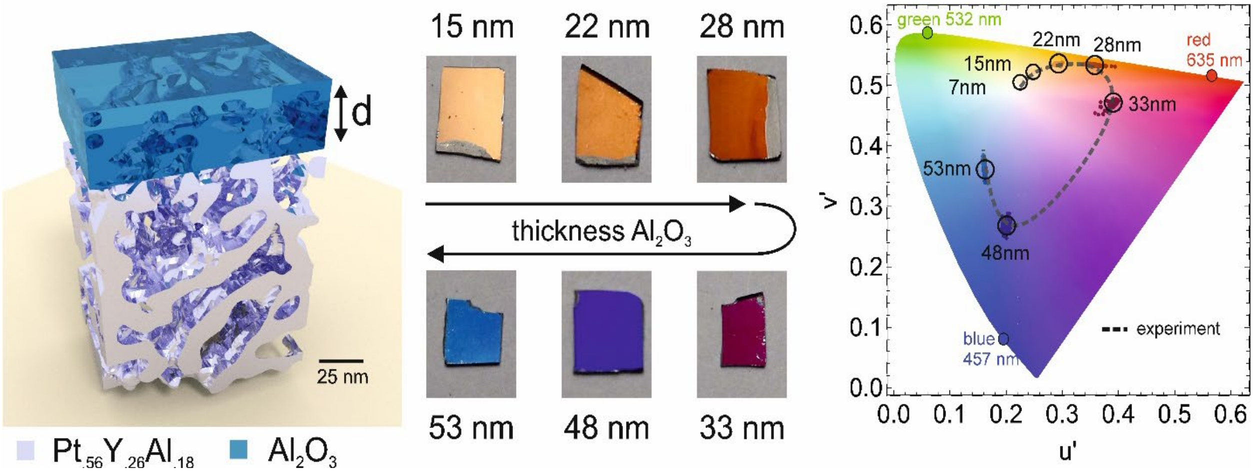

Fig. 40. Observation of structural colors in random metallic networks with subwavelength dielectric coatings. (a) Schematic illustration of an alumina coated PtYAl nanomaterial, based on a 3D reconstruction of a de-alloyed PtYAl thin film obtained via FIB assisted thin film tomography. (b) Photographs of deposited, de-alloyed, and alumina coated PtYAl metamaterial networks, illustrating the formation of vibrant colors and the continuous color change with increasing coating thickness. Each image is 2 × 2 mm^2. (c) Experimental and FDTD simulated structural color reported in a standard CIE 1931 (*x, y*) space, depicting the chromaticity visible to the average person. The RGB color space is marked by the triangle area. The chromaticity is calculated from reflectance spectra obtained either experimentally (circles markers) or by FDTD simulations (dashed line).

De-alloying was used to assemble a nanoscale metallic network with controllable features. This method utilizes the selective dissolution of the less noble constituent of an alloy during wet etching. In our experiments, 300 nm thick $Pt_{.14}Y_{.06}Al_{.80}$ thin films were deposited on an amorphous Si_3N_4/Si substrate. After etching of the less noble Al the remaining metal reorganizes into a network with an open porosity (Fig. 40a). The network can be altered by changing the etching time, the etchant concentration or the initial composition of the thin film. The nanomaterial is coated with an ultra-thin layer of Al_2O_3 using ALD (Fig. 40a). The coating thickness is increased stepwise in a range from 7 to 53 nm. A three-dimensional image of the network metamaterial, experimentally obtained using FIB thin film tomography, is displayed in Fig. 40a. The experiments unveiled a very interesting mechanism of structural coloration from the nanowire network, as shown in Fig. 40b. By changing the coating thickness, the formation of a multitude of colors spanning from yellow, orange, and red to, finally, blue was observed. Conversely, when the same coatings were deposited on a dense PtYAl metal thin film, no color was produced. The colors observed in the metallic network were saturated. Modeling showed that these colors are the result of the resonant coupling of light with surface plasmons that are localized in nanoscale epsilon near zero regions formed in the metallic network. Without the dielectric these nanoscale regions act as efficient broadband trapping regions; the resulting reflectivity is weakly dependent of wavelength as in the experiments. When the subwavelength thick alumina coating is added the reflectance, spectrum develops a deep wavelength minimum, which shifts linearly with thickness, in agreement with experiments, leading to a new form of structured color.

Marko Loncar Group

During the five year program the group explored novel metasurface platforms and their intriguing physics leading to several important breakthroughs: (a) the first demonstration of all-diamond metasurfaces with ultrahigh reflectivity and ultrahigh laser power handling capability; (b) the discovery by topological optimization of metasurfaces with functionalities such as designer exceptional points and new aberration corrected metalenses; (c) Dirac cone and zero index metasurfaces as new tool for photonic band engineering, including zero-index metamaterials based on diamond, leading to the demonstration of devices that feature Dirac cone and exhibit zero-effective refractive index; (d) nonlinear metasurfaces such as phase-matching-free second harmonic generation in a $LiNbO3$ waveguide with gradient metasurfaces; (e) quantum metasurfaces with Purcell enhanced emission from embedded NV centers.

Highly-Reflective All-Diamond Metasurfaces for High-Power Applications (in collaboration with Penn State University Applied Research Laboratory, Electro-Optics Center)

Many optical components use optical coatings to engineer their transmission or reflection properties. Examples include anti-reflection (AR) coatings, high-reflectivity mirrors based on Distributed Bragg Reflectors (DBR), dichroic beam splitters, and filters. However, the fact that

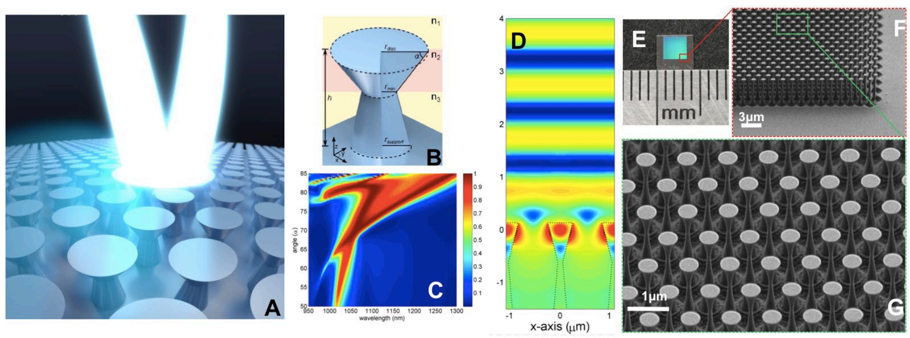

Fig. 41. Diamond metasurface mirror design, simulation and fabrication. **(A)** Illustration of the diamond metasurface mirror that consists of a hexagonal array of hourglass columns. **(B)** Schematic of the hourglass column, with all relevant dimensions indicaated: angle α, radii r_{disc}, r_{min}, $r_{support}$, and total height h. By precisely engineering each of these parameters, high reflectance can be achieved. **(C)** Reflection spectrum for the diamond mirror for different α. Red and blue colors indicate positions of maximum and minimum reflection respectively. **(D)** Optimizes structure features ~ 100 % reflectivity, without any wave-front distortion. **(E)** Optical image of the diamond metasurface mirror on a 4.2 mm x 4.2 mm diamond. Each division on the ruler is 1mm. **(F)** SEM image of the diamond mirror taken at 60º. **(G)** Zoomed in SEM image of hourglass features for the diamond mirror taken at 40º.

these devices use dissimilar materials in thin film form, results in significant damage when they are exposed to high optical powers. Imperfections in the coating layers or at the interfaces between the layers form sites where laser energy can be absorbed, leading to local melting or extreme thermal stress, thus significantly degrading the device performance. To overcome this, we have been developing novel highly-reflective dielectric mirror designs, that are fabricated from one material only. Our approach, illustrated in Figure 4a, is based on novel all-diamond high-reflectivity meta-surface (HiReMS) concept that consists of an array of hour-glass shaped pillars (Fig. 41B) engraved in the surface of diamond crystal. When structure parameters are properly designed these resonances can combine destructively with forward propagating beams resulting in perfect reflectivity of R = 100 % (Fig. 41C and D). To realize these complex 3-D structures (Fig. 41E-G) we used unconventional, yet scalable, angled-etching nanofabrication technique that we have recently developed. Our mirrors were characterized using both white light source and lasers, and reflectance of R = 98.9% was measured at 1.064 µm. Furthermore, R > 97 % was measured over 50 nm wide bandwidth, and experimental results were found to be in excellent agreement with theoretical predictions

High-power laser characterization of these high-reflectivity metasurfaces was performed. The laser source used for testing was a 1070 nm multimode fiber laser from IPG Photonics, capable of providing up to 10 kW of cw laser power. The laser intensity was incrementally increased from 500W to 10kW. At each power level the diamond mirror was irradiated for 30 seconds The red circle in each image indicated the area of interest that is being irradiated with the laser beam. A small fraction of the laser power leaks through the diamond mirror and is absorbed by the aluminum water cooled mount supporting the diamond. At the maximum intensity level, the diamond mirror had no indication of damage or change in surface morphology by optical or SEM inspection, proving to be far superior to existing high reflectivity high power mirrors and optics.

Owing to exceptional performance of our metasurface mirrors, the group is exploring opportunities to transfer this technology to a marketplace. Along these lines, two patents have been filed, and funds have been secured from DoD iCORP program that supports transition of technology from academia to market. Finally, collaborations with DoD labs (Navy) that is developing high-power laser weapons have been established.

Topology optimized metasurfaces *(in collaboration with Capasso Group)*

The group developed an advanced modeling approach based on topology optimization (TO) to enable automatic discovery of all-dielectric metasurfaces. It allows for inverse design of structures with predefined spectral, spatial and temporal response, and relies on a powerful computational technique which optimizes the shape and topology of a geometry over *every* pixel in the computational domain. Unlike traditional techniques, the method does not require any initial pre-conceived geometry to improve upon but rather develops the entire structure solely based on a specified performance objective. The group used this technique to realize zero-index metasurfaces with enhanced Purcell factor and complex spectral degeneracies including a third-order exceptional point (Fig. 42a). We have applied this method to discover efficient nonlinear metasurfaces with highly efficient second-harmonic generation (SHG) (Fig. 42b). A key distinction from previous formulation and designs that seek to maximize Purcell factors at individual frequencies is that this method aims to not only achieve frequency matching (across

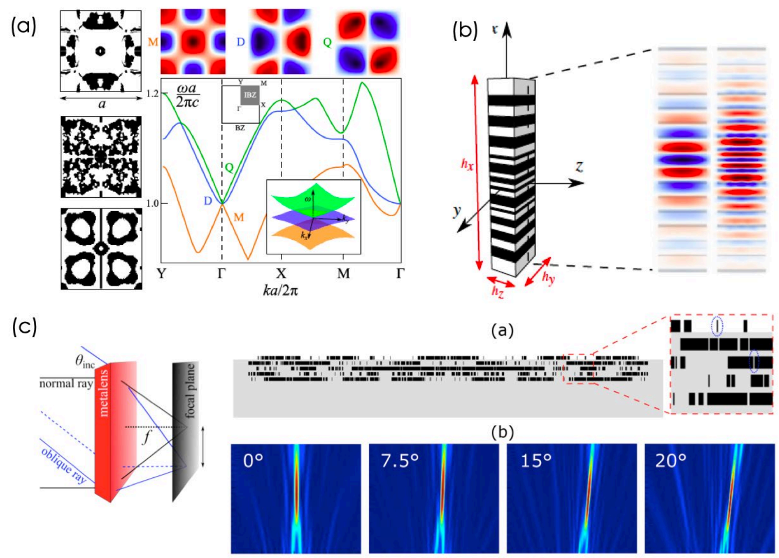

Fig. 42. **(a)** Discovered metamaterials that feature "exceptional" points. Structures host a Dirac cone with monopolar, dipolar and quadrupolar modes (right panel). **(b)** Schematic of a topology-optimized micropost cavity with alternating AlGaAs⁄Al2O3 layers. x–z cross section of the Ey components of fundamental and SHG modes. **(c)** Multilayered, aberration corrected, miniature 2D lens shown for incident angles of 0°; 7.5°; 15°; 20° The lens consists of five layers of silicon (black) in alumina matrix (gray). (Inset) A portion of the lens is magnified for easy visualization. FDTD analysis of the far-field profiles reveal focusing action for the four incident angles.

an entire octave) and large radiative lifetimes, but also optimizes the equally important nonlinear-coupling figure of merit β, involving a complicated spatial overlap-integral between modes. This method was applied to the problem of optimizing micropost and grating-slab cavities (one-dimensional multilayered structures) demonstrating that a variety of material platforms can support modes with the requisite frequencies, large quality factors and small modal volumes, leading to orders of magnitude enhancements in SHG efficiency compared to state-of-the-art photonic designs. Finally, the same approach was used to discover multilayered metasurfaces (MMS) which allow rich physical interactions within and between layers and thereby offer increased functionality. The key property of these MMSs is that the layers cannot be treated independently of each other but must be considered integrally in the design process. Such a consideration often leads to a greatly extended design space that cannot be handled by traditional design methods, which rely on precompiled libraries of intuitive geometrical elements. This approach led to the design of a compact aberration- corrected metalens, and a metalens that ensures diffraction-limited focusing under general oblique incidence (Fig. 42c).

Dirac cone and zero-index metasurfaces.

Zero-index metasurfaces (ZIMs) offer novel ways to manipulate the flow of light and are of interest for wide range of applications including optical cloaking, super-coupling, phase-mismatch-free nonlinear optics, and enhanced light emission of embedded quantum emitters (e.g. via inherently phase-matched super radiant effect). The group designed and fabricated on-chip integrated 2D metasurfaces with a refractive index of zero in the optical regime. The first structure consisted of silicon pillar arrays embedded in a polymer matrix and clad by gold. This ZIM arrangement features Dirac cone-like dispersion at the center of the Brillouin zone, resulting in an index that is isotropically near zero (Fig. 43) and can be impedance-matched to free space or standard optical waveguides. To characterize our ZIM, prisms made of this material were realized, and delivered light to it using integrated optical waveguides (Fig. 43d). In the experiments light refracts perpendicular to the facets of the prism as expected in the case of near zero effective index (Fig. 43e). By sweeping the wavelength of the excitation beam and performing the parameter retrieval, the group confirmed that refractive index is zero in telecom wavelength range (Fig. 43). To overcome losses associated with gold

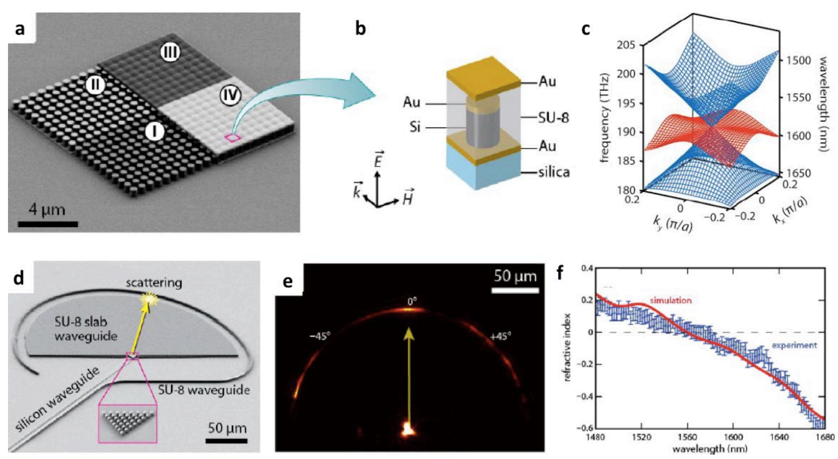

Fig. 43. a) SEM image of the metamaterial structure in four different fabrication stages: I. Silicon pillars on a silicon-on-insulator (SOI) substrate; II. Silicon pillars with bottom gold layer; III. Silicon pillars in SU-8 matrix with bottom gold layer; IV. Silicon pillars in SU-8 matrix with top and bottom gold layers (completed structure). **b)** 3D view of one unit-cell of the metamaterial. **c)** 3D dispersion surfaces in the vicinity of Γ point. The linear bands (blue) form a Dirac-like cone**. d)** SEM image of the fabricated device and corresponding **e)** near-infrared microscope image of the prism excited by light. 0 degree refraction can be observed, indicative of near-zero refractive index. **f)** Measured and simulated effective index of the zero-index metamaterial.

absorption, robust all-dielectric ZIM that supports Dirac cone dispersion over wide parameter space were demonstrated. This also overcomes major obstacle of conventional structures – sensitivity to fabrication imperfections. The structure, consisting of an array of Si pillars on silica substrate, is fabricated in silicon-on-insulator (SOI) platform and operates at telecom wavelengths. With proper choice of lattice constant a and pillar height h_{Si} , the PDC features the fabrication tolerance against pillar diameter $2r$ variation (Fig. 44), which is obtained by engineering the structural dependencies of the target modes. These designs were experimentally confirmed, also showing that PDC and zero-index operation can be obtained over wide wavelength range, much wider than in previous work.

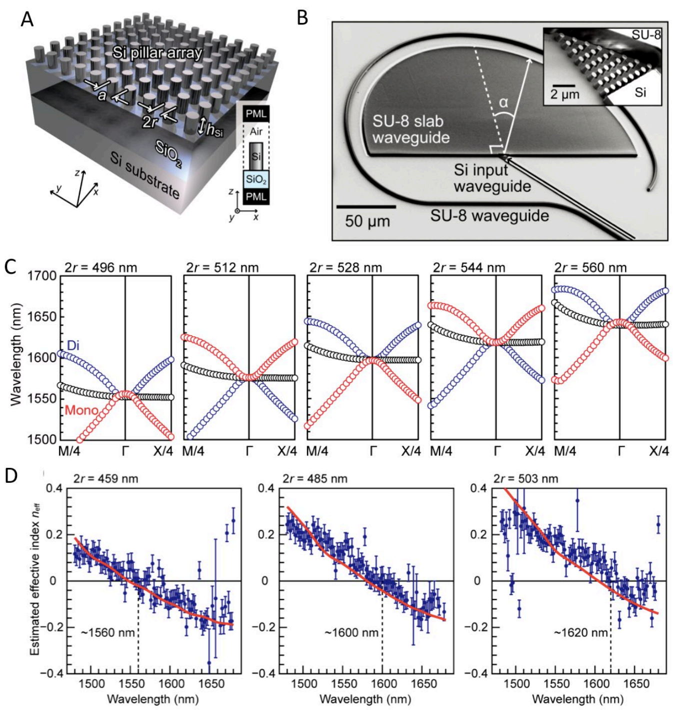

Fig. 44. Fabrication tolerant on-chip all-dielectric zero-index metamaterial**.** A) Schematic and B) SEM image of the device. C) Photonic band diagrams with five different diameters ($2r$) showing Dirac cone at different wavelengths. Blue, red and black dots indicate dipole, monopole, and "dark" longitudinal magnetic dipole modes, respectively. D) Measured effective index n_{eff} for metamaterials with three different pillar diameters (2r). Blue dots and red lines indicate the experimental and theoretical results, respectively.

The topology optimization technique was also used to discover the structures with Dirac cone. Focusing on geometries, realizable in simple isotropic dielectric materials, which exhibit dual-polarization Dirac cones photonic crystals of different symmetry types, such as four-fold and six-fold rotational symmetries, with Dirac cones at different points within the Brillouin zone were designed. This works opens avenues to new forms of photonic band-structure engineering and manipulating the propagation of light in periodic media, with possible applications to exotic optical phenomena such as effective zero-index media and topological photonics.

Nonlinear Metasurfaces

(in collaboration with Nanfang Yu (Columbia), and Marty Fejer (Stanford) groups)

The phase-matching condition is a key aspect in nonlinear wavelength conversion processes, which requires the momenta of the photons involved in the processes to be conserved. Conventionally, nonlinear phase matching is achieved using either birefringent or periodically poled

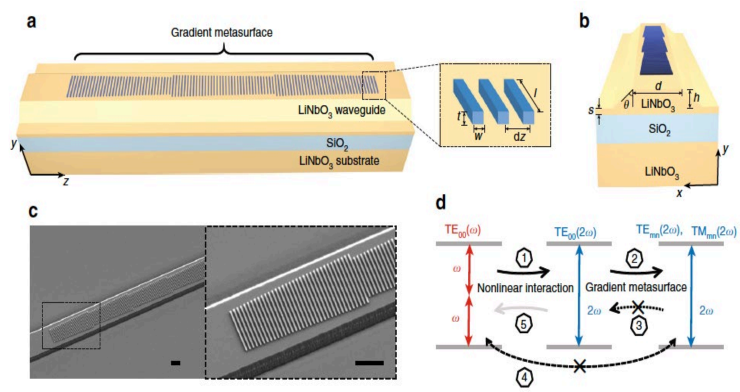

Fig. 45. a Schematic of an integrated nonlinear photonic device, where a gradient metasurface is used to achieve phase-matching-free second harmonic generation (SHG) in a LiNbO3 waveguide. **b** device cross-section, and **c** images of a fabricated devices. **d** Conceptual diagram of the proposed phase-matching-free SHG.

nonlinear crystals, which requires careful dispersion engineering and is usually narrowband. In recent years, metasurfaces consisting of densely packed arrays of optical antennas have been demonstrated to provide an effective optical momentum to bend light in arbitrary ways. Gradient metasurface structures consisting of phased array antennas can circumvent the phase-matching requirement in on-chip nonlinear wavelength conversion. The group demonstrated phase-matching-free second harmonic generation over many coherent lengths in thin film lithium niobate waveguides patterned with the gradient metasurfaces. Efficient second harmonic generation in the metasurface-based devices is observed over a wide range of pump wavelengths (λ = 1580–1650 nm).

Quasi-phase-matched interactions in waveguides with quadratic nonlinearities enable highly efficient nonlinear frequency conversion. To that end the group demonstrated the first generation of devices that combine the dispersion-engineering available in nanophotonic waveguides with quasi-phase matched nonlinear interactions available in periodically poled lithium niobate (PPLN). This combination enables quasi-static interactions of femtosecond pulses, reducing the pulse energy requirements by several orders of magnitude, from picojoules to femtojoules. Efficient quasi-phase-matched second harmonic generation with <100 fJ of pulse energy was observed. In the limit of strong phase-mismatch, spectral broadening of both harmonics with as little as 2-pJ of pulse energy was observed. These results lay a foundation for a new class of nonlinear devices, in which co-engineering of dispersion with quasi-phase matching enables efficient nonlinear optics at the femtojoule level.

Quantum Metasurfaces *(in collaboration with Eric Mazur group, Harvard)*

Solid-state quantum emitters, such as the silicon-vacancy (SiV) color centers in diamond, have recently emerged as the most promising quantum emitters in the solid state, of interest for applications in quantum science and technology. These applications benefit from higher photon emission rates, which in turn can be engineered through engineering the local density of photon states. To accomplish this, we used circular gold-diamond apertures to engineer the emission of SiV centers (Fig. 46a) Simulations show that for circular aperture of 110 nm diameter a Purcell enhancement ~15 can be achieved. In our experiments, lifetimes as short as 0.2 ns for SiV centers embedded inside apertures (Fig. 47b) were measured, which represents a ~9-fold reduction over a ~1.8 ns value typical for SiV^- in bulk diamond (Fig.47c).

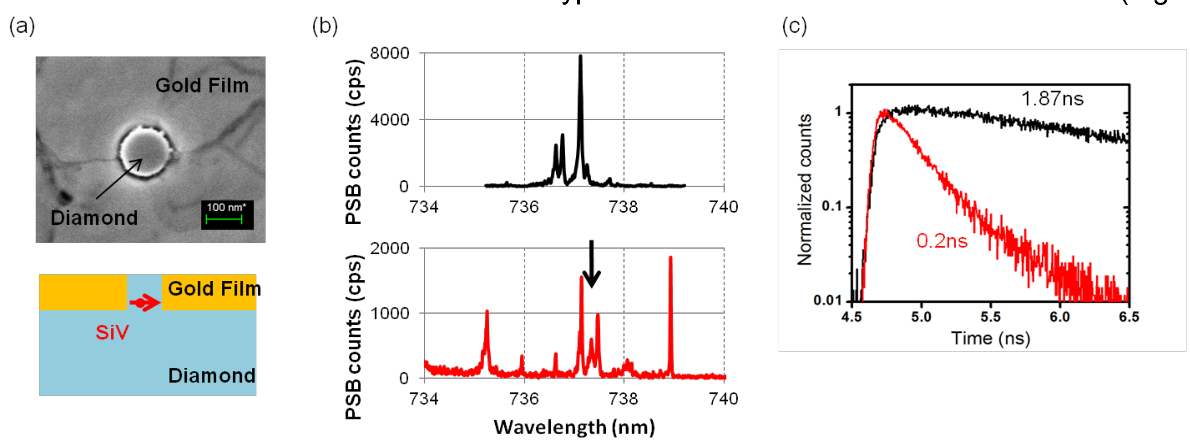

Fig. 46. Engineering the emission properties of SiV centers in diamond, using metallic apertures. **(a)** SEM image of the gold diamond aperture and its schematic side view. It is designed to have resonance around SiV emission wavelength at 737 nm. (**b)** (top) Resonant scanning of ensemble of SiVs in bulk diamond: four peaks, the signature of SiV, can be resolved; (bottom) Resonant scanning of a single aperture containing multiple SiVs: Each peak represents the specific transition of one of the SiVs. Due to different coupling rate, each transition has its own lifetime, and the one pointed with arrow has the shortest lifetime 0.2 ns. **c)** The maximum lifetime reduction that the aperture resonators produce is ~9.

Zero-index metamaterials based on diamond, leveraging on the group's expertise with diamond quantum photonics were explored, leading to the demonstration of devices that feature Dirac cone and exhibit zero-effective refractive index (Fig. 47). Current activities are focused on introducing color silicon-vacancy (SiV) color centers inside the structures, with the goal of observation of super-radiant emission rom an array of SiVs. The main challenge is overcoming inhomogeneous distribution of SiV color centers, due to variations in local strain environments of different SiVs. The group has developed techniques for strain tuning of quantum emitters in diamond, and these will be leveraged to address the inhomogeneous broadening issues.

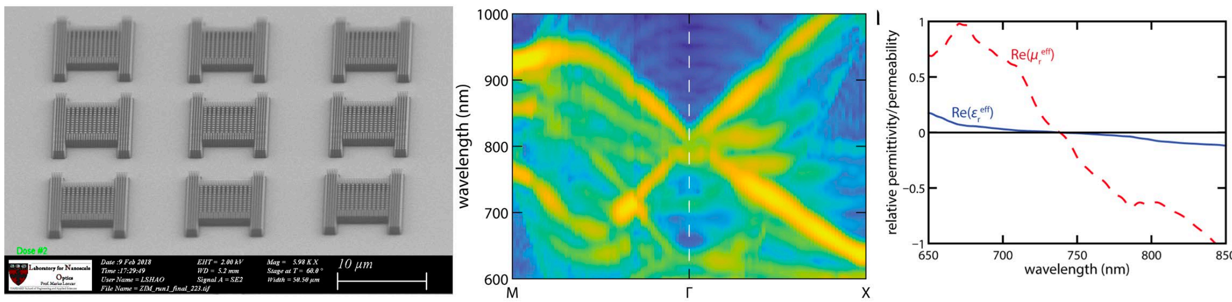

Fig. 47. Left: fabricated all-diamond near-zero refractive index metasurface. Middle: the dispersion of these structures features a Dirac cone, and (right) near-zero effective epsilon.

Nader Engheta Group

During the 5-year period of this MURI program, the group theoretically investigated several research programs on wave-matter interaction with metasurfaces. These include: (1) One-way photonic surface states with magnetized materials; (2) All-Passive Nonreciprocal Metasurfaces; (3) Dispersion Engineering using Metatronic Metasurfaces based on Filter Design; (4) Metasurfaces with Plasmonic Features without Negative Dielectrics; (5) ENZ-based and EMNZ-based Metasurfaces for Switching "Windows"; (6) Metatronic Analogue of the Wheatstone Bridge; (7) Metasurface Tunability via nonlinearity and via mechanical actuation; (8) Inverse-designed Metasurfaces as Anti-Reflection (AR) Coating for Rough Surfaces; (9) Metasurface Lenses with Broken Optical Axes; and (10) nonlinear photonic doping and nonlinear Salisbury metasurfaces.

All-Passive Nonreciprocal Metasurfaces

In this project, how nonlinearity combined with spatial asymmetry in wave propagation may provide nonreciprocity for photon flows was theoretically explored. As is well known, there are three ways one can break the time-reversal symmetry: (1) using biasing magnetic field in magneto-active materials; (2) temporal and spatio-temporal modulation of material parameters; and (3) nonlinearity merged with asymmetric wave propagation. In the study here, the group considered a nonlinear metasurface embedded in the proper position within a bi-layered structure formed by two dielectric slabs with unequal dielectric constants and unequal thicknesses. The broken symmetry in the properties of the two dielectric slabs provides the required asymmetry, leading to asymmetric field distribution within them, while the bilayer is still reciprocal. However, when this structure is combined with the nonlinearity in the metasurface, the entire structure may exhibit non-reciprocal behavior. In Fig. 48, as an example varactor element are studied, which are known to be nonlinear in the microwave regime. This is effectively a metatronic "diode".

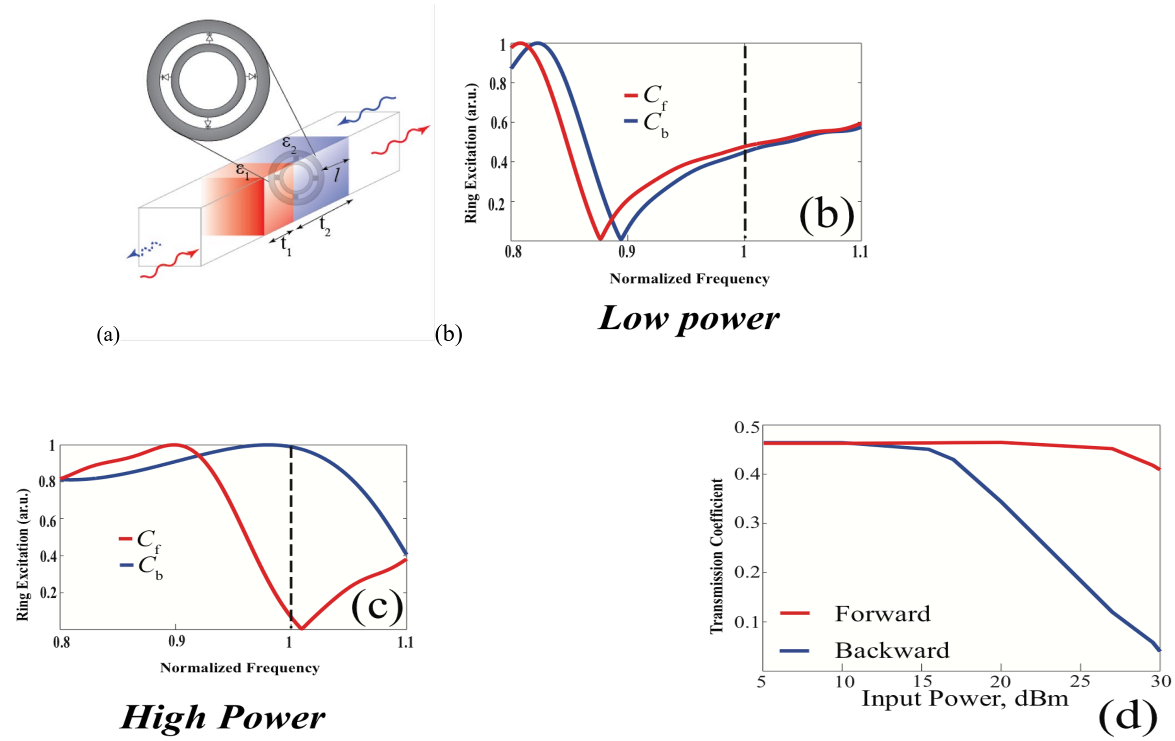

Fig. 48 Combining nonlinearity with asymmetric bilayered metasurface, to develop nonreciprocity when the incoming power is high enough: (a) geometry of the problem; (b) Simulation results for the response of the ring with varactors added, when the power is low; (c) similar to (b), but with higher power; (d) simulation result for the transmission coefficient of the metatronic metasurface "diode" for the forward and backward direction, in terms of incoming power.

Dispersion Engineering using Metatronic Metasurfaces based on Filter Design

In this project, we explored theoretically the synthesis of frequency dispersion of layered metasurfaces based on the design of multi-ordered optical filters using metatronic metasurface concepts. Utilizing the insertion loss method commonly employed in the design of electronic and microwave filters, in our theoretical study we showed how we could tailor optical dispersion by combining proper sets of metasurfaces. As examples of our technique, we have carried out the design of several low-pass, high-pass, band-pass and band-stop filters of different orders with a (maximally flat) Butterworth response by combining proper metasurfaces. We numerically demonstrate that such dispersion engineering can be achieved by combining metasurfaces made of one or two materials acting as metatronic optical lumped elements, and, hence, leading to simple, easy to apply, design rules. We have also validated our theoretical results based on this circuital approach using full-wave numerical simulations. We have also developed the metatronic analogue of the Wheatstone bridge. Our findings can have important applications in material response synthesis for customized light-matter interaction with important technological applications. Our results can be extended to other frequency dispersion synthesis, filter design procedure and/or functionality, thus opening exciting possibilities in the design of composite materials with on-demand dispersion and high-performance and compact optical filters using one or two materials. Figure 49 shows some of the numerical results of our study.

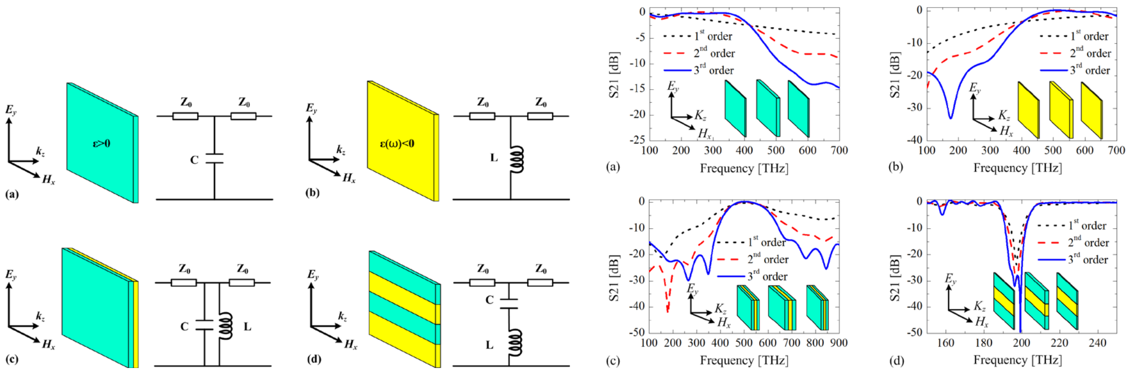

Fig. 49. Higher-order optical metatronic filters using metasurfaces made of positive- and negative-epsilon materials. (left panel): Single-order low-pass filter (green top left made of positive-epsilon thin layer), high-pass filter (yellow top right made of negative-epsilon thin later), band-pass filter (bottom left, made of two metasurfaces one from positive- and one from negative-epsilon materials), band-stop filter (bottom right, using a single metasurface formed by stripes of positive and negative epsilon materials). (Right panel) simulation results for the first-, second- and third-order optical metatronic low-pass (top left), high-pass (top right), band-pass (bottom left), and band-stop (bottom right) filters.

Inverse-Designed Metasurfaces as Anti-Reflection Coating for Rough Surfaces

It is well known that placing a quarter-wavelength anti-reflection (AR) coating on top of a flat interface between two media can reduce the reflection of a normally incident plane wave. However, this approach does not work for rough surfaces. Here we have theoretically explored how metasurfaces can be designed in order to achieve AR coating for rough surfaces. Using the inverse design based on optimization methods with the gradient descent techniques, we have been able to explore thin metasurfaces that would reduce the reflection significantly when located above a rough surface. Figure 50 a shows the geometry of the rough surface of silicon, and Fig. 50 b presents the optimized metasurface (for the perpendicular polarization) that can be formed by an inhomogeneous distribution of dielectric material (with relative permittivity of 6) and air. As can be seen from Figs. 50c-e, the reflection coefficient for the normally incidence plane wave can be reduced when the AR metasurface is placed in front of the rough surface.

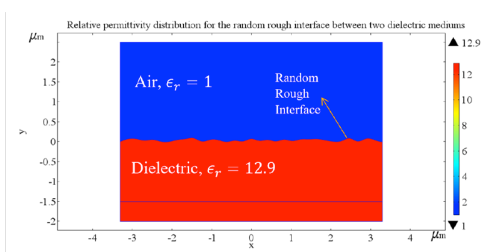

(a)

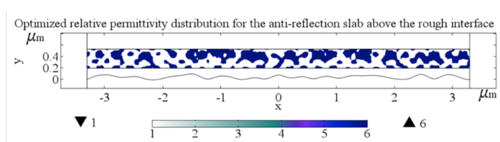

(b)

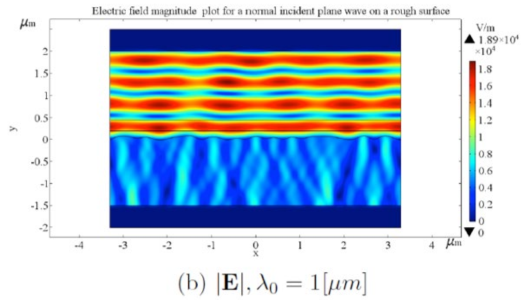

(c)

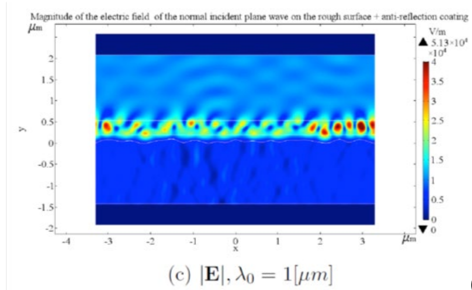

(d)

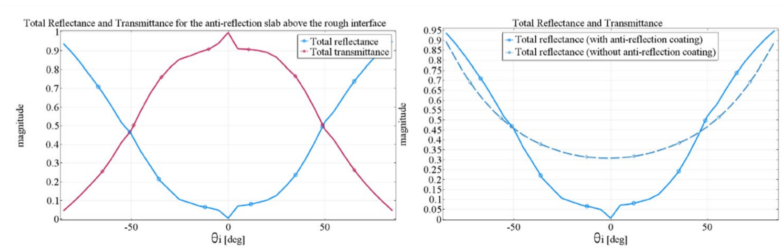

(e)

Fig. 50 Metasurfaces as AR coating for Rough Surfaces: (a) Geometry of the rough surface of a dielectric (e.g., silicon) region; (b) Inverse-designed metasurface. This metasurface can be formed as an inhomogeneous distribution of a dielectric material (with relative permittivity of 6) and air; (c) the magnitude of the total electric field with perpendicular polarization illuminating a rough surface only, and (d) for the AR metasurface above the rough surface. We can clearly see the reduction of the reflected wave in (d) when compared with (c); (e, right panel) the comparison between the reflectance of the case of rough surface only and that of the case of AR metasurface above the rough surface. We see that the reflectance is reduced for the incidence angle between around -50 degrees and +50 degrees. (e, left panel) shows the reflectance and transmittance for the AR metasurface above the rough surface.

ENZ-based and EMNZ-based Metasurfaces for Switching "Windows"

In this project, we conducted theoretical and numerical research on the light-matter interaction in the epsilon-near-zero (ENZ)-based and epsilon-and-mu-near-zero (EMNZ)-based metasurfaces, particularly for their properties as switching "windows". By properly adding a non-magnetic conventional dielectric rod with positive dielectric constant into non-magnetic ENZ metasurfaces (See Fig. 51 top left panel), the composite metasurfaces can interact with EM waves quite differently. Such composite metasurfaces may behave as a structure with effective permittivity near zero, while its effective permeability can exhibit a desired value even though none of the materials involved are magnetic. For example, one can have an ENZ metasurface that can act as perfect magnetic conducting (PMC) wall (even though none of the materials is magnetic) when the dielectric rod has a proper radius and/or dielectric material. In this case, the composite metasurface can have small transmission coefficient. Alternatively, by changing the radius and/or permittivity of the dielectric rod in the ENZ metasurface, the same composite ENZ metasurface can be structured such that the entire metasurface exhibits effective epsilon-and-mu-near-zero (EMNZ) property, in which case the transmission coefficient can be high. Figure 51 (top right panel) shows the result of our numerical simulation of the transmission coefficient of such composite ENZ metasurface. We note that at the $\omega = \omega p$, we get high transmission (i.e., the metasurface effectively behaves as epsilon-and-mu-near-zero (EMNZ)) and at a lower frequency ($\omega = 0.985\omega p$), we have the transmission coefficient small, where the metasurface may act as a magnetic wall (denoted as PMC "Perfect magnetic wall"). The bottom right and left panels in Fig. 51 shows the simulation results as the wave interacts with these ENZ-based metasurface. As we note, the left metasurface behaves as a PMC metasurface “closed window”, whereas the right metasurface acts as an EMNZ metasurface “open window”. In both cases, the ENZ metasurface is the same, but the dielectric rod behaves quite differently as these two different frequencies. Such ENZ-based metasurface may find useful applications in switchable windows.

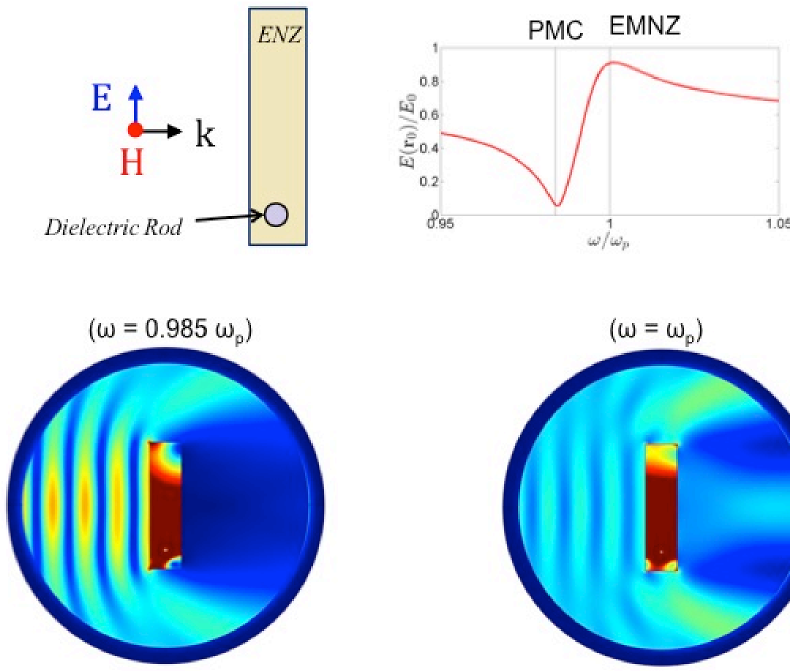

Fig. 51. Metasurface “window” based on the ENZ and EMNZ layers: (Top left panel): ENZ metasurface in which a single dielectric rod is embedded. Based on the choice of the radius and/or dielectric constant of the rod, the composite metasurface can have significantly different transmission properties. (Top right panel): Results of our numerical simulation for the transmission coefficient. At $\omega = \omega p$ the composite ENZ-based metasurface behaves as EMNZ metasurface “open window”, whereas at $\omega = 0.985\omega p$, the metasurface behaves as PMC metasurface “closed window”. Bottom panels show our simulation results for the field distributions for these two cases.

Metalenses with Broken Optical Axes

Conventional lenses possess optical axes that are normal to the plane of the lens. However, metasurfaces can be exploited to achieve lensing with broken optical axes. We theoretically investigated several classes of metasurface lenses with such broken axes. As an illustrative example, here we present the case of metasurfaces with vertical focal planes, i.e., the lens whose optical axis is rotated by 90 degrees. One of the interesting applications of such lenses would be in confocal microscopy. Such a metasurface may enable imaging of objects in the plane perpendicular to the lens plane, contrary to the conventional lens that images objects in the plane parallel with the lens. Figure 52a shows the sketch of our idea. We would like incident beams with different angles of incidence focus at focal points that are in the plane perpendicular to the lens plane. We have pursued 4 different approaches. Here we discuss only one of these 4 cases. Figure 52b shows the optimized distribution of dielectric material (with relative permittivity of 4) and air in such desired metasurface. Our numerical simulation shows the time snap shot (Fig. 52c) and the magnitude (Fig. 52d) of the electric field distribution for this "vertical-focal-plane lens". We can clearly see that for different incidence angles of incoming beams, for which the metasurface has been optimized using the inverse design, the focal point is moved vertically. However, the intermediate incidence angles may have some reflections. This issue can be addressed by one of our other approaches to design such lenses. Figure 52e illustrates the field distribution cut in the vertical plane, highlighting the width of the focal points. Such a metasurface lens can potentially be useful in confocal microscopy, since the vertical cut in a medium can be imaged in the image plane of the lens, therefore by rotating the lens in the azimuthal plane, one can image a volumetric region in the object domain.

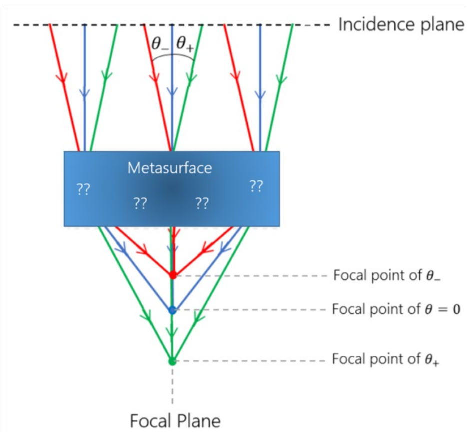

(a)

(b)

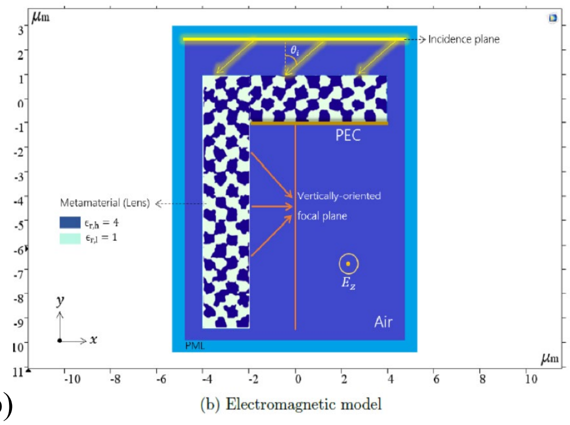

(c)

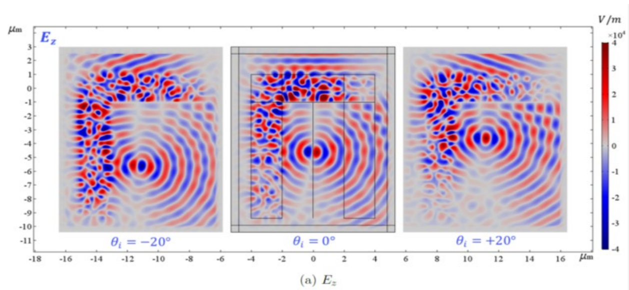

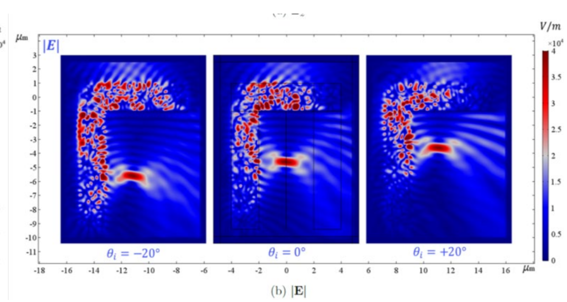

(d)

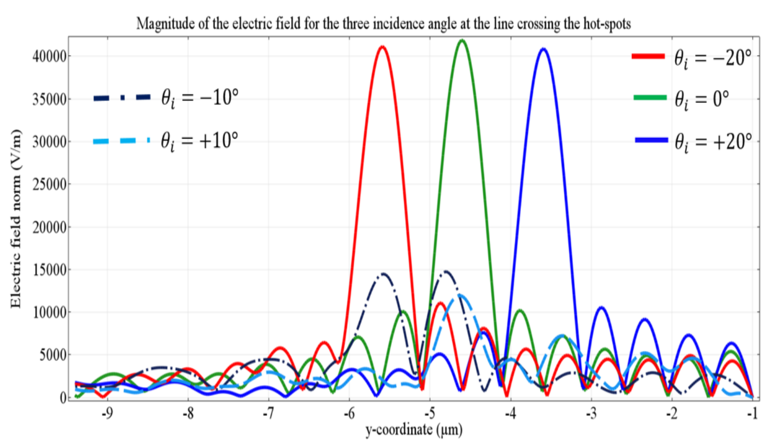

(e)

Fig. 52. Metasurface Lens with Broken Optical Axes: (a) Our idea of metasurface possessing vertical focal plane; (b) Our optimized metasurface, having inhomogeneous distributions of dielectric material (with relative permittivity of 4) and air, providing 90-degree bend of the optical axis; simulation results for (c) the time snap shot and (d) the magnitude of the total electric field distributions in this metasurface, for three different incidence angles (-20, 0 and +20 degrees), clearly showing how the focal point is moved along the vertical axis as the incidence angle changes. The intermediate angles (-10 and +10 degrees) have more reflection. This issue can be addressed by one of our other approaches; (e) magnitude of the electric field distributions in the vertical focal plane.

Metasurfaces with Plasmonic Features without Negative Dielectrics

Traditionally, plasmonic phenomena are exhibited in light-matter interaction involving materials whose real parts of permittivity functions attain negative values at operating wavelengths. However, it is also well known that such materials usually suffer from dissipative losses, thus limiting the performance of plasmon-based optical devices. In this project, we theoretically investigated an alternative methodology that mimics a variety of plasmonic phenomena by exploiting the structural dispersion of electromagnetic modes in bounded guided-wave structures filled with only materials with positive permittivity. This method for developing metasurfaces with plasmonic features without using negative dielectrics is more suitable for lower frequencies and allows designers to employ conventional dielectrics and highly conductive metals for which the loss is low at these frequencies, while achieving plasmonic features. In this project, we also introduced and developed the concept of **"**waveguide metatronics,**"** an advanced form of optical metatronics that uses structural dispersion in waveguides to obtain the materials and structures required for design of this class of circuitry and metasurfaces. Using numerical simulations, we explored the design of metatronic metasurface circuits using waveguides filled with materials with positive permittivity. This includes the design of all **"**lumped**"** circuit elements and their combination in a single metasurface. In doing so, we extended the concepts of optical metatronics to frequency ranges where there are no natural plasmonic materials available. This methodology can have interesting applications in design of metasurfaces with desired spatial and temporal dispersion. Figure 53 depicts these concepts and an example of our numerical result.

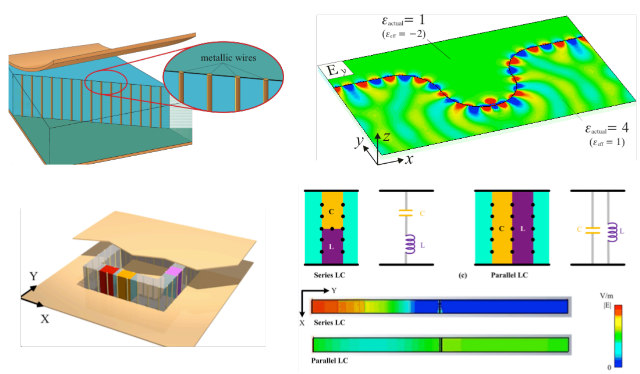

Fig. 53. Plasmonic Metasurfaces without Using Negative Dielectrics. (Top left panel): A parallel-plate waveguide (PPW) with the TE_{10} mode, exhibiting specific effective permittivity tailored by the geometric dispersion. (Top right panel): Surface plasmon polariton (SPP) at the interface between two conventional (i.e., positive permittivity) dielectric materials inside the PPW. Our simulation result is shown here for the SPP along an arbitrarily curved interface between positive-permittivity media. (Bottom left panel): Conceptual sketch of a waveguide metatronic metasurface system. The system is assumed to be composed of a PPW made of PEC top and bottom plates, operating with its TE_{10} mode near its cutoff that

produces an effective ENZ background. A square loop region with a positive dielectric [acting as "D-dotwire"] is assumed in the waveguide. Three dielectric slabs with different, though all positive real parts of permittivities are assumed to be in the dielectric loop. The response of the system effectively behaves as a series resistor-inductor-capacitor (RLC) circuit, even though all the materials have positive permittivity. (Bottom right panel): Concept of LC metasurface circuits based on waveguide metatronic metasurface using only materials with positive permittivities. The numerical simulations demonstrate that, as expected, the series LC circuit responds as a short circuit that blocks the propagation of the incident wave, whereas the parallel LC circuit responds as an open circuit with no significant impact on the propagation of the incident wave.

Metasurface Tunability via Nonlinearity and via Mechanical Actuation

We have shown before that embedding dielectric rods in an ENZ-based metasurafecs can provide structures with engineered effective magnetic permeability. Our simulations have shown that in addition to the high sensitivity of such effective permeability on the rod's permittivity and radius, the rod exhibits a hot spot for the electric field. This observation motivated us to study whether ENZ-based metasurfaces doped with Kerr nonlinear rods can lead to enhanced nonlinearity. As shown in Fig. 54, we numerically investigate this effect by choosing the rod permittivity and radius such that the slab behaves like EMNZ. In this manner, the slab is transparent at low incident intensities, but it becomes opaque as intensity increases (see Fig. 54(c) of left panel). We compare this configuration with a homogeneous slab composed of the same material as the nonlinear rod but covered with an anti-reflection coating (See Fig. 54(b) of left panel). The resulting slab is also transparent at low incident intensities, an effect, which persists up to intensities several orders of magnitude higher than the rod-embedded ENZ metasurface (in Fig. 54 (c) of left panel). Indeed, enhanced nonlinear effects can be achieved by such Kerr-doped ENZ metasurfaces. Since ENZ materials inevitably have loss, we also theoretically studied the effect of ENZ loss on the enhanced nonlinearity effect (see Fig. 54 (c) of left panel). Our parametric analysis shows that if the ENZ loss is low enough, the enhanced nonlinearity effect is maintained whereas for higher ENZ loss, this effect deteriorates. To compensate for the ENZ host, we propose to have localized gain in the rod (which can be assumed to come from optical pumping into the rod waveguide). Preliminary simulations show that for different values of ENZ loss, we can find a required amount of gain in the rod such that the transmission through the Phonically-doped ENZ structure again becomes unity. Another possible approach to achieve tunability is to exploit mechanical actuation. As shown in the right panel of Fig. 54, an air-filled hole is introduced in the ENZ metasurface, and then a smaller dielectric rod is inserted in this air hole. Displacing the rod from the center changes the properties of the particle, and thus the effective permeability of the entire slab, in turn leading to a change in the transmission coefficient (see Right panel Fig. 54). The high sensitivity of the transmission through the doped ENZ to small displacements of the rod suggests possible future implementations with mechanical actuators, and interesting possibilities in MEMS-actuated devices.

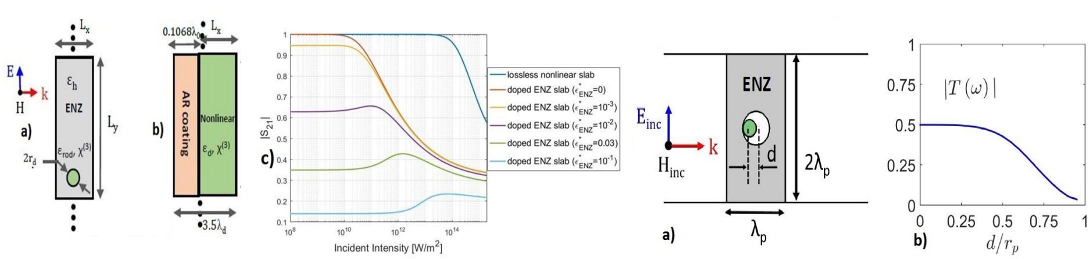

Fig. 54. Left panel (a) Non-magnetic ENZ metasurface, within which non-magnetic Kerr-nonlinear dielectric rods are embedded, realizing an effective EMNZ medium at low incident intensities. The parameters shown in the figure are chosen as $L_x = \lambda_0$, $L_y = 2\lambda_0$, $\varepsilon_{rod} = 10$, $r_d = 0.122\lambda_0$ Left penal (b) Homogeneous Kerr-nonlinear slab ($\varepsilon_d = 10$) with anti-reflection coating. Left panel (c) Comparison of the magnitude of the transmission coefficient through the lossless and lossy ENZ hosts doped with a nonlinear rod with that of a lossless homogeneous nonlinear slab. Kerr nonlinear coefficient $\chi^{(3)}=10^{-29}$ [C.m/V^3]. Right panel (a) An idea for a mechanical actuator as a thin rod inserted inside an air hole in an ENZ host; The relative permittivity of the ENZ host, the relative permittivity of the rod, and the rod radius are $\varepsilon_h = i0.03$, $\varepsilon_{rod} = 10$, $r_{rod} = 0.114\lambda_0$, respectively. Right panel (b) The transmission coefficient magnitude as a function of the rod displacement relative to the center of the hole.

Hossein Mosallaei Group

Accomplishments: The group has worked on various topics related to metasurfaces. The focus has been on metasurfaces with novel building blocks nanoantennas both plasmonic and all-dielectric, single and multilayer, and active. We have also implemented required modeling schemes. The topics can be summarized as, 1) all-dielectric metasurfaces, 2) plasmonic and all-dielectric nanoantennas building blocks, 3) multilayer configurations, 4) ITO-based tunable metasurfaces, 5) modeling and optimization.

All-Dielectric Metasurfaces, Flat and Conformal

Here we have investigated the concept of all dielectric metasurfaces. We have considered disk building blocks where electric and magnetic modes are created and offer Huygens metasurface with full transmission and controllable phase. A metasurface lens is illustrated in transmission mode. The results are shown in Fig.55 for bending performance.

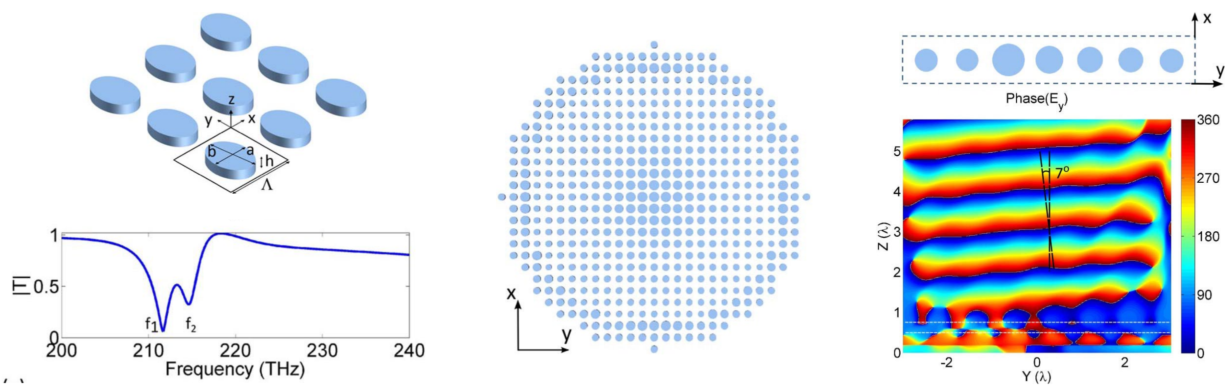

(a) (b) (c)

Fig. 55. (a) Array of dielectric metasurface and its transmission performance, (b) an all-dielectric metasurface lens, and (c) bending performance and its full wave modeling.

We then took the concept to realize an achromatic design. Basically, an issue with metasurfaces is their narrow bandwidth. This was overcome by using a filter circuit theory idea when one can in theory overcome the issue. We designed layered metasurfaces each layer to provide requires LC element then by cascading to demonstrate a metasurface with wideband performance. We have enabled this both by using plasmonic elements and only-dielectric concept, illustrated in Fig. 56. Also Fig. 56 shows results for an all-dielectric design for focusing over the entire visible band. One can clearly see achromatic performance for focusing.

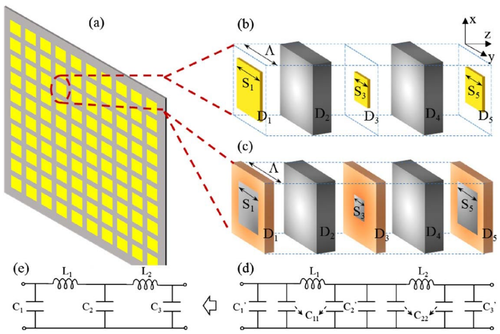

(a)

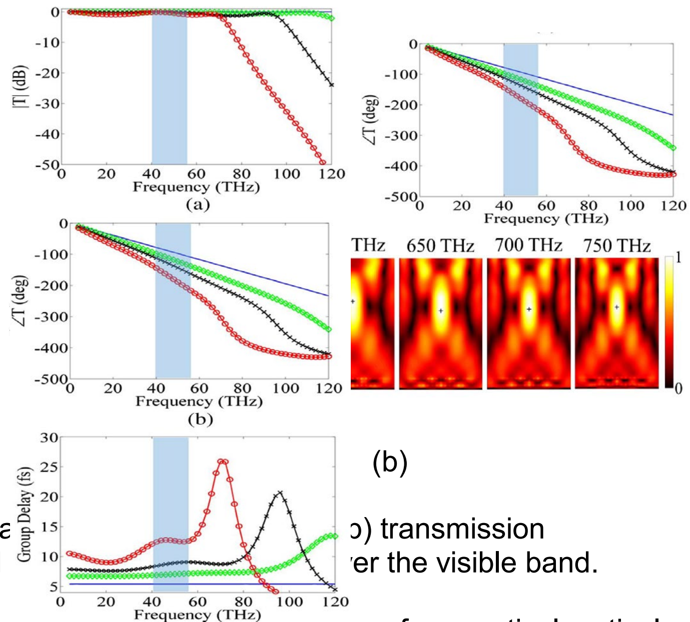

(b)

Fig. 56. (a) Layered dielectric metasurface rea… ɔ) transmission amplitude and linear phase performance, and … ɛr the visible band.

We also have worked on design and analy… ɔes for practical optical applications at 532 nm visible band for the first time. The inclusions are silicon disk nanoantennas embedded in a flexible supporting layer of polydimethylsiloxane (PDMS). They behave as local phase controllers in subwavelength dimensions for successful modification of electromagnetic responses point by point, with merits of high efficiency, at visible regime, ultrathin films, good tolerance to the incidence angle and the grid stretching due to the curvy substrate. An efficient modeling technique based on field equivalence principle is systematically proposed for characterizing metasurfaces with huge arrays of nanoantennas oriented in a conformal manner. Utilizing the robust nanoantenna inclusions and benefiting from the powerful analyzing tool, we successfully simulated the superior performance of conformal metasurfaces in two specific areas, one for lensing and compensation of spherical aberration, and the other for a carpet cloak, both at 532 nm visible spectrum (Fig.57). We have designed conformal metasurfaces for cloaking and lensing applications using all dielectric elements at 532 nm.

(a)

(b)

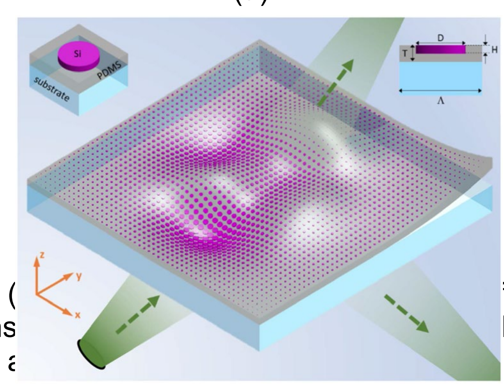

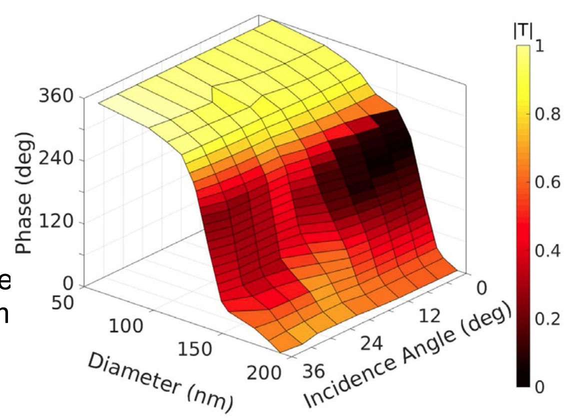

Fig. 57. (… face … n, (b) Trans… lem … e incident a…

Nanoantennas Building Blocks, Plasmonic and All-Dielectric

The group has worked extensively as part of this program to study various nanoantennas building blocks for metasurfaces, both plasmonic and all-dielectric. Figure 58 illustrates a double concentric loop. Proper design and coupling between the loops allow for full transmission and phase control as is desired. Another unique feature of this design is that for a desired phase change we must rotate the element by double the angle. It also works in transmission mode, in contrast to many metasurface in reflection mode. We have taken the idea to implement a metasurface for beam shaping as is shown in Fig. 58 (c). The metasurface does two things, 1) control the ray path to change a Gaussian beam to a flat top beam, and 2) to conjugate phase and allow uniform phase after transmission for long propagation length.

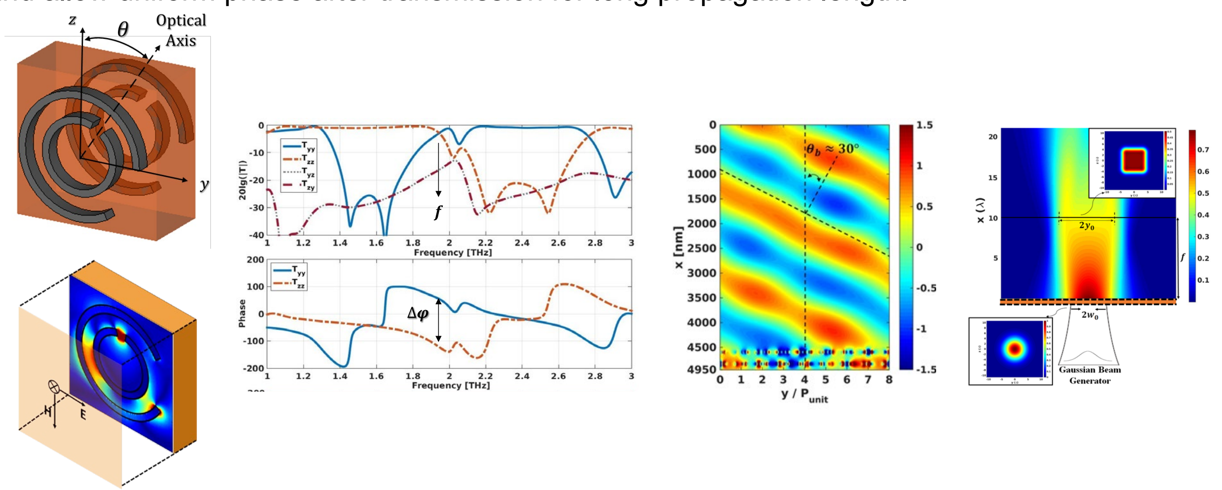

(a) (b) (c)

Figure 58. (a) Double concentric plasmonic loop for full transmission and phase control and its amplitude and phase performance, (b) bending, and (C) beam shaping performance.

A systematic study is also carried out on the interaction of electromagnetic waves with a nonsymmetric all-dielectric C-shaped nanoantenna to achieve an ultimate control over the independent and relative spectral positions of the excited magnetic and electric dipolar modes. By properly determining the structural parameters (inner and outer radii and the opening angle) and tailoring the interference of geometrical resonances, an ultrathin C-element metasurface is designed, which can highly transmit the linearly polarized incident beam (>80%) with full phase-agility (2π) in the red light of visible regime. The investigation on the physical mechanism behind this nanoantenna reveals the confinement of magnetic and electric fields corresponding to the magnetic and electric dipolar modes mainly inside the hollow and opening angle, i.e., outside the constituent high-index material of C-element. This feature allows making building blocks less dependent on the material loss and dispersion. Three different approaches based on only varying the inner/outer radius or the opening angle are proposed which can facilitate the design complexity, the encoding of the desired phase distribution for specific functionality and easing the fabrication procedure. The proposed approaches are leveraged to design several highly transparent graded-pattern metasurfaces with the capability of beam steering, focusing, flat-top generation, and holography. Figures 59 and 60 show the concept and results.

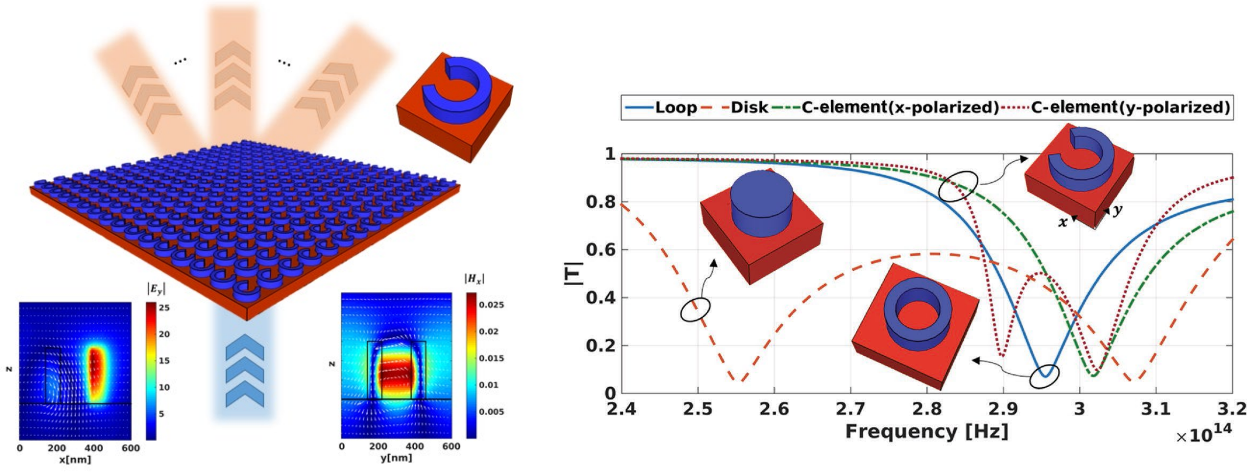

(a) (b)

Fig. 59. (a) Schematic representation of the proposed all-dielectric metasurface for beam manipulation, (b) The transmission amplitude of the periodic C-shaped unit-cell for x-polarized (dash-dotted line) and y-polarized (dotted line) incident beams. The dashed and solid lines are related to the transmission responses of two limiting cases when $R_i = 0$ and $\alpha = 0$ (nanodisk) and $R_i \neq 0$ and $\alpha = 0$ (nanoloop), respectively. The insets show the prospective views of corresponding unit-cells.

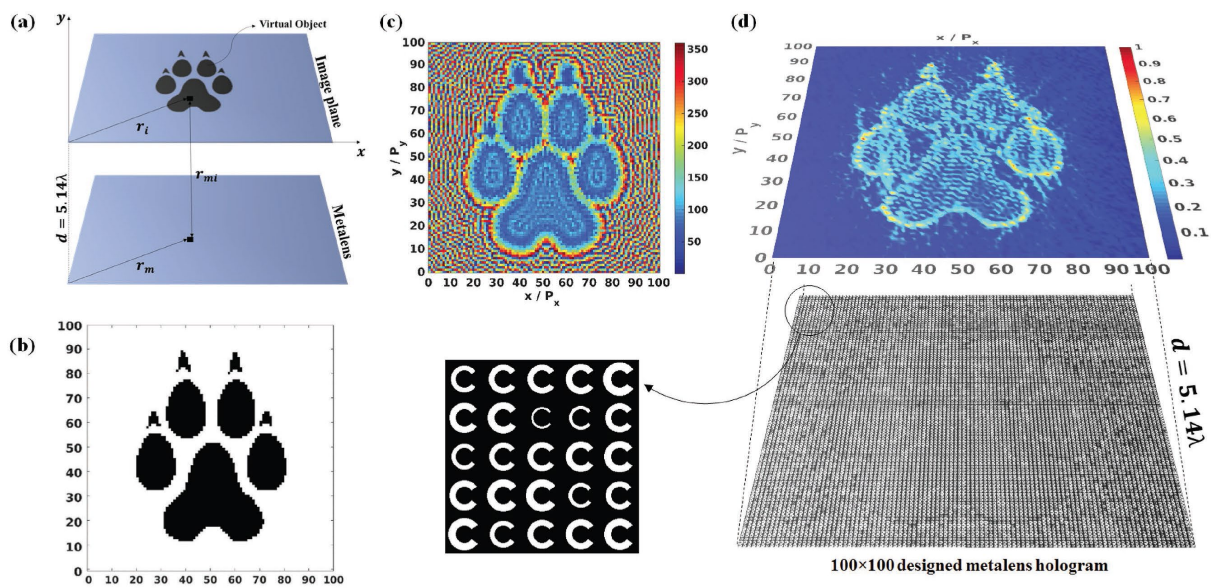

Fig. 60. (a) Schematic illustration of the metasurface hologram design. The image plane is assumed at the distance of $d = 5.14\lambda$ above the metasurface hologram where the light-emitting virtual object ("husky logo") is located. The required electric field distribution on the metalens is calculated based on the diffraction theory and mapping the electric field propagating from the virtual object. (b) The binary image of the "husky logo" which includes 100×100 pixels. The black region has the same amplitude of 1 and the white region around the object has the amplitude of 0. (c) The calculated phase distribution of the electric field on the metasurface plane. (d) The numerically calculated amplitude of the electric field distribution at the image plane ($d = 5.14\lambda$) at the operating frequency of 430 THz. The holographic image is produced by 100×100 array of C-elements with only varying outer radius (this is a very huge array size we have modeled).

Voltage Tunable Metasurfaces Enabled by ITO

We have worked extensively on tunable metasurfaces using ITO materials. This is to have controllable behavior in real-time by applying voltages to ITO. One of our works in this area has been a 2016 highlight in Journal of Optics.

In our work we designed two electrically tunable dual-band reflectarray antennas by the integration of 61a thin layer of indium tin oxide (ITO) into plasmonic multi-sized and multilayer unit cells (Fig. 61a). The presented geometries include two gold nanoribbons located next to each other with different widths and backed by a stack of alumina-ITO-metallic ground plane and two pairs of vertically stacked gold nanoribbon-alumina-ITO on a metallic ground plane. The double-resonance nature of the double metal-insulator metal unit-cells is exploited to achieve two distinct operating frequencies in which the control over phase of the reflected beam is obtained via the tunable gate biasing of ITO (Fig. 61 (b)-(e). An in-depth phased array analysis is developed with emphasis on the accomplishment of a reconfigurable antenna with robust beam scanning and focusing characteristics. The proposed structures can be considered as dual-band bifunctional reflectarray antenna that can operate at two distinct frequencies in the near-infrared regime with two different functionalities as bending and focusing.

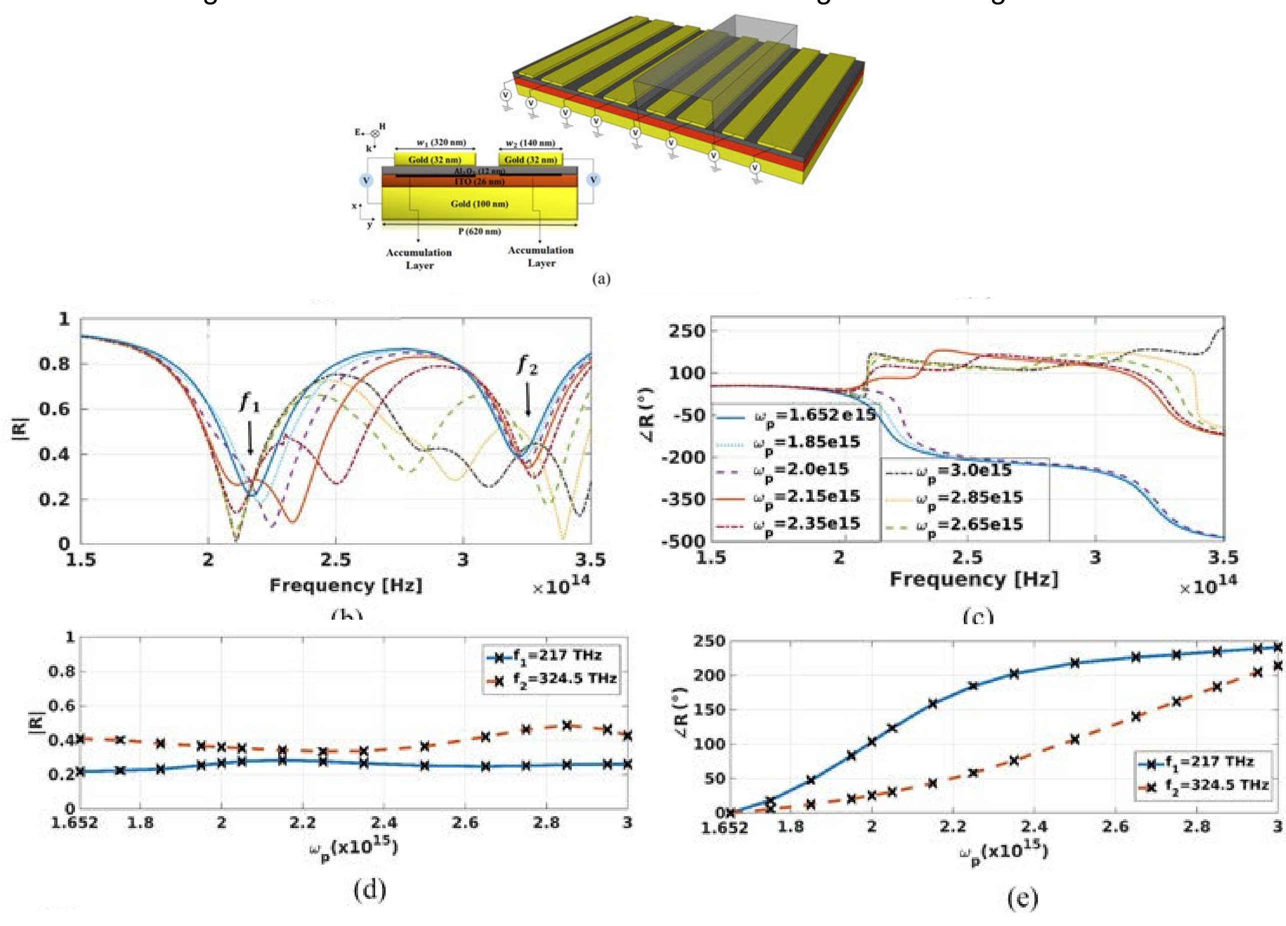

Fig. 61. (a) Schematic overview of the electrically tunable dual-band reflectarray structure. The bi-MIM unit-cell includes two nanoribbons which are placed on a stack of Al_2O_3-ITO-gold back mirror. FDTD full-wave simulation results for the reflection (b) amplitude and (c) phase of the unit-cell versus

frequency for different plasma frequencies of the accumulation layers of ITO in the range from 1.652×10^{15} to 3×10^{15} rad/s. (d)-(e) The reflection amplitude and relative phase change (the reflection phase of the unbiased case is assumed zero) at the operating frequencies of 217 and 324.5 THz. Both gold nanoribbons are assumed under influence of the same DC voltage bias.

Modeling and Optimization

Data Driven Activation (DDA)Technique

Advances in the field of metasurfaces require simulation of large-scale metasurfaces that extend over many light wavelengths. Adopting standard numerical methods leads to models featuring many degrees of freedom, which are prohibitive to solve within a time window compatible with the design workflow. This requires developing the techniques to replace large-scale computational models with simpler ones, still capable of capturing the essential features but imposing a fraction of the initial computational costs. In this work, we present a simulation approach in order to handle reduced order analyses of large-scale metasurfaces of arbitrary elements. We use the discrete dipole approximation in conjunction with the discrete complex image method and hierarchical matrix construction as a common theoretical framework for dipole approximation in the hierarchy of individual elements and the array scale. We extract the contributions of multipoles in the scattering spectra of the nanoantennas forming the metasurface and retrieve their dynamic polarizabilities. The computational complexity of modeling the array problem is then significantly reduced by replacing the fine meshing of each nanoantenna with its dynamic polarizability. The solver is developed to model several fully functional metasurfaces of different types including a one-atom-thick metasurface made of graphene with chemical doping interruptions, a multi-focusing lens made of plasmonic V-shaped nanoantennas, and a multicolor hologram consisting of dielectric nanobars. The performance of the method is evaluated through comparison with full-wave simulations, and a significant computational gain is observed while the accuracy of the results is retained owing to the preserved coupling information between dipolar modes.

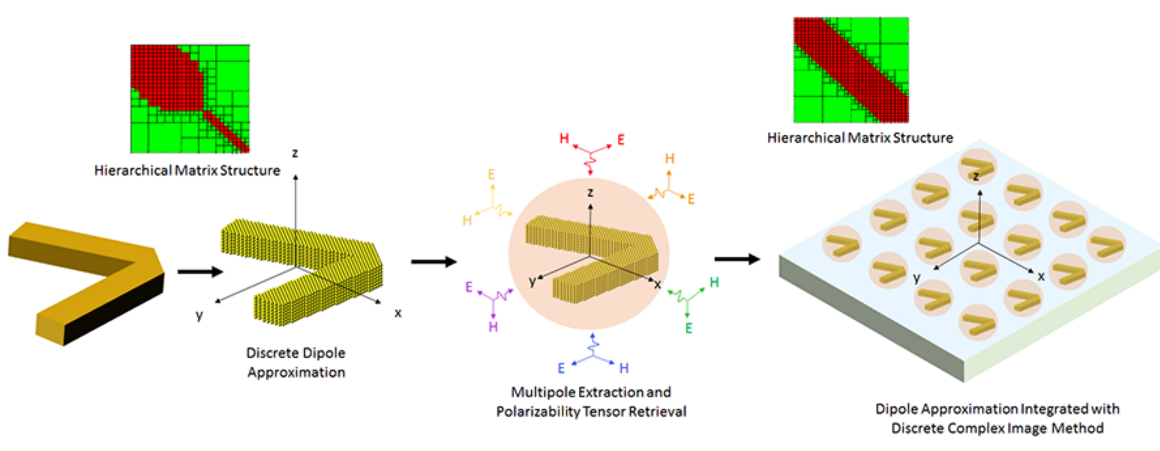

Fig. 62. Schematic of the hierarchical multiscale DDA modeling

Optimization Based Metasurfaces

Synthetization of multiple functionalities over a flat metasurface platform offers a promising approach to achieving integrated photonic devices with minimized footprint. Metasurfaces capable of diverse wavefront shaping according to wavelengths and polarizations have been demonstrated. Here we propose a class of angle-selective metasurfaces, over which beams are reflected following different and independent phase gradients in the light of the beam direction. Such powerful feature is achieved by leveraging the local phase modulation and the non-local lattice diffraction via inverse scattered field and geometry optimization in a monolayer dielectric grating, whereas most of the previous designs utilize the local phase modulation only and operate optimally for a specific angle. Beam combiner/splitter and independent multibeam deflections with up to 4 incident angles are numerically demonstrated respectively at the wavelength of 700 nm (Fig. 63). The deflection efficiency is around 45% due to the material loss and the compromise of multi-angle responses. Flexibility of the approach is further validated by additional designs of angle-switchable metagratings as splitter/reflector and transparent/opaque mirror. The proposed designs hold great potential for increasing information density of compact optical components from the degree of freedom of angle.

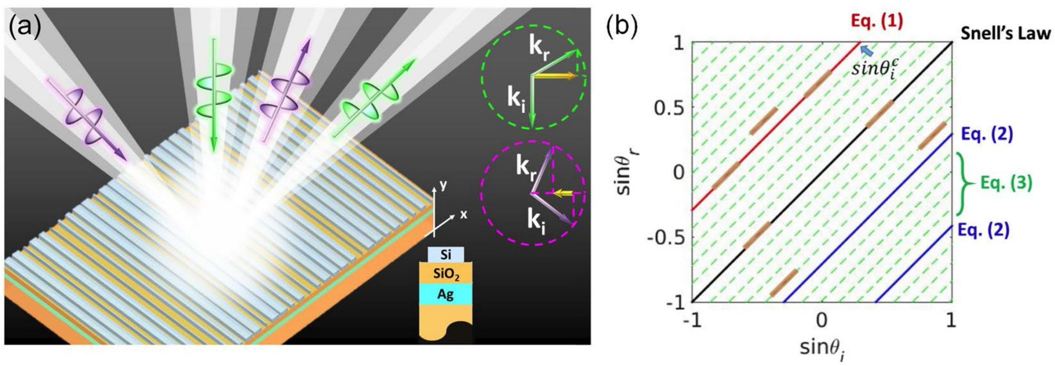

Fig. 63. (**a**) Optimized metagrating for angle-selective beam deflection. Different phase gradients can be seen by beams from different directions, leading to independent beam deflections controlled by angle. The momentum conservation is illustrated in the upper right corner, with the metasurface phase gradient represented by the yellow arrow. The reflective grating element is shown in the lower right corner. (**b**) Snell's law of reflection and its generalization.

Adaptive Genetic Algorithm Based Design

As optical metasurfaces become progressively sophisticated, the expectations from them are becoming increasingly complex. The limited number of structural parameters in the conventional metasurface building blocks, and existing phase engineering rules do not completely support the growth rate of metasurface applications. We present digitized-binary elements, as alternative high dimensional building blocks, to accommodate the needs of complex-tailorable-multifunctional applications. To design these complicated platforms, we demonstrate adaptive genetic algorithm (AGA), as a powerful evolutionary optimizer, capable of handling such demanding design expectations (Fig.65). We solve four complex problems of high current interest to the optics community, namely, a binary pattern plasmonic reflectarray with high tolerance to fabrication imperfections and high reflection efficiency for beam-steering purposes, a dual-beam aperiodic leaky-wave antenna, which diffracts TE and TM excitation waveguides modes to arbitrarily chosen directions, a compact birefringent all dielectric metasurface with finer pixel resolution compared to canonical nanoantennas, and a visible transparent infrared emitting/absorbing metasurface that shows high promise for solar-cell cooling applications, to showcase the advantages of the combination of binary-pattern metasurfaces and the AGA technique. Each of these novel applications encounters computational and fabrication challenges under conventional design methods and is chosen carefully to highlight one of the unique advantages of the AGA technique. We show that large surplus datasets produced as by-products of the evolutionary optimizers can be employed as ingredients of the new-age computational algorithms, such as, machine learning and deep leaning. In doing so, we open a new gateway of predicting the solution to a problem in the fastest possible way based on statistical analysis of the datasets rather than researching the whole solution space.

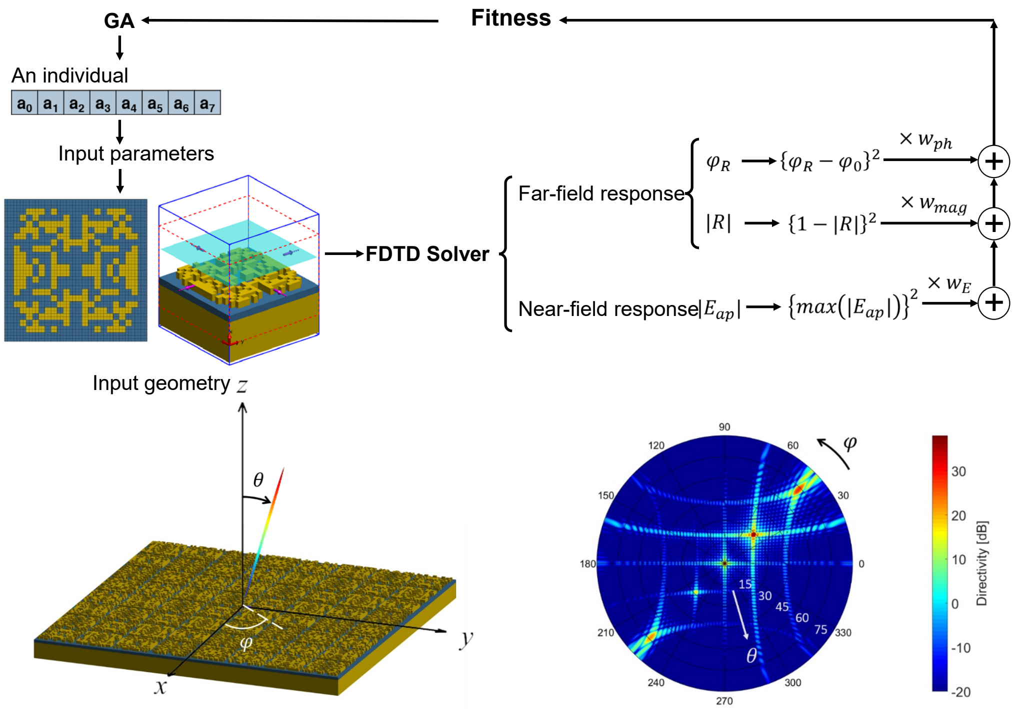

Fig. 64. GA optimized metasurface and associated cost function, designed metasurface, and the beam scanning in space implemented by the optimized metasurface.

The next step in the field will be optics design by AI. This would need sophisticated advanced modeling along active learning to manage minimum training pool. The materials presented in this section will lead to successful inverse designs for multifunctional optical systems.

3. Outlook

The nascent and multidisciplinary field of flat optics is about to take-off, as indicated by World Economic Forum as one of top ten emerging technologies of 2019 (https://innovationorigins.com/top-10-emerging-technologies-3-tiny-lenses/) and predicted by Lux Research for 10 billion market opportunity by 2030 (http://web.luxresearchinc.com/metamaterials-executive-summary). Scientific American has listed metalenses as one the top emerging technologies of the year https://www.scientificamerican.com/article/top-10-emerging-technologies-of-2019/ .

To fuel this expansion and to support continuing innovation at the physics, device and system levels, new powerful design tools supported by adequate AI will be needed and new strategies for merging at the design level hardware and software.

Inverse-designed Photonics based Neural/Neuromorphic Networks

The inverse design has become an exciting tool in nanophotonics, as one can achieve more complex, unintuitive, non-periodic structures whose degrees of freedom can be much higher than conventional periodic counterparts, allowing counterintuitive photonic geometries that can provide desired functionalities. For example, the Engheta group has recently designed, constructed, and tested a metastructure that can solve integral equations as waves traverse it, effectively developing the steps towards ultrafast, wave-based, material-based analog computing metamaterial machines. The computational tools of inverse design have mostly been directed to design linear photonic metasurfaces and structures and we expect major impact in designing entire large area devices such as metalenses rather than resorting to models based on periodic boundary conditions. Furthermore, applying the methodology of inverse design to nonlinear phenomena in photonics can significantly open numerous possibilities for structures with multifunctionalities (i.e., function multiplexing) and more complex optical properties.

Nonlinearity is one of the essential ingredients in the data-driven machine learning and neural networks, and therefore nonlinear optics, when merged with the inverse design, can lead to a paradigm shift in neuromorphic photonics. Many algorithmic steps in computation, which involve iterations, can benefit from optics which is inherently ultrafast. Applying inverse design to neural networks will significantly expand the possibilities of optics-based machine learning.

Deep optics

The current understanding of metasurfaces and recent developments in computational imaging systems is now giving rise to an exciting new opportunity to realize Deep Optics. In Deep Optics, metasurface optics can be co-optimized with advanced digital image processing techniques to create hybrid optical-electronic neural networks capable of performing advanced image processing tasks at unparalleled speed and low power consumption. An early example is the realization of the depth camera by the Capasso group, discussed in this report, where by co-designing the hardware (metalens) and the software (algorithm) the computational burden inherent in stereo and time of flight depth cameras has been reduced by a more than one order of magnitude.
We envision that next-generation computational imaging systems. will be composed of a series of stacked, nanostructured optical layers that derive their functionality from the specific way in

which they are patterned as well as the non-linear optical materials that can be incorporated in these layers. If successful, basic image processing tasks can be performed as light flows through these stacks.

The types of data contained in digital images can take many forms and a wide range of algorithms have been developed to mine for desired information. It is the focus of the computational imaging field to extract high-dimensional data from images and transform it into useful numerical or symbolic information that can be further processed, interpreted and used in decision making. With advances in deep learning with artificial neural networks, digital computers are now able to analyze images with a logic structure that is like how we think. As a result, the ability of image processing systems is now starting to approach that of humans and it is possible to e.g. recognize complex objects, people, handwritten or printed texts. Digital electronics can perform a wide range of complex image analysis tasks. However, there are many imaging applications that require high-throughput, real-time, and low power image processing for which digital electronics is not ideally suited. To enable such applications, we aim to off-load certain critical and computationally-intensive tasks to passive, non-energy consuming, and fast flat optics.

The optical elements, that we envision using are metasurface based. A simple example is a metalens, which (like a conventional lens) can perform a Fourier transformation. Unlike conventional electronic computers, optical metasurfaces can run massively parallel computations in the array of densely packed meta-elements. Advanced image processing units and optical convolutional neural network (CNN) can also be created by cascading the linear and nonlinear metasurfaces with dynamic tunability. To enable this advance, new antennas and metasurface design will need to be created using inverse or topological optimization. New non-linear materials and dynamic antenna elements will need to be created. Fundamentally new strategies to co-optimize digital image processing and metasurface hardware need to be constructed. New large-area and 3-dimensional fabrication processes need to be realized.

4. Publications

Nanfang Yu Group

1. A. C. Overvig, S. Shrestha, S. C. Malek, M. Lu, A. Stein, C. Zheng, and N. Yu, “Dielectric metasurfaces for complete and independent control of optical amplitude and phase,” *Light: Science & Applications* vol. **8**, 92 (2019).
2. J. Mandal, M. Jia, A. C. Overvig, Y. Fu, E. Che, N. Yu, and Y. Yang*, “Porous polymers with switchable optical transmittance for optical and thermal regulation,” *Joule* vol. **3**, 1–12 (2019).
3. W. A. Britton, R. Zhang, S. Shrestha, Y. Chen, N. Yu, and L. Dal Negro*, “Indium silicon oxide thin films for infrared metaphotonics,” *Applied Physics Letters* vol. **114**, 161105 (2019).
4. Z. Li*, Y. Zhu, Y. Hao, M. Gao, M. Lu, A. Stein, A.-H. A. Park, J. C. Hone, Q. Lin*, and N. Yu*, “Hybrid metasurface-based mid-infrared biosensor for simultaneous quantification and identification of monolayer protein,” *ACS Photonics* vol. **6**, 501–509 (2019).
5. S. Shrestha, A. C. Overvig, M. Lu, A. Stein, and N. Yu*, “Broadband achromatic dielectric metalenses,” *Light: Science & Applications* vol. **7**, 85 (2018).
6. J. Mandal, Y. Fu, A. Overvig, M. Jia, K. Sun, N. N. Shi, H. Zhou, X. Xiao, N. Yu*, and Y. Yang*, “Hierarchically porous polymer coatings for highly efficient passive daytime radiative cooling,” *Science* vol. **362**, 315–319 (2018).

7. Y. Zhu, Z. Li, Z. Hao, C. DiMarco, P. Maturavongsadit, Y. Hao, M. Lu, A. Stein, Q. Wang, J. Hone, N. Yu* and Q. Lin*, "Optical conductivity-based ultrasensitive mid-infrared biosensing on a hybrid metasurface," *Light: Science & Applications* vol. **7**, 67 (2018).
8. N. N. Shi, C.-C. Tsai, M. J. Carter, J. Mandal, A. C. Overvig, M. Y. Sfeir, M. Lu, C. L. Craig, G. D. Bernard, Y. Yang, and N. Yu*, "Nanostructured fibers as a versatile photonic platform: Radiative cooling and waveguiding through transverse Anderson localization," *Light: Science & Applications* vol. **7**, 37 (2018).
9. J. Mandal, S. Du, M. Dontigny, K. Zaghib, N. Yu*, and Y. Yang*, "Li4Ti5O12: A visible-to-infrared broadband electrochromic material for optical and thermal management," *Advanced Functional Materials* vol. **28**, 1802180 (2018).
10. S. Shrestha, Y. Wang, A. C. Overvig, M. Lu, A. Stein, L. Dal Negro, and N. Yu*, "Indium tin oxide broadband metasurface absorber," *ACS Photonics* vol. **5**, 3526–3533 (2018).
11. A. C. Overvig, S. Shrestha, and N. Yu*, "Dimerized high contrast gratings," *Nanophotonics* vol. **7**, 1157–1168 (2018).
12. Z. Zhang, D. Schwanz, B. Narayanan, M. Kotiuga, J. A. Dura, M. Cherukara, H. Zhou, J. W. Freeland, J. Li, R. Sutarto, F. He, C. Wu, J. Zhu, Y. Sun, K. Ramadoss, S. S. Nonnenmann, N. Yu, R. Comin, K. M. Rabe, S. K. R. S. Sankaranarayanan, and S. Ramanathan*, "Perovskite nickelates as electric-field sensors in salt water," *Nature* vol. **553**, 68–72 (2018).
13. Z. Li, M.-H. Kim, C. Wang, Z. Han, S. Shrestha, A. C. Overvig, M. Lu, A. Stein, A. M. Agarwal, M. Lončar, and N. Yu*, "Controlling propagation and coupling of waveguide modes using phase-gradient metasurfaces," *Nature Nanotechnology* vol. **12**, 675–683 (2017).
14. C. Wang, Z. Li, M.-H. Kim, X. Xiong, X.-F. Ren, G.-C. Guo, N. Yu*, and M. Loncar*, "Metasurface-assisted phase-matching-free second harmonic generation in lithium niobate waveguides," *Nature Communications* vol. **8**, 2098 (2017).
15. J. Mandal, D. Wang, A. C. Overvig, N. N. Shi, D. Paley, A. Zangiabadi, Q. Cheng, K. Barmak, N. Yu*, and Yuan Yang*, "Scalable, 'dip-and-dry' fabrication of a wide-angle plasmonic selective absorber for high-efficiency solar–thermal energy conversion," *Advanced Materials* vol. **29**, 1702156 (2017).
16. Y. Wang, A. C. Overvig, S. Shrestha, R. Zhang, R. Wang, N. Yu, and L. Dal Negro*, "Tunability of indium tin oxide materials for mid-infrared plasmonics applications," *Optical Materials Express* vol. **7**, 2727–2739 (2017).
17. Z. Li, Y. Zhou, H. Qi, Q. Pan, Z. Zhang, N. N. Shi, M. Lu, A. Stein, C. Y. Li, S. Ramanathan*, and N. Yu*, "Correlated perovskites as a new platform for super broadband tunable photonics," *Advanced Materials* vol. **28**, 9117–9125 (2016).
18. S. Zhang, M. H. Kim, F. Aieta, A. She, T. Mansuripur, I. Gabay, M. Khorasaninejad, D. Rousso, X. Wang, M. Troccoli, N. Yu, and F. Capasso*, "High efficiency near diffraction-limited mid-infrared flat lenses based on metasurface reflectarrays," *Optics Express* vol. **24**, 18024–18034 (2016).
19. H.-T. Chen*, A. J. Taylor*, and N. Yu*, "A review of metasurfaces: physics and applications," *Reports on Progress in Physics* vol. **79**, 076401 (2016).
20. N. N. Shi, C.-C. Tsai, F. Camino, G. D. Bernard, N. Yu*, R. Wehner*, "Keeping cool: Enhanced optical reflection and radiative heat dissipation in Saharan silver ants," *Science* vol. **349**, 298–301 (2015).
21. N. Yu* and F. Capasso*, "Optical metasurfaces and prospect of their applications including fiber optics," *IEEE Journal of Lightwave Technology* vol. **33**, 2344 (2015).
22. N. Yu* and F. Capasso*, "Flat optics with designer metasurfaces," *Nature Materials* vol. **13**, 139–150 (2014).

Purdue Team

23. K. Chaudhuri *et al.*, "Photonic Spin Hall Effect in Robust Phase Gradient Metasurfaces

utilizing Transition Metal Nitrides," *ACS Photonics*, vol. 6, no. 1, pp. 99–106, Jan. 2019.
24. A. Boltasseva and V. M. Shalaev, "Transdimensional Photonics," *ACS Photonics*, vol. 6, no. 1, pp. 1–3, Jan. 2019.
25 A. Dutta, D. Wan, B. Yan, V. M. Shalaev, T. Venkatesan, and A. Boltasseva, "Strontium Niobate for Near-Infrared Plasmonics," *Adv. Opt. Mater.*, vol. 7, no. 19, p. 1900401, Oct. 2019.
25. D. Wang *et al.*, "Spatial and Temporal Nanoscale Plasmonic Heating Quantified by Thermoreflectance," *Nano Lett.*, vol. 19, no. 6, pp. 3796–3803, Jun. 2019.
26. P. Nyga *et al.*, "Laser-induced color printing on semicontinuous silver films: red, green and blue," *Opt. Mater. Express*, vol. 9, no. 3, p. 1528, Mar. 2019.
27. M. Song, Z. A. Kudyshev, H. Yu, A. Boltasseva, V. M. Shalaev, and A. V. Kildishev, "Achieving full-color generation with polarization-tunable perfect light absorption," *Opt. Mater. Express*, vol. 9, no. 2, p. 779, Feb. 2019.
28. A. M. Shaltout *et al.*, "Spatiotemporal light control with frequency-gradient metasurfaces," *Science*, vol. 365, no. 6451, pp. 374–377, Jul. 2019.
29. A. M. Shaltout, V. M. Shalaev, and M. L. Brongersma, "Spatiotemporal light control with active metasurfaces," *Science*, vol. 364, no. 6441, p. eaat3100, May 2019.
30. M. Li *et al.*, "Plasmonic Biomimetic Nanocomposite with Spontaneous Subwavelength Structuring as Broadband Absorbers," *ACS Energy Lett.*, vol. 3, no. 7, pp. 1578–1583, Jul. 2018.
31. D. Shah *et al.*, "Controlling the Plasmonic Properties of Ultrathin TiN Films at the Atomic Level," *ACS Photonics*, vol. 5, no. 7, pp. 2816–2824, Jul. 2018.
32. S. K. H. Andersen *et al.*, "Hybrid Plasmonic Bullseye Antennas for Efficient Photon Collection," *ACS Photonics*, vol. 5, no. 3, pp. 692–698, Mar. 2018.
33. K. Chaudhuri, M. Alhabeb, Z. Wang, V. M. Shalaev, Y. Gogotsi, and A. Boltasseva, "Highly Broadband Absorber Using Plasmonic Titanium Carbide (MXene)," *ACS Photonics*, vol. 5, no. 3, pp. 1115–1122, 2018.
34.J. Kim *et al.*, "Dynamic Control of Nanocavities with Tunable Metal Oxides," *Nano Lett.*, vol. 18, no. 2, pp. 740–746, Feb. 2018.
35. S. M. Choudhury *et al.*, "Material platforms for optical metasurfaces," *Nanophotonics*, vol. 7, no. 6, pp. 959–987, Jun. 2018.
36. A. M. Shaltout, J. Kim, A. Boltasseva, V. M. Shalaev, and A. V Kildishev, "Ultrathin and multicolour optical cavities with embedded metasurfaces," *Nat. Commun.*, vol. 9, no. 1, p. 2673, Dec. 2018.
37 C. T. DeVault *et al.*, "Suppression of near-field coupling in plasmonic antennas on epsilon-near-zero substrates," *Optica*, vol. 5, no. 12, p. 1557, Dec. 2018.
38. M. Henstridge *et al.*, "Synchrotron radiation from an accelerating light pulse," *Science*, vol. 362, no. 6413, pp. 439–442, Oct. 2018.
39. M. Henstridge *et al.*, "Accelerating light with metasurfaces," *Optica*, vol. 5, no. 6, p. 678, Jun. 2018.
40. H. Reddy *et al.*, "Temperature-Dependent Optical Properties of Single Crystalline and Polycrystalline Silver Thin Films," *ACS Photonics*, vol. 4, no. 5, pp. 1083–1091, 2017.
41. S. Choudhury, U. Guler, A. Shaltout, V. M. Shalaev, A. V. Kildishev, and A. Boltasseva, "Pancharatnam-Berry Phase Manipulating Metasurface for Visible Color Hologram Based on Low Loss Silver Thin Film," *Adv. Opt. Mater.*, vol. 5, no. 10, p. 1700196, May 2017.
42 J. Fang *et al.*, "Enhanced Graphene Photodetector with Fractal Metasurface," *Nano Lett.*, vol. 17, no. 1, pp. 57–62, Jan. 2017.
43. M. Clerici *et al.*, "Controlling hybrid nonlinearities in transparent conducting oxides via two-colour excitation," *Nat. Commun.*, vol. 8, no. 1, p. 15829, Aug. 2017.
44. V. A. Zenin, S. Choudhury, S. Saha, V. M. Shalaev, A. Boltasseva, and S. I. Bozhevolnyi, "Hybrid plasmonic waveguides formed by metal coating of dielectric ridges," *Opt. Express*, vol. 25, no. 11, p. 12295, May 2017.

45. O. A. Makarova, M. Y. Shalaginov, S. Bogdanov, A. V. Kildishev, A. Boltasseva, and V. M. Shalaev, "Patterned multilayer metamaterial for fast and efficient photon collection from dipolar emitters," *Opt. Lett.*, vol. 42, no. 19, p. 3968, Oct. 2017.
46. J. Kim *et al.*, "Controlling the Polarization State of Light with Plasmonic Metal Oxide Metasurface," *ACS Nano*, vol. 10, no. 10, pp. 9326–9333, Oct. 2016.
47. J. Kim *et al.*, "Role of epsilon-near-zero substrates in the optical response of plasmonic antennas," *Optica*, vol. 3, no. 3, p. 339, Mar. 2016.
48. L. Caspani *et al.*, "Enhanced Nonlinear Refractive Index in ϵ-Near-Zero Materials," *Phys. Rev. Lett.*, vol. 116, no. 23, p. 233901, Jun. 2016.
49. A. M. Shaltout *et al.*, "Development of Optical Metasurfaces: Emerging Concepts and New Materials," *Proc. IEEE*, 2016.
50. F. Ding, Z. Wang, S. He, V. M. Shalaev, and A. V. Kildishev, "Broadband High-Efficiency Half-Wave Plate: A Supercell-Based Plasmonic Metasurface Approach," *ACS Nano*, vol. 9, no. 4, pp. 4111–4119, Apr. 2015.
51. R. Chandrasekar *et al.*, "Second harmonic generation with plasmonic metasurfaces: direct comparison of electric and magnetic resonances," *Opt. Mater. Express*, vol. 5, no. 11, p. 2682, Nov. 2015.
52. P. R. West *et al.*, "All-dielectric subwavelength metasurface focusing lens," *Opt. Express*, vol. 22, no. 21, p. 26212, Oct. 2014.

Brongersma Group

53. M. Miyata, A. Holsteen, Y. Nagasaki, M.L. Brongersma, and J. Takahara, "Gap Plasmon Resonance in a Suspended Plasmonic Nanowire Coupled to a Metallic Substrate," Nano Letters, 15, 5609-5616 (2015).
54. Dianmin Lin, Aaron L. Holsteen, Elhanan Maguid, Gordon Wetzstein, Pieter G. Kik, Erez Hasman, Mark L. Brongersma "Photonic multitasking interleaved Si nanoantenna phased array," Nano Letters, 16, 7671 (2016).
55. Optically resonant dielectric nanostructures," Arseniy I. Kuznetsov, Andrey E. Miroshnichenko, Mark L. Brongersma, Yuri S. Kivshar, Boris Luk'yanchuk, Science, 354, 846 (2016).
56. "Photonic multitasking interleaved Si nanoantenna phased array," Dianmin Lin, Aaron L. Holsteen, Elhanan Maguid, Gordon Wetzstein, Pieter G. Kik, Erez Hasman, Mark L. Brongersma, Nano Letters 16, 7671 (2016).
57 Aaron Holsteen, Soren. Raza, Pengyu Fan, Pieter G. Kik, Mark L. Brongersma, "Purcell effect for active tuning of light scattering from semiconductor optical antennas," Science 358, 1407–1410 (2017).
58 Yeonsang Park, Jineun Kim, Kyung-Sang Cho, Hyochul Kim, Min-kyung Lee, Jae-soong Lee, Un Jeong Kim, Sung Woo Hwang, Mark L. Brongersma, Young-Geun Roh, and Q-Han Park, "Metasurface electrode light emitting diodes with planar light control" Scientific Reports 7, 14753-14753 (2017).
59. Dianmin Lin, Aaron L. Holsteen, Elhanan Maguid, Pengyu Fan, Pieter G. Kik, Erez Hasman, Mark L. Brongersma, "Polarization-independent metasurface lens employing the Pancharatnam-Berry phase," Optics Express 26, 24835-24842 (2018).
60.Soongyu, Yi, Ming Zhou, Zongfu Yu, Pengyu Fan, Nader Behdad, Dianmin Lin, Shanhui Fan, and Mark L Brongersma, "Subwavelength Angle-Sensing Photodetectors Inspired by Directional Hearing in Small Animals" Nature Nanotechnology 13, 1143–1147 (2018).
61. Aaron L. Holsteen, Ahmet F. Cihan, Mark L. Brongersma "Temporal color mixing and dynamic beam shaping with silicon metasurfaces," Science, 365, 257-260 (2019).
62. Amr M. Shaltout, Vladimir M. Shalaev, Mark L. Brongersma, "Spatiotemporal light control with active metasurfaces," Science 364, eaat3100 (2019).

63.“Spatiotemporal light control with frequency-gradient metasurfaces,” Amr M. Shaltout, Konstantinos G. Lagoudakis, Jorik van de Groep, Soo Jin Kim, Jelena Vučković, Vladimir M. Shalaev, and Mark L. Brongersma, Science 365, 374-377 (2019)

Capasso group

64. N. Yu and F. Capasso, “Optical metasurfaces and prospect of their applications including fiber optics,” IEEE Journal of Lightwave Technology 33, 2344 (2015)
65. Patrice Genevet, Daniel Wintz, Antonio Ambrosio, Alan She, Romain Blanchard and Federico Capasso “Controlled steering of Cherenkov surface plasmon wakes with a one-dimensional metamaterial” Nature Nanotechnology 10, 804 (2015)
66. Francesco Aieta, Mikhail Kats, Patrice Genevet, Federico Capasso, “Multiwavelength Achromatic Metasurfaces by Dispersive Phase Compensation”, Science 347, 1342 (2015)
67. Mohammadreza Khorasaninejad, Francesco Aieta, Pritpal Kanhaiya, Mikhail A. Kats, Patrice Genevet, David Rousso, and Federico Capasso, “Achromatic Metasurface Lens at Telecommunication Wavelengths” Nano Letters 5, 5358(2015)
68. Mohammadreza Khorasaninejad and Federico Capasso, “Broadband Multifunctional Efficient Meta-Gratings Based on Dielectric Waveguide Phase Shifters”, Nano Lett., DOI: 10.1021/acs.nanolett.5b02524, 2015
69. Robert C. Devlin, Mohammadreza Khorasaninejad, Wei Ting Chen, Jaewon Oh, and Federico Capasso “Broadband high-efficiency dielectric metasurfaces for the visible spectrum” *Proceedings of the National Academy of Sciences* 113, 10473 (2016)
70. M. Khorasaninejad, W.T. Chen, R. C. Devlin, J. Oh, A. Zhu, and F. Capasso, “Metalenses at visible wavelengths: Diffraction-limited focusing and subwavelength resolution imaging” *Science* **352**, 1190 (2016) *(featured on the cover)*
71. M. Khorasaninejad, W.T. Chen, A.Y. Zhu, J. Oh, R.C. Devlin, D. Rousso, and F. Capasso “Multispectral Chiral Imaging with a Metalens” *Nano Letters* 16, 4595 (2016) (*Editor’s choice)*
72. Shuyan Zhang, Myoung-Hwan Kim, Francesco Aieta, Alan She, Tobias Mansuripur, Ilan Gabay, Mohammadreza Khorasaninejad, David Rousso, Xiaojun Wang, Mariano Troccoli, Nanfang Yu, and Federico Capasso, “High efficiency near diffraction-limited mid-infrared flat lenses based on metasurface reflectarrays” Optics Express 24, 18024 (2016)
73. M. Khorasaninejad, W. T. Chen, J. Oh, and F. Capasso, “Super-Dispersive Off-Axis Meta-Lenses for Compact High Resolution Spectroscopy”, Nanoletters 16, 3732 (2016)
74. Jura Rensberg, Shuyan Zhang, You Zhou, Alexander S. McLeod, Christian Schwarz, Michael Goldflam, Mengkun Liu, Jochen Kerbusch, Ronny Nawrodt, Shriram Ramanathan, D. N. Basov, Federico Capasso, Carsten Ronning, and Mikhail A. Kats “Active Optical Metasurfaces Based on Defect-Engineered Phase- Transition Materials” Nanoletters 16, 1050 (2016)
75. Andrea Fratalocchi, Henning Galinsky, Gael Favraud, Hao Dong, Juan Sebatian Totero Gongora, Gregory Favaro, Max Dobeli, Ralph Spolenak, and Federico Capasso "Scalable, ultra-resistant structural colors based on network metamaterials" Light: Science and Applications 6, 16233 (2017)
76. J. Rensberg, Y. Zhou, S. Richter, C. Wan, S. Zhang, P. Schöppe, R. Schmidt-Grund, S. Ramanathan, F. Capasso, M.A. Kats, and C. Ronning, Physical Review Applied 8, 14009 (2017)
77. Mohammadreza Khorasaninejad, Zhujun Shi, Wei-Ting Chen, Vyshakh Sanjeev, Aun Zaidi, and Federico Capasso “Achromatic metalens over 60 nm bandwidth in the visible and metalens with reverse chromatic dispersion” Nano Letters 17, 1819 (2017)

78. Patrice Genevet, Federico Capasso, Francesco Aieta, Mohammadreza Khorasaninejad, and Robert Devlin “Recent advances in planar optics: from plasmonic to dielectric metasurfaces” Optica 4, 139 (2017)
79. Robert C. Devlin, Antonio Ambrosio, Daniel Wintz, Stefano Luigi Oscurato, Alexander Yutong Zhu, Mohammadreza Khorasaninejad, Jaewon Oh, Pasqualino Maddalena, and Federico Capasso “Spin-to-orbital angular momentum conversion in dielectric metasurfaces” Optics Express 25, 377 (2017)
80. Robert C. Devlin, Antonio Ambrosio, Noah A. Rubin, J.P. Balthasar Mueller, and Federico Capasso, “Arbitrary spin-to-orbital angular momentum conversion of light”, Science 358, 896 (2017)
81. M. Khorasaninejad and F. Capasso “Metalenses: Versatile multifunctional photonic components”, Science 358, 8100 (2017)
70. Jura Rensberg, You Zhou, Steffen Richter, Chenghao Wan, Shuyan Zhang, Philipp Schöppe, Rüdiger Schmidt-Grund, Shriram Ramanathan, Federico Capasso, Mikhail A. Kats, and Carsten Ronning “Epsilon-Near-Zero Substrate Engineering for Ultrathin-Film Perfect Absorbers” Physical Review Applied 8, 14009 (2017)
71. Benedikt Groever, Wei Ting Chen, and Federico Capasso “Meta-Lens Doublet in the Visible Region” Nano Letters 8, 4902 (2017)
72. Wei Ting Chen, Alexander Y. Zhu, Mohammadreza Khorasaninejad, Zhujun Shi, Vyshakh Sanjeev, and Federico Capasso “Immersion Meta-Lenses at Visible Wavelengths for Nanoscale Imaging” Nano Letters 17, 3188 (2017)
73. Alexander Y. Zhu, Wei-Ting Chen, Mohammadreza Khorasaninejad, Jaewon Oh, Aun Zaidi, Ishan Mishra, Robert C. Devlin, and Federico Capasso “Ultra-compact visible chiral spectrometer with meta-lenses”APL Photonics 2, 036103 (2017)
74. Mohammadreza Khorasaninejad, Zhujun Shi, Wei-Ting Chen, Vyshakh Sanjeev, Aun Zaidi, and Federico Capasso “Achromatic metalens over 60 nm bandwidth in the visible and metalens with reverse chromatic dispersion’ Nano Letters 17, 1819 (2017)

75. R. Sawant, P. Bhumkar, A.Y. Zhu, P. Ni, F. Capasso, and P. Genevet. Mitigating Chromatic Dispersion with Hybrid Optical Metasurfaces, Advanced Materials 30, 48 (2018)
76. W-T Chen, A. Y. Zhu, J. Sisler, Yao-Wei Huang, K. M. A. Yousef, E. Lee, C-W Qiu, and F. Capasso. Broadband Achromatic Metasurface-Refractive Optics. Nano Letters 18, 7801 (2018)
77. N. A. Rubin, A. Zaidi, M. Juhl, R. P.Li, J.P. Balthasar Mueller, R. C. Devlin, K. Leósson, and F. Capasso. Polarization state generation and measurement with a single metasurface. Optics Express 26, 21455 (2018)
78. H. Pahlevaninezhad, M. Khorasaninejad, Y-W Huang, Z. Shi, Lida P. Hariri, D. C. Adams, V. Ding, A. Zhu, C-W Qiu, F. Capasso, and M. J. Suter, Nano-optic endoscope for high-resolution optical coherence tomography in vivo, Nature Photonics 12, 540 (2018)
79. A. Y. Zhu, W-T Chen, J. Sisler, K. M. A. Yousef, E. Lee, Y-W Huang, C-W Qiu, and F. Capasso “Compact Aberration-Corrected Spectrometers in the Visible Using Dispersion-Tailored Metasurfaces. Advanced Optical Materials 1801144 DOI: 10.1002/adom.20180114 (2018)
80. R. Pestourie, C. Pérez-Arancibia, Z. Lin, W. Shin, F. Capasso, S. G. Johnson, Inverse design of large-area metasurfaces, Optics Express 26, 33732 (2018)
81. Alexander Y. Zhu, Wei Ting Chen, Jared Sisler, Kerolos M. A. Yousef, Eric Lee, Yao-Wei Huang, Cheng-Wei Qiu, and Federico Capasso “Compact Aberration-Corrected

Spectrometers in the Visible Using Dispersion-Tailored Metasurfaces" Advanced Optical Materials 1801144 (2018)
82. Wei Ting Chen, Alexander Y. Zhu, Jared Sisler, Yao-Wei Huang, Kerolos M. A. Yousef, Eric Lee, Cheng-Wei Qiu, and Federico Capasso "Broadband Achromatic Metasurface-Refractive Optics' Nano Letters 18,7810 (2018)
83. Noah A. Rubin, Aun Zaidi, Michael Juhl, Ruo Ping Li, J.P. Balthasar Mueller, Robert C. Devlin, Kristján Leósson, and Federico Capasso "Polarization state generation and measurement with a single metasurface" Optics Express 26, 21455 (2018)
84. Hamid Pahlevaninezhad, Mohammadreza Khorasaninejad, Yao-Wei Huang, Zhujun Shi, Lida P. Hariri, David C. Adams, Vivien Ding, Alexander Zhu, Cheng-Wei Qiu, Federico Capasso, and Melissa J. Suter "Nano-optic endoscope for high-resolution optical coherence tomography in vivo" Nature Photonics 12, 540 (2018)
85. Alexander Y. Zhu, Wei Ting Chen, Aun Zaidi, Yao-Wei Huang, Mohammadreza Khorasaninejad, Vyshakh Sanjeev, Cheng-Wei Qiu, and Federico Capasso "Giant intrinsic chiro-optical activity in planar dielectric nanostructures" Light: Science & Application 7, 17158 (2018)
86. Zhujun Shi, Mohammadreza Khorasaninejad, Yao-Wei Huang, Charles Roques-Carmes, Alexander Y. Zhu, Wei Ting Chen, Vyshakh Sanjeev, Zhao-Wei Ding, Michele Tamagnone, Kundan Chaudhary, Robert C. Devlin, Cheng-Wei Qiu, and Federico Capasso "Single-Layer Metasurface with Controllable Multiwavelength Functions" Nano Letters 0, 0 (2018)
87. Wei Ting Chen, Alexander Y. Zhu, Vyshakh Sanjeev, Mohammadreza Khorasaninejad, Zhujun Shi, Eric Lee, and Federico Capasso "A broadband achromatic metalens for focusing and imaging in the visible" Nature Nanotechnology 13, 220 (2018)
88. Yao-Wei Huang, Noah A. Rubin, Antonio Ambrosio, Zhujun Shi, Robert C. Devlin, Cheng-Wei Qiu, and Federico Capasso, "Versatile total angular momentum generation using cascaded J-plates" Optics Express 27, 5 (2019)

89. Wei Ting Chen, Alexander Y. Zhu, Jared Sisler, Zameer Bharwani, and Federico Capasso "A broadband achromatic polarization-insensitive metalens consisting of anisotropic nanostructures" Nature Communications 10, 355 (2019)
90. Noah A. Rubin, Gabriele D'Aversa, Paul Chevalier, Zhujun Shi, Wei Ting Chen, and Federico Capasso, "Matrix Fourier optics enables a compact full-Stokes polarization camera" Science 365, 6448 (2019)

Loncar Group

91. H. Atikian, P. Latawiec, X. Xiong, S. Meesala, S. Gauthier, D. Wintz, J. Randi, D. Bernot, S. DeFrances, J. Thomas, M. Roman, S. Durrant, F. Capasso, and M. Loncar. Submitted. "Diamond Mirror for High Power Lasers." arXiv:1909.06458 (2019)
92.. H. A. Atikian, P. Latawiec, M. J. Burek, Y. I. Sohn, S. Meesala, N. Gravel, A. B. Kouki, and M. Loncar. "Freestanding nanostructures via reactive ion beam angled etching." APL Photonics, 2, 051301 (2017).
93. Z. Lin, A. Pick, M. Lončar, and A. W. Rodriguez "Enhanced spontaneous emission at third-order dirac exceptional points in inverse-designed photonic crystals." Physical Review Letters, 10, 117 (2016).

94. Z. Lin, X. Liang, M. Loncar, S.G. Johnson, A.W. Rodriguez, “Cavity-enhanced second harmonic generation via nonlinear-overlap optimization”, Optica, 3, 233 (2016)

95. Z. Lin, B. Groever, F. Capasso, A. W. Rodriguez, and M. Lončar, “Topology Optimized Multi-layered Meta-optics.” Physical Review Applied, 9, 044030 (2018)

96. Y. Li, S. Kita, P. Muñoz, O. Reshef, D. I. Vulis, M. Yin, M. Lončar, and E. Mazur, “On-chip zero-index metamaterials”, Nature Photonics, 9, 738 (2015)

97. S. Kita, Y. Li, P. Muñoz, O. Reshef, D. I. Vulis, R. W. Day, E. Mazur, and M. Lončar, “On-chip all-dielectric fabrication-tolerant zero-index metamaterials.” Optics Express, 7, 8326 (2017)

98. D. I. Vulis, Y. Li, O. Reshef, P. Camayd-Muñoz, M. Yin, S. Kita, M. Lončar, and E. Mazur, “Monolithic CMOS-compatible zero-index metamaterials.” Optics Express, 25, 12381 (2017)

99. Z. Lin, L. Christakis, Y. Li, E. Mazur, A. W. Rodriguez, and M. Lončar. “Topology-optimized Dual-Polarization Dirac Cones.” Physical Review B, 97, 081408(R) (2018)

100. C. Wang, Z. Li, M. H. Kim, X. Xiong, X. F. Ren, G. C. Guo, N. Yu, and M. Lončar, “Metasurface-assisted phase-matching-free second harmonic generation in lithium niobate waveguides.” Nature Communications, 8, 2098 (2017).

101. Z. Li, M. H. Kim, C. Wang, Z. Han, S. Shrestha, A. C. Overvig, M. Lu, A. Stein, A. M. Agarwal, M. Lončar, and N. Yu.. “Controlling propagation and coupling of waveguide modes using phase-gradient metasurfaces.” Nature Nanotechnology, 12, 5 (2017)

102. M. Jankowski, C. Langrock, B. Desiatov, A. Marandi, C. Wang, M. Zhang, C. R. Phillips, M. Loncar, and M. M. Fejer. “Ultrabroadband Nonlinear Optics in Nanophotonic Periodically Poled Lithium Niobate Waveguides.”, to appear in Optica (2019)

103. I. C. Huang, J. Holzgrafe, R. A. Jensen, J. T. Choy, M. G. Bawendi, and M. Lončar. 2016. “10 nm gap bowtie plasmonic apertures fabricated by modified lift-off process.” Applied Physics Letters, 13, 109 (2016)

Engheta Group

104. F. Abbasi, A. R. Davoyan, and N. Engheta, “One-Way Surface States due to Nonreciprocal Light-Line Crossing,” New Journal of Physics, 17, 063014 (2015).

105. N. Engheta, “150 Years of Maxwell’s Equations,” A perspective article Science, 340, 136 (2015).

106. A.M. Mahmoud, A. R. Davoyan, and N. Engheta, “All-Passive Nonreciprocal Metasurface,” Nature Communications, Vol. 6:8359, September 28, 2015.

107. Y. Li, I. Liberal and N. Engheta, “Metatronic Analogues of the Wheatstone Bridge,” Journal of Optical Society of America B, Special Issue on “EM Metasurfaces”, Vol. 33, A72, February 2016.

108. J. Kim, A. Dutta, G. V. Naik, A. V. Kildishev, A. J. Giles, F. J. Bezares, C. T. Ellis, J. G. Tischler, O. J. Glembocki, A. M. Mahmoud, H. Caglayan, J. D. Caldwell, A. Boltasseva, and N. Engheta, “The Role of Epsilon-Near-Zero Substrates in the Optical Response of Plasmonic Antennas,” Optica, Vol. 3, p. 339, March 2016.

109. C. Della Giovampaola and N. Engheta, “Plasmonics without Negative Dielectrics,” Physical Review B, Vol. 93, 195152, May 24, 2016.

110. Y. Li, I. Liberal, C. Della Giovampaola, and N. Engheta, “Waveguide Metatronics: Lumped Circuitry based on Structural Dispersion,” Science Advances, Vol. 2: e1501790, June 10, 2016.

111. Y. Li, I. Liberal, and N. Engheta, “Dispersion Synthesis with Multi-Ordered Metatronic Filters,” Optics Express, Vol. 25, No. 3, pp. 1937-1948, February 6, 2107.

112. I. Liberal and N. Engheta, “Near-Zero Refractive Index Photonics”, Nature Photonics, Vol. 11, pp. 149-158, March 2017.

113. I. Liberal, A. Mahmoud, Y. Li, B. Edwards, and N. Engheta, “Photonic Doping of Epsilon-Near-Zero Media,” Science, Vol. 355, Issue 6329, pp. 1058-1062, March 10, 2017.

114. F. Prudencio, J. Costa, C. Fernandes, N. Engheta and M. Silveirinha, “Experimental Verification of “Waveguide” Plasmonics,” New Journal of Physics, Vol. 19, 123017, December 6, 2017.

I115. I. Liberal and N. Engheta, “The Rise of Near-Zero-Index Technologies”, a Perspective article in Science, Vol. 358, 1540-1541, December 22, 2017.

I12. Liberal, Y. Li, and N. Engheta, “Reconfigurable Epsilon-Near-Zero Metasurfaces via Photonic Doping,” Nanophotonics, Vol 7 (6), pp. 1117-1127, June 16, 2018.

113. E. Nahvi, I. Liberal and N. Engheta, “Nonperturbative Effective Magnetic Nonlinearity in ENZ Media Doped with Kerr Dielectric Inclusions,” ACS Photonics, Vol. 6, No. 11, pp. 2823-2831, September 13, 2019.

114. Y. Li, I. Liberal and N. Engheta, “Structural-Dispersion-based Loss Reduction in Plasmonics,” *Science Advances*, Vol. 5, no. 10, eaav3764, October 11, 2019.

Mosallei Group

115. J. Cheng, D. Ansari, and H. Mosallaei, “Wave manipulation with designer dielectric metasurfaces,” Optics Lett, vol. 39, no. 21, Nov. 2014.

116. J. Cheng and H. Mosallaei, “Truly achromatic optical metasurfaces: A filter circuit theory based-design,” JOSA B, vol. 32, no. 10, pp. 2115-2121 (2015).

117. J. Cheng, S. Jafar-Zanjani, H. Mosallaei, “All-dielectric ultrathin conformal metasurfaces: lensing and cloaking applications at 532 nm wavelength,” Scientific Report, 6, 38440, DOI: 10.1038/srep38440, 2016.

114. A. Forouzmand, S. Tao, S. Jafar-Zanjani, J. Cheng, M. M. Salary, H. Mosallaei, “Double split-loop resonators as building blocks of metasurfaces for light manipulation: Bending, focusing, and flat-top generation,” JOSA B, vol. 33, no. 7, July 2016.

115. A. Forouzmand and H. Mosallaei, “All-dielectric C-shaped nanoantennas for light manipulation: Tailoring both magnetic and electric resonances to the desire,” Adv. Optical Mater., 1700147, DOI: 10.1002/adom.201700147.

116. A. Forouzmand and H. Mosallaei, “Shared aperture antenna for simultaneous two-dimensional beam steering at near-infrared and visible,” J. Nanophoton. 11(1), 010501 (2017).

117. J. Cheng, S. Jafar-Zanjani, H. Mosallaei, “Real-Time Two-Dimensional Beam Steering with Gate-Tunable Materials: A Theory Design Investigation,” Applied Optics, vol. 55, no. 22, 2016.
118. A. Forouzmand and H. Mosallaei, “Real-time controllable and multi-functional metasurfaces utilizing indium tin oxide materials: A phased array prospective,” IEEE Trans. Nanotechnology, VOL. 16, NO. 2, pp. 296-306, March 2017.
119. A. Forouzmand, H. Mosallaei, “Tunable two dimensional optical beam steering with reconfigurable indium tin oxide plasmonic reflectarray metasurface,” Journal of Optics, 18 (2016), 125003.
120. A. Forouzmand, M. M. Salary, S. Inampudi, and H. Mosallaei, “A tunable multigate indium-tin-oxide-assisted all-dielectric metasurface,” Adv. Optical Mater., 1701275, DOI: 10.1002/adom.201701275, 2018.

5. Patents

Capasso Group

1. F. Capasso et al. Broadband dispersion-compensated and chiral meta-holograms US20180259700A1 (2016)
2. F. Capasso et al. Atomic layer deposition process for fabricating dielectric metasurfaces for wavelengths in the visible spectrum, US20180341090A1 (2018)
3. F. Capasso et al. Polarization-selective scattering antenna arrays based polarimeter, US US20180066991A1 (2018)
4. M. Khorasaninejad and F. Capasso, Broadband multifunctional efficient meta-gratings based on dielectric waveguide and phase shifters, US20180210147A1 (2018)
5. F. Capasso et al. Meta-lens doublet for aberration correction WO201762501422P (2018)
6. F. Capasso et al. Broadband dispersion-compensated and chiral meta-holograms US20180259700A1 (2018)
7. A. She and F. Capasso, Method and system for polarization state generation US20180045889A (2018)
8. F. Capasso et al. Broadband dispersion-compensated and chiral meta-holograms US20180259700A1 (2018)
9. F. Capasso et al. Ultra-compact, aberration corrected, visible chiral spectrometer with metalenses WO2018118984A1 (2018)
10. F. Capasso et al. Planar achromatic and dispersion-tailored meta-surfaces in visible spectrum WO2018222944A1 (2018)
11. F. Capasso et al. Achromatic metalens and metalens with reverse chromatic dispersion US10408416B2 (2019)
12. F. Capasso et al. Substrate-formed metasurface devices US US20190025463A1 (2019)
13. F. Capasso et al. Highly efficient data representation of dense polygonal structures US20190025477A1 (2019)
14. F. Capasso et al. Optical devices including rotary variable optical elements, US20190346658A1 (2019)
15. F. Capasso et al. Electrically-stretchable planar optical elements using dielectric elastomer actuators US20190257984A1 (2019)
16. F. Capasso et al. Spin-to-orbital angular momentum converter for light WO2019108290A9 (2019)
17. F. Capasso et. al. Topology optimized multi-layered meta-optics WO2019103762A9 (2019)

18. F. Capasso et al. Endoscopic imaging using nanoscale metasurfaces WO2019118646A1 (2019)
19. F. Capasso et al. Immersion meta-lens at visible wavelengths for diffraction-limited imaging WO2018183774A1
20. F. Capasso et al. Angle-dependent or polarization-dependent metasurfaces with wide field of view WO2019136166A1 (2019)
21. F. Capasso et al. Aberration correctors based on dispersion-engineered metasurfaces WO2019164849A1 (2019)

Yu Group

1. N. Yu et al "Amplitude and phase spatial light modulator based on miniature optical resonators," provisional patent filed on Apr. 2, 2019.
2. M. Lipson, J. Hone, N. Yu, I. Datta, and S. H. Chae, "Efficient phase shifters using electro-refractive modulation of monolayer transition metal di-chalcogenides in photonic structures," provisional patent filed on Feb. 21, 2019.
3. N. Yu, et al. "Metasurfaces with complete control of the amplitude and phase of light at up to three wavelengths simultaneously," US Provisional US62/546,951, PCT/US18/46947, Licensed to MetaLenz Inc.
4. N. Yu, et al US62/510,670, PCT/US18/34460, Licensed to MetaLenz Inc.
5. N. Yu and Z. Li, "Systems and methods for active photonic devices using correlated perovskites," PCT application filed on Aug. 29, 2017.
6. N. Yu, et al. "Methods and systems for radiative cooling and heating," US62/181,674, PCT/US16/38190, US15/845,820,
7. N. Yu, et al., "Integrated photonic devices based on waveguide patterned with optical antenna arrays," PCT application filed on Jun. 24 2014.
8. N. Yu, "System, apparatus and computer-accessible medium for providing a modulation of mid-infrared light using one or more graphene-metal plasmonic antennas," PCT application filed on January 30, 2014.

Purdue team

1. A. Shaltout, S. Choudhury, A. V. Kildishev, A. Boltasseva, V. M. Shalaev, "System for producing ultra-thin color phase hologram with metasurfaces", US9952557B2, 2018
2. A. Shaltout, A. Kildishev, V. Shalaev, J. Liu, "Sub-millimeter real-time circular dichroism spectrometer with metasurfaces", US20170003169A1, 2018
3. A. Shaltout, A. Kildishev, V. Shalaev, "Time-varying metasurface structure", US20170235162A1, 2019

Loncar Group

1. US Patent Application US20180138047A1, "System and method for wafer-scale fabrication of free standing mechanical and photonic structures by ion beam etching", Haig Atikian, Marko Loncar

2. US Patent Application US20180252844A1, "Wavelength selective optical nanostructures fabricated on the surface of bulk homogenous substrates", Haig Atikian, Marko Loncar

Brongersma Group

1. Mark L. Brongersma et al. "Light-field Imaging Using a Gradient Metasurface Optical Element" US20170146806A1 (2017)
2. Mark L. Brongersm et al. "Spatially multiplexed dielectric metasurface optical elements" US10126466B2 (2108)

6. Start Ups

- Federico Capasso is co-founder and Director of Metalenz Inc., which focuses on high volume applications of metalenses such as camera modules for the cell phone market. Harvard has exclusively licensed its portfolio of metalens patents to Metalenz
- Nanfang Yu is the Co-founder and CTO of a startup company MetaRE Inc. that develops and commercializes: (1) radiative-cooling coatings, which can substantially reduce the temperatures of buildings, shipping containers, and palletized goods by strongly reflecting solar radiation and efficiently dissipating heat through thermal radiation; (2) radiative-cooling textiles, which have optimal cooling capabilities by combining radiative, convective, and evaporative cooling mechanisms. The startup has licensed the entire portfolio of IPs related to radiative cooling from Columbia Technology Ventures.

  Nanfang Yu serves on the advisory board of Metalenz Inc. that develops and commercializes flat lenses based on metasurfaces. One of his patents on broadband achromatic meta-lenses has been licensed to the Metalenz Inc.
- Marko Loncar is co-founder Peak Power Optics which commercializes high power metasurfaces.
- Mark Brongersma is cofounder of Rolith, which developed a tool that enables inexpensive, large-area nanopatterning. This company was acquired by a company based in Halifax, Canada called Metamaterials Technology Incorporated (MTI, Inc).